DISSERTATION

LARGE-EDDY SIMULATION OF COMPRESSIBLE FLOWS USING THE STRETCHED-VORTEX MODEL AND A FOURTH-ORDER FINITE VOLUME SCHEME ON ADAPTIVE GRIDS

Submitted by

Sean Walters

Department of Mechanical Engineering

In partial fulfillment of the requirements

For the Degree of Doctor of Philosophy

Colorado State University

Fort Collins, Colorado

Spring 2022

Doctoral Committee:

Advisor: Stephen Guzik
Co-Advisor: Xinfeng Gao

Azer Yalin
David Randall

ABSTRACT

LARGE-EDDY SIMULATION OF COMPRESSIBLE FLOWS USING THE STRETCHED-VORTEX MODEL AND A FOURTH-ORDER FINITE VOLUME SCHEME ON ADAPTIVE GRIDS

State-of-the-art engineering workflows are becoming increasingly dependent on accurate large-eddy simulations (LES) of compressible, turbulent flows for off-design conditions. Traditional CFD algorithms for compressible flows rely on numerical stabilization to handle unresolved physics and/or steep gradient flow features such as shockwaves. To reach higher levels of physical-fidelity than previously attainable, more accurate turbulence models must be properly incorporated into existing, high-order CFD codes in a manner that preserves the stability of the underlying algorithm while fully realizing the benefits of the turbulence model. As it stands, casually combining turbulence models and numerical stabilization degrades LES solutions below the level achievable by using numerical stabilization alone.

To effectively use high-quality turbulence models and numerical stabilization simultaneously in a fourth-order-accurate finite volume LES algorithm, a new method based on scale separation is developed using adaptive grid technology for the stretched-vortex subgrid-scale (SGS) LES model. This method successfully demonstrates scheme-independent and grid-independent LES results at very-high-Reynolds numbers for the inviscid Taylor-Green vortex, the temporally-evolving double-shear-flow, and decaying, homogeneous turbulence. Furthermore, the method clearly demonstrates quantifiable advantages of high-order accurate numerical methods.

Additionally, the stretched-vortex LES wall-model is extended to curvilinear mapped meshes for compressible flow simulations using adaptive mesh refinement. The capabilities of the wall-model combined with the stretched-vortex SGS LES model are demonstrated using the canonical zero-pressure-gradient flat-plate turbulent boundary layer. Finally, the complete algorithm is

applied to simulate flow-separation and reattachment over a smooth-ramp, showing high-quality solutions on extremely coarse meshes.

ACKNOWLEDGEMENTS

I would like to thank my advisor, Dr. Guzik, for his guidance, encouragement, and teaching throughout my time in the CFD lab. I have always enjoyed your willingness to listen to my crazy ideas, and through your patience and continual suggestions, I have grown academically and personally. I would also like to thank my co-advisor, Dr. Gao, for her high academic standards, creativity, and persistent help throughout this research. This research would not have been possible without both of you.

I would also like to thank my committee members, Dr. Randall and Dr. Yalin, for their feedback and recommendations. Additionally, I would like to thank Dr. Colella, Dr. Johansen, and Dr. Murman for collaboration that contributed to this research.

I would also like to thank my parents and my sister for their continual support, encouragement, and love.

I would also like to thank my colleagues in the CFD lab, Andy, Chris, Erik, Jordan, Josh, Justin, Landon, Nate, Nelson, Noah, Scott, Taylor, and Yijun for friendship, fun discussions, helpful advice, and a fantastic time in the CFD lab.

I am very grateful for the financial support of Dr. Guzik and Colorado State University during my time in the CFD lab.

Finally, but most importantly, I thank my Creator and Heavenly Father for continual blessings throughout life. Without You, all of this would be impossible.

TABLE OF CONTENTS

LIST OF FIGURES

Chapter 1

Introduction

Much of engineering and science relies heavily upon understanding and modeling turbulent fluid motion and behavior. And yet, while equations describing fluid flows have existed for over two-and-a-half centuries, few analytical solutions exist for flows of practical interest. The nonlinear nature of the Euler and Navier-Stokes equations allow macroscopically-simple flows to rapidly evolve microscopic-complexity. This complexity poses a serious challenge to obtaining analytical solutions for flows with practical configurations. Naturally, mathematicians developed methods of approximation to obtain "close enough" solutions. In the era of ever-increasing digital computational power, engineers and scientists use these methods of approximation and other tools of computational fluid dynamics (CFD) to simulate fluid flows of greater and greater complexity.

In 2014, NASA, in collaboration with industrial and academic partners, released a report detailing a bold vision for CFD capabilities and aerospace design in the year 2030 [1]. Assessing the then-current state-of-the-art of CFD application, the report stated "CFD is not yet sufficiently predictive and automated to be used in critical/relevant engineering decisions by the non-expert user, particularly in situations where separated flows are present." The report went on to propose a series of increasingly complex, CFD "grand challenges" and a CFD development road-map for solving these problems by 2030. Reaching the level of technological capability and readiness as defined in the CFD road-map would enable another of NASA's stated goals — certification-by-analysis-level (CbA) simulations by the year 2025 [2]. The goal of CbA is to eliminate unnecessary physical tests and move toward a digital analysis process for certifying the flight-worthiness of aircraft and spacecraft. It has been estimated that a CbA process would eliminate half of all currently necessary flight tests and would enable faster development times and greater technological developments than previously possible all while greatly reducing development costs [3]. In 2021, NASA released a report detailing its CbA road-map and how to achieve industrial-level readiness and application

of CbA by 2040. The report specifically noted that one of the intended outcomes of the 2030 CFD road-map was the enabling of the 2040 CbA-implementation goal [3].

In order to reach NASA's 2025 goal of simulations usable within CbA, the first of NASA's 2030 CFD Vision grand challenges focused on achieving a large-eddy simulation (LES) "of a powered aircraft configuration across the full flight envelope." The 2014 report stated that "progress toward this goal can be measured through the demonstration of effective hybrid RANS-LES and wall-modeled LES simulations with increasing degrees of modeled versus resolved near-wall structures with increasing geometric complexity." In short, meeting this goal would move CFD capabilities toward using turbulence-resolving methods (such as LES) sufficiently far from the aircraft while using wall-models near the aircraft surface. These wall-models would account for unresolved turbulent-scales generated by the aircraft surface while coupling the effects of flow further away from the surface with the wall. For aircraft operating conditions, this wall-modeled LES approach will sit at the limit of computational capability for the next several decades (unless unforeseen advancements in computational power occur). Accurately coupling the wall-model with the outer-flow LES is a must. Additionally, the LES numerical solver must be numerically stable and robust (i.e., it must provide an answer for any realistic flow without breaking). For compressible flows, traditional methods of achieving numerical stability can artificially introduce a turbulence-damping effect if not properly used in the LES context. As a result, the interaction of models and numerical algorithms (discretizations, numerical regularization, etc.) within the LES framework as a whole must be carefully considered.

To that end, the goals of this research are defined to:

1. implement the stretched-vortex subgrid-scale (SGS) model into an existing fourth-order accurate finite volume algorithm designed to simulate unsteady, compressible flows with or without chemical reactions at high speeds on mapped grids with adaptive mesh refinement (AMR),

2. implement the stretched-vortex SGS wall-model for solving wall-bounded, high-Reynolds number flows,

3. extend the slip-wall type, stretched-vortex SGS wall-model to compressible flows,

4. couple the interior SGS and wall-models with numerical regularization in a self-consistent manner that achieves grid-independence and scheme-independence for turbulent flows,

5. incorporate the LES models into existing AMR infrastructure in order to effectively solve problems exhibiting multi-scale physics and/or strong gradients,

6. demonstrate the LES model capability to effectively capture physics relevant to flat-plate boundary-layers, smooth-body separation, and

7. provide guidance for future efforts in modeling turbulent combustion.

The remainder of this chapter introduces the basics of turbulent flows and why they are challenging to numerically simulate. Typical approaches to overcome challenges in simulating turbulent flows are then presented in the second section of the chapter. A brief synopsis of the rest of the dissertation concludes the chapter.

1.1 Turbulence Scales

Turbulence is a flow phenomenon exhibiting small-scale complexity and a large range of spatial and temporal scales due to the nonlinearity of the governing equations. Throughout the 19th and early 20th centuries, these equations were studied from an analytical perspective without modern digital computers. Although general analytical solutions of turbulent flows evaded researchers, many discoveries of that era paved the way for future research and study with computational resources.

In late 1940, Kolmogorov famously argued that the size of the smallest turbulent flow scales directly correlates with the kinematic viscosity and the energy dissipation rate of the fluid flow [4]. Utilizing further dimensional analysis, one can derive relationships between the largest and smallest spatial and temporal scales such that they only depend on the ratio of inertial forces to viscous

forces, referred to as the Reynolds number, Re, of the flow

$$\mathrm{Re} = \frac{u_0 L_0}{\nu} \,, \tag{1.1}$$

where u_0 is the flow's characteristic velocity and is taken to be L_0/t_0, L_0 is the characteristic length, t_0 is the characteristic time, and ν is the kinematic viscosity of the fluid. For an aircraft wing in flight, the characteristic length-scale would be the chord length of the wing (wing-tip to the wing trailing edge), while the characteristic velocity would be the velocity of the wing relative to the air. While the relationships are rough approximations derived from assumptions of local homogeneity and isotropy of the flow along with an assumption of very high Reynolds number, these relationships provide an idea of the range of scales present in a turbulent flow and are given as

$$\frac{L_0}{\eta} = \mathrm{Re}^{\frac{3}{4}} \quad , \quad \frac{t_0}{\tau} = \mathrm{Re}^{\frac{1}{4}} \,, \tag{1.2}$$

where η is the Kolmogorov length-scale defining the spatial size of the smallest eddies and τ is the time associated with the "turnover" of the smallest eddies. This ratio between the largest and smallest length-scales in a turbulent flow imposes a constraint on simulations that attempt to resolve all of the turbulent length-scales. As a consequence of Eq. (1.2), in a three-dimensional simulation, the discretization size will scale with $\mathrm{Re}^{9/4}$. At relatively low Reynolds numbers of a few thousand, modern CFD codes and high-performance computing (HPC) architectures are capable of providing fully resolved turbulent flow results. For physically realistic flows at high Reynolds numbers however, the numerical requirements are impractically large to obtain fully resolved simulations. Considering a turbulent flow with a Reynolds number of one million, Eq. (1.2) provides a rough estimate that the numerical discretization would require tens of trillions of discretization points. This size of simulation is well beyond the reach of the majority of CFD today and will likely remain that way for some time. As a result, a method of separating and solving for only the scales-of-interest is required. The next section addresses several methods of scale-separation.

1.2 Approximation Through Scale-Separation

Recognizing the large range of scales in turbulent flows, Osborne Reynolds, while attempting to analytically understand turbulence onset [5], decomposed turbulent flow fields, u, into mean portions, $\bar{u}$, and fluctuating portions, u',

$$u = \bar{u} + u' \quad , \quad \overline{u'} = 0 \; . \tag{1.3}$$

The main issue with such a decomposition is that, for nonlinear equations, the mean portions of the solution, $\bar{u}$, depend on the fluctuating portions, u'. In order to know the mean part of the solution, one must also know the fluctuating part of the solution, which then requires that one know the entire solution.

To address this, an assumption of some form must be made and a model for the fluctuating solution must be introduced. This is the entire issue when one desires to model turbulence (model u' and solve for $\bar{u}$) rather than directly solve for all turbulent-scales (solve for u instead of just $\bar{u}$). How this issue is addressed and what is being solved differentiates multiple practical methods of turbulence modeling. The following sections will cover a few of these, namely Reynolds-averaged Navier-Stokes (RANS), explicitly-modeled LES, and implicit LES (ILES).

1.2.1 Reynolds-Averaged Navier-Stokes

RANS methods assume the resolved solution is a statistical or time-averaged representation of the fluid flow. A consequence of this modeling assumption is that these methods do not directly resolve instantaneous turbulent fluid motions, but instead resolve the statistically-averaged or time-averaged turbulent motions. The closure models employed by RANS must incorporate as much of the effects of turbulent motions as possible. With so many of the flow scales being modeled, RANS models must often rely significantly on physical hypotheses for the correct description of a flow of interest. As a result, closure models employed by RANS are often tuned to a specific set of canonical flow configurations and can perform poorly in off-design simulations. Moreover,

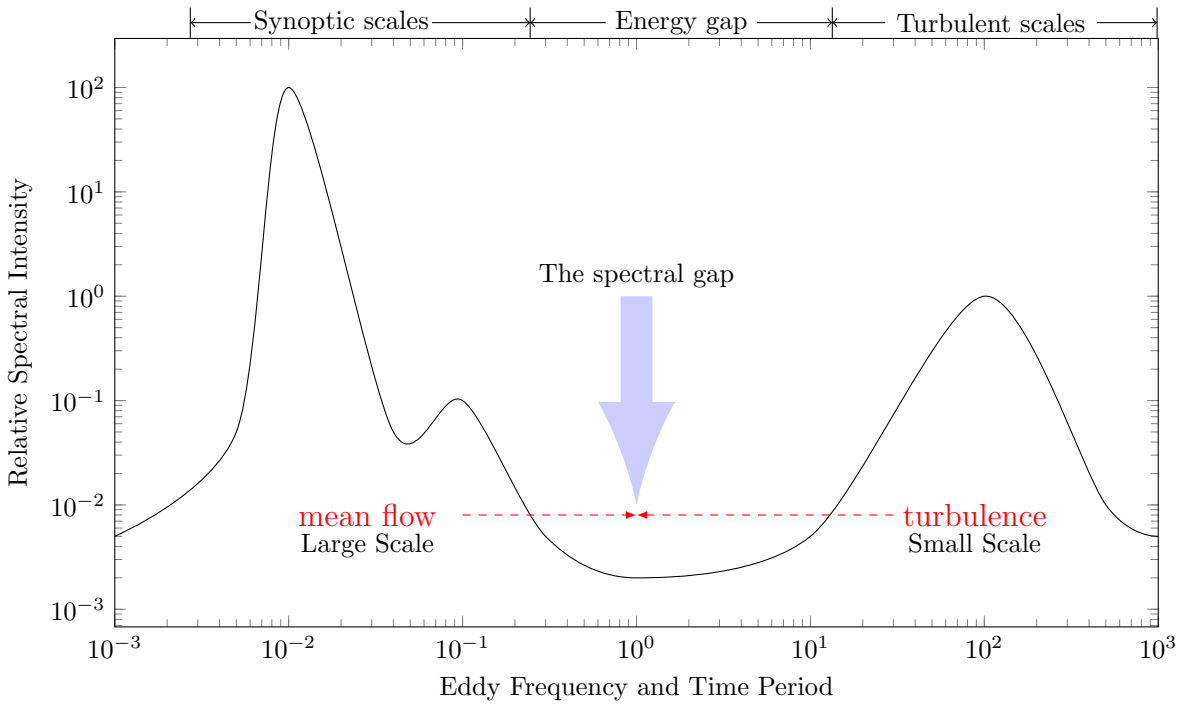

Figure 1.1: Illustration of spectral gap.

for unsteady RANS (URANS) models designed to simulate flows with large-scale, unsteady, non-turbulent motions (e.g. large vortex structures), a distinct spectral gap, as illustrated by Fig. 1.1, would be ideal in the turbulent flow under consideration. For all of these reasons, RANS-based approaches in CFD modeling for turbulent flows have plateaued in their ability to resolve the critical technical challenges of the present related to off-design exploration and complex physics modeling [6].

1.2.2 Explicitly Modeled Large-Eddy Simulation

LES is a promising alternative to RANS and is more computationally achievable than simulating all scales as in direct numerical simulation (DNS), in that it solves large turbulent-scales while modeling small-scale effects to provide a solution acceptable for many engineering requirements. The approach is logical when rate-limiting processes happen at the larger resolved scales [7]. Even so, defining and modeling the small scales becomes one of the key issues in LES.

Additionally, previous research has highlighted the extent to which the underlying numerical solver affects LES solutions [8]. When simulating vortex-dominated flows, high-order algorithms are necessary in order to more fully capture the nonlinear effects of unsteady vortex interactions [9]. Additionally, numerical stability and numerical diffusivity are critical features when simulating compressible, turbulent flows. The need for high-order, stable, non-diffusive algorithms is especially high in flows where small scales impact the evolution of large-scale, global phenomenon. Research has shown that combining numerical regularization (methods designed for maintaining numerical stability such as limiters) with turbulence models can provide results dominated by the numerical regularization [10]. Even using high-order discretizations and complex numerical regularization machinery, these simulations can still incorrectly predict well-resolved kinetic energy. As a result, much improvement is possible for LES of complex flows of engineering interest.

1.2.3 Implicit Large-Eddy Simulation

Implicit LES relies on carefully designed characteristics of the underlying numerical algorithm (e.g. numerical regularization or dissipation) to provide the necessary closure of the nonlinear filtered terms [11–16]. While ILES has seen widespread use, there are distinct issues with this method that still remain to be solved. For example, research has shown that arbitrary usage of various ILES numerical regularization techniques in the context of turbulent flows can incorrectly predict well-resolved kinetic energy and provide incorrect turbulence evolution [10, 11, 17–19]. These issues are expected to only grow with the addition of more complex physics models. For ILES methods to gain consistent success in *predictive* simulations, it must be placed on a more thoroughly rigorous and self-consistent mathematical footing. As it currently stands, naive implementations essentially solve "lower-Reynolds number" physics but present this as the solution to the high-Reynolds number problem that was originally intended.

1.3 Dissertation Organization

The rest of this dissertation is organized as follows. The mathematical foundation of LES, filtering, is discussed to some length in Chapter 2. Chapter 3 presents the governing equations utilized throughout the rest of this study. The governing equation terms requiring closure and the model used to close these terms, the stretched-vortex SGS model, are detailed in Chapter 4. Chapter 5 describes the fourth-order finite volume algorithm which forms the numerical framework in which the LES model is applied. The configurations of test problems are described in Chapter 6, while results also serving as validation are presented in Chapter 7. Chapter 8 concludes the dissertation with a summary of important results.

Chapter 2

Filtering

Filtering is a convenient mathematical formalism for scale-separation, and it provides a core element around which an understanding of the scale-separated problem can be constructed. Ideally, an appropriate filter transforms the equations from the original space containing all the flow scales to the form exactly representing only the scales of interest. As things are rarely ideal, significant approximation is required during the process. While entire fields of research are dedicated to filters and filtering, an overview of the basics of filters as used within LES is presented here.

2.1 Basic Concepts for Filters and Filtering

As operators which modify or remove solution information, filters have an extremely broad range of forms. Traditional LES filters have been linear, low-pass (i.e. smoothing) operators where the filter operator $\mathcal{L}$ applied to a turbulent data field, u, provides the low-frequency (filtered) field $\bar{u}$,

$$\bar{u} = \mathcal{L}(u) \ . \tag{2.1}$$

An operator $\mathcal{L}$ is linear if, when applied to function variables ϕ and ψ and scalar constant α, it satisfies

$$\mathcal{L}(\phi + \psi) = \mathcal{L}(\phi) + \mathcal{L}(\psi) \quad , \quad \mathcal{L}(\alpha\phi) = \alpha\mathcal{L}(\phi) \ . \tag{2.2}$$

For example, applying this operator to the linear advection equation, it can be seen that

$$\mathcal{L}\left(\frac{\partial u}{\partial t} + a\frac{\partial u}{\partial x}\right) = \mathcal{L}\left(\frac{\partial u}{\partial t}\right) + a\mathcal{L}\left(\frac{\partial u}{\partial x}\right) = 0 \ . \tag{2.3}$$

While there is a possibility that a nonlinear filter would provide an improvement over a linear filter, nonlinear filters are difficult to work with and have generally been avoided or overlooked by LES researchers. Another filter trait generally sought within the LES community is commutativity with

differentiation. An operator is commutative with differentiation if,

$$\mathcal{L}\left(\frac{\partial \phi}{\partial x}\right) = \frac{\partial}{\partial x}\left(\mathcal{L}\left(\phi\right)\right) \ . \tag{2.4}$$

Applying this to the example linear advection equation provides

$$\mathcal{L}\left(\frac{\partial u}{\partial t}\right) + a\mathcal{L}\left(\frac{\partial u}{\partial x}\right) = \frac{\partial}{\partial t}\left(\mathcal{L}\left(u\right)\right) + a\frac{\partial}{\partial x}\left(\mathcal{L}\left(u\right)\right) = 0 \ . \tag{2.5}$$

Additionally, filters can be invertible or non-invertible. An invertible filter is one that satisfies

$$\mathcal{L}^{-1}\left(\bar{\phi}\right) = \mathcal{L}^{-1}\left(\mathcal{L}\left(\phi\right)\right) = \phi \ , \tag{2.6}$$

where $\mathcal{L}^{-1}$ is the inverse filter operator. A consequence of using an invertible filter is that sub-analytical-filter-scale (SAFS) information can be recovered from filtered data. Filters can also be classified as projective or non-projective. Projective operators satisfy

$$\mathcal{L}\left(\mathcal{L}\left(\phi\right)\right) = \mathcal{L}\left(\phi\right) \ . \tag{2.7}$$

In practice, many LES filter operators are formally non-projective. Some of these filters even retain some solution information at all scales. However, discrete numerical methods are projective at some scale as the numerical discretization imposes its own projective filter to the system. Mathematically speaking, projective filters are non-invertible and it is impossible to exactly recover SAFS information from these types of filters. When the numerical discretization or "grid" is the filter being referred to in LES, the SAFS information is referred to as SGS information. Lastly, LES filters typically preserve constants (i.e. conservation preserving)

$$\mathcal{L}\left(\alpha + \phi\right) = \alpha + \mathcal{L}\left(\phi\right) \ . \tag{2.8}$$

Within the LES construct, filters are generally viewed as convolution integral operators, $*$, applied to data fields. A space-time filtered field, $\bar{\phi}$, is defined as [20],

$$\bar{\phi}(\vec{x},t) = G * \phi(\vec{x},t) = \int_{-\infty}^{\infty}\int_{-\infty}^{\infty} \phi(\vec{\xi},\tau)G(\vec{x}-\vec{\xi},t-\tau)d\tau d\vec{\xi}\,, \tag{2.9}$$

where the filter convolution kernel function, G, has a cut off length $\Delta_{\vec{x}}$ and cut off time Δ_τ. A one-dimensional space-time convolution filter example is the parabolic filter [21],

$$\bar{\phi}\,(x,t) = \frac{\sqrt{\Delta_t}}{(4\pi)^{1/2}\,\Delta_x}\int_{-\infty}^{t}\int_{-\infty}^{\infty} \frac{\phi(\xi,\tau)}{(t-\tau)^{1/2}} e^{\left(-\frac{(x-\xi)^2\Delta_t}{4\Delta_x^2(t-\tau)}-\frac{t-\tau}{\Delta_t}\right)}\,\mathrm{d}\xi\,\mathrm{d}\tau\ . \tag{2.10}$$

Note that this is the solution to the nonhomogeneous heat equation [22]. As a result, for Eq. (2.10), the related inverse convolution (a deconvolution) is known to be written, in the differential form, as

$$\phi = \bar{\phi} + \Delta_t\frac{\partial\bar{\phi}}{\partial t} - \Delta_x^2\frac{\partial^2\bar{\phi}}{\partial x^2}\ . \tag{2.11}$$

For nonhomogeneous partial differential equations (PDE) with an integral solution that represents a filtering operation, the PDE is the deconvolution operator in differential form. It is apparent that the filter must be non-projective since the deconvolution operator exists and it is also apparent that the deconvolution operator could be used to filter an equation by direct variable substitution. That is, since a function of the form $\phi = \mathcal{L}\left(\bar{\phi}\right)$ is known, ϕ can be replaced by a function of only $\bar{\phi}$. The problem is, variable substitution implies the final system retains all original information and that no "filtering" really occurs [23].

An additional important property of LES filters is the preservation of invariants present in the original governing equations. Invariants are measurable properties of a dynamical system remaining unchanged independent of an observer's reference frame. Briefly stated, Noether's theorem demonstrates that systems which remain unchanged with reference-frame changes have associated conservation laws [22]. For example, a system which is independent of the temporal reference frame conserves energy. As a result, LES filters and models should preserve the original governing

equations' invariants. Many researchers have explored this concept, with most demonstrating the lack of invariance preservation in many LES filters and models [20, 24–28].

2.2 Explicit Filtering versus Implicit Filtering

It should be mentioned that while the LES community generally defines equations with formal, analytical filters, it is rather rare that filters are explicitly utilized within algorithms solving turbulent flows. Additionally, it is uncommon for LES models to be derived based on the assumption of an explicit specified filter function. Generally, it is assumed that most models can dissipate enough information out of the system and explicit filtering is unnecessary. In these cases, the effect of models and discretizations together form an implicit filter. Unless filters are explicitly used to filter solution data during the evolution of the governing equations, the resulting method is referred to as implicitly-filtered LES (not to be confused with implicit LES or ILES). Even in cases where explicit filters are used, unless the filter is projective and the filter width is sufficiently large, the filter-like natures of the numerical scheme and the discretization will contribute additional properties to the explicit filter. The combined effect of any explicit filters, turbulence models, the discretization, and the numerical scheme is generally referred to as the effective filter. This is the filter which is critical for practical LES as it governs what is actually being solved by the LES system.

2.2.1 Space Filtering

One of the first LES models derived from a specific filter function was the work of Clark [29]. The model for the nonlinear term was based on the assumption that the scale-separator was a box filter. The resulting model is consistent with the mathematical definition of the box filter applied to the equations. Unfortunately, this method is an unstable turbulence modeling system. The attempt to recover SGS information without sufficient regularization or dissipation causes the failure of this model in general.

Explicitly spatially-filtered LES simulations have seen even less development and practical utilization than the development of LES models based on a specified filter function. However, it is theoretically necessary to utilize something equivalent to explicit filtering in order to achieve grid-independent LES solutions. If explicit filtering is not used and the mesh resolution is increased, the LES problem changes. With enough mesh resolution and no explicit filtering, the LES becomes DNS and any explicit turbulence models are no longer necessary. Some of the first three-dimensional, explicitly filtered simulations demonstrating grid-independent results were obtained only in the last two decades [30, 31].

2.2.2 Space-Time Filtering

A little over a decade after the identification of the convolution operator as taking the role of the LES scale-separator, it was suggested that simultaneous space-time filtering was a feasible option and could increase the accuracy of the resulting LES formulation [32, 33]. The resulting formulation was another case of model development based on a specified filter function (as opposed to explicitly filtering the solution fields). Although the terms were still truncated at 4th-order accuracy so as to only include up to 3rd-order derivatives in the final system, the nonlinear term was modeled using a Gaussian filter in the space-time domain. It is important to note that Taylor-series expansions of the Gaussian filter and the box/top-hat filter are identical in form up to 4th-order accuracy and, as a result, are indistinguishable at that level of accuracy. As a result, the system was identical to Clark's model except for the additional time-derivatives.

Other researchers have investigated space-time filtering since Dakhoul and Bedford, but the method has seen relatively limited application [34–37]. The author of this dissertation performed some research on space-time filtering (Favre-averaged spatial-temporal LES — FAST LES), and while the results showed some promise, the method experienced drawbacks related to providing a consistent mathematical and numerical framework for the implementation of the method [37]. The author of this dissertation is unaware of any truly explicit space-time filtering of LES solution data as a part of the simulation process.

2.2.3 Time-Filtering

While the vast majority of LES filtering operators have been defined as spatial filters or spatio-temporal filters, a few researchers have utilized temporal filtering when formulating the filtered Navier-Stokes equations that govern the LES simulation [38–40]. Most notably, Pruett investigated temporal filtering and analyzed the invariance properties of a general temporal filter. His findings showed that, while temporal filtering was invariant under specific transformations such as constant-velocity translation, the temporally filtered Navier-Stokes equations are not invariant under general changes of reference frame (it is known that general spatial filters are also not invariant under all changes of reference frame) [24]. Additionally, a general approximate deconvolution model was developed for temporally filtered flows [41].

2.3 Theoretical and Practical Filtering

As mentioned previously, many approximations must be made when filtering, but sometimes, it's good to hope for the ideal. It is important to note that the following discussion assumes that the numerical discretization acts as a type of filtering. Given that the equations must be solved numerically, the combination of the ideal analytical filter and the ideal numerical discretization would remove all information that cannot be simulated (unrepresentable scales) while perfectly resolving all representable scales.

Considering the spectral content of the classical turbulence cascade, the application of this ideal system would look something similar to Fig. 2.1a. For this case, the SAFS terms and the SGS terms would be identical as the scales representable by the discretization would be fully resolved by the numerical discretization. In reality, both the analytical filter and the numerical discretization will be non-projective and the numerical algorithm will introduce an extra loss of information beyond what is provided by the mesh (i.e. the numerical algorithm will be dissipative). The dissipation and loss of information experienced with the realistic system results in a situation described by Fig. 2.1b. Obviously some of the scales previously defined as $\overline{u}$ are now gone due to any analytical or explicit filtering and the effects of the numerical discretization. The resulting system can be

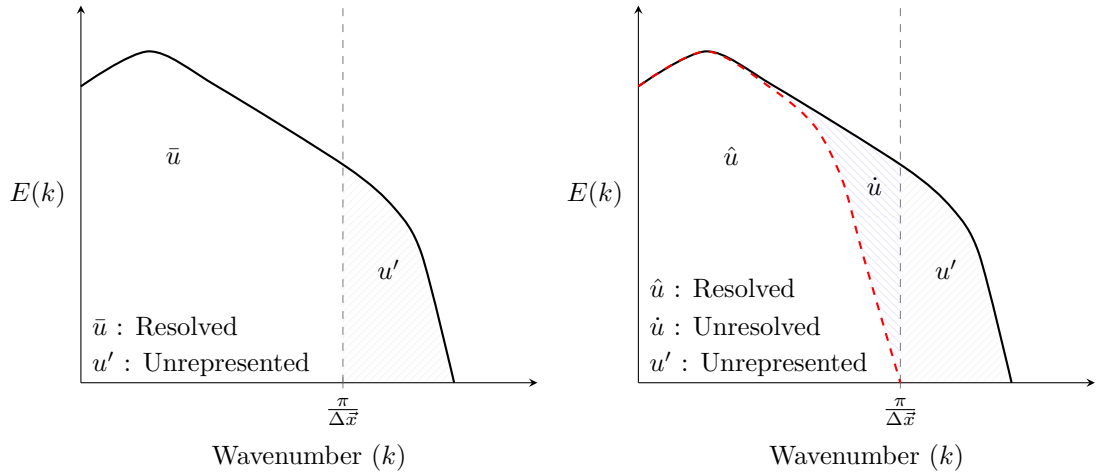

(a) Ideal spectral-like filtering

(b) Realistic filtered system

Figure 2.1: Effects of analytical filter and numerical discretization.

represented by another decomposition

$$\overline{u} = \hat{u} + \dot{u} \,, \tag{2.12}$$

where $\hat{u}$ is the resolved portion of $\overline{u}$ and $\dot{u}$ is the unresolved, but still representable, portion. That is, some information representable on the discrete solution space is no longer resolvable.

Practical CFD implementation must consider Fig. 2.1b and that the effects of the discretization can never be purely isolated. Rather, the discretization, the numerical method, and any turbulence models and explicit filtering utilized must interact in a manner that maintains the intended purpose of each element. If a turbulence model requires some sense of an unresolved turbulent flow to perform properly, then it must be isolated from those elements of the numerical scheme that tend to remove or suppress unresolved solution information for the sake of numerical stability (e.g. limiters).

Additionally, it is critical to demonstrate solution convergence in some sense of the concept. Ideally, a method would demonstrate grid-independence where the generated solution would be independent of the mesh on which it was solved. Achieving the same solution with different numerical methods would demonstrate scheme-independence and would provide further confidence that

the schemes are predicting the "correct" solution of the chosen model. Such goals have generally been elusive for most problems within the LES community. As turbulence models and numerical methods are advanced, it is possible that these goals will regularly be demonstrated. This dissertation presents a method of achieving these goals through using a model for the SGS scales in a manner that is consistent with the numerical discretization and the other algorithmic components. Specifically, the scale at which the model is evaluated is moved to lower wavenumbers so that, relative to the representable information on the mesh, the amount of resolved information increases. This effectively isolates the model from the discretization and other numerical components (e.g. numerical stabilization). In terms of the numerical implementation, the model is evaluated on a mesh that is some integer-ratio coarser than the discretization of the main CFD problem. For example, the current dissertation tests the effects of evaluating the model at the resolution of the CFD mesh, and at resolutions which are twice as coarse and four times as coarse as the CFD mesh. These coarsened meshes are visualized by moving the scale of the model evaluation to the left in Fig. 2.1b. Eventually, all representable scales on the coarser evaluation mesh will be resolved. Reaching that point and achieving grid and scheme-independence as a result is the fourth goal of this dissertation as presented in Chapter 1.

2.4 Favre-Filtering

Around the time the convolution filter was suggested as the framework for LES scale-separation, it was suggested that the Reynolds operator should utilize mass-density weighting when applied to compressible flows [42]. A fact largely ignored in the literature is that Reynolds originally used a mass-density weighting for his averages [43]. Also largely ignored in the literature is the fact Reynolds took his averaging operator to apply to both time and space [5, 43].

The resulting mass-weighted averaging, Favre-averaging, was subsequently applied to LES filtering. The Favre-filtered velocity is defined as

$$\tilde{u}(\vec{x},t) = \frac{\overline{\rho u}}{\bar{\rho}} = \frac{\int_{-\infty}^{\infty}\int_{-\infty}^{\infty} \rho u(\vec{\xi},\tau) G(\vec{x}-\vec{\xi},t-\tau) d\tau d\vec{\xi}}{\bar{\rho}(\vec{x},t)} \,. \tag{2.13}$$

This dissertation assumes the use of a linear Favre-filter for filtering operations applied to governing equations. It is also assumed, for the purposes of turbulence model derivation, that the filter is projective in nature.

Chapter 3

Governing Equations

3.1 Unfiltered Governing Equations

This research is focused on a single-species, non-reacting, calorically perfect, ideal gas which, in the physical space Cartesian coordinate-system, $\vec{x}$, is governed by

$$\frac{\partial \rho}{\partial t} + \frac{\partial \rho u_i}{\partial x_i} = 0 \,, \tag{3.1}$$

$$\frac{\partial \rho u_i}{\partial t} + \frac{\partial}{\partial x_j}\left(\rho u_i u_j + p\delta_{ij} - \tau_{ij}\right) = 0 \,, \tag{3.2}$$

$$\frac{\partial \rho e}{\partial t} + \frac{\partial}{\partial x_i}\left(\rho e u_i + p u_i + q_i - \tau_{ij} u_j\right) = 0 \,, \tag{3.3}$$

which are conservation equations for mass, momentum, and energy respectively, where ρ is the fluid mass density, u_i is the i-th velocity-vector component, p is the thermodynamic pressure, e is the total energy per unit mass, and δ_{ij} is the Kronecker delta. The heat flux, q_i, is modeled with Fourier's law

$$q_i = -\kappa \frac{\partial T}{\partial x_i} \,, \tag{3.4}$$

where κ is the fluid thermal conductivity, and T is the fluid temperature. Additionally, assuming the fluid is Newtonian, the molecular stress-tensor, τ_{ij}, is modeled according to

$$\tau_{ij} = 2\mu\left(S_{ij} - \frac{1}{3}\delta_{ij}\left(\frac{\partial u_k}{\partial x_k}\right)\right) \quad , \quad S_{ij} = \frac{1}{2}\left(\frac{\partial u_i}{\partial x_j} + \frac{\partial u_j}{\partial x_i}\right) \,, \tag{3.5}$$

where μ is the fluid's molecular viscosity. Noting that γ is the fluid specific-heat ratio, pressure is computed using

$$p = (\gamma - 1)\left(\rho e - \frac{1}{2}\rho u_i u_i\right) \,. \tag{3.6}$$

However, to accommodate complex geometries while utilizing structured discretizations and AMR, this work employs generalized curvilinear coordinates to transform Eqs. (3.1–3.3) to the computational space, $\vec{\xi}$,

$$\frac{\partial J\rho}{\partial t} + \frac{\partial}{\partial \xi_j}\left[\mathrm{N}_{ji}^{\top}\left(\rho u_i\right)\right] = 0 \,, \tag{3.7}$$

$$\frac{\partial J\rho u_i}{\partial t} + \frac{\partial}{\partial \xi_k}\left[\mathrm{N}_{kj}^{\top}\left(\rho u_i u_j + p\delta_{ij} - \mathcal{T}_{ij}\right)\right] = 0 \,, \tag{3.8}$$

$$\frac{\partial J\rho e}{\partial t} + \frac{\partial}{\partial \xi_k}\left[\mathrm{N}_{ki}^{\top}\left(\rho e u_i + p u_i + \mathcal{Q}_i - \mathcal{T}_{ij}u_j\right)\right] = 0 \,, \tag{3.9}$$

where J is the Jacobian of the grid mapping, $J = \det(\vec{\nabla}_{\xi}\vec{x})$, and $\mathrm{N}_{ij}^{\top}$ is the mapping transformation matrix, $\mathrm{N}_{ij}^{\top} = J\frac{\partial \xi_i}{\partial x_j}$, with $\top$ representing the matrix transpose operator. The mapped viscous stress tensor, $\mathcal{T}_{ij}$, is written as

$$\mathcal{T}_{ij} = 2\mu\left(\mathcal{S}_{ij} - \frac{1}{3}\delta_{ij}\left(\frac{\partial u_k}{\partial \xi_l}\right)\frac{\mathrm{N}_{lk}^{\top}}{J}\right) \quad , \quad \mathcal{S}_{ij} = \frac{1}{2}\left(\frac{\partial u_i}{\partial \xi_k}\frac{\mathrm{N}_{kj}^{\top}}{J} + \frac{\partial u_j}{\partial \xi_k}\frac{\mathrm{N}_{ki}^{\top}}{J}\right) \,, \tag{3.10}$$

and the mapped heat flux, $\mathcal{Q}_i$, is written as

$$\mathcal{Q}_i = -\kappa\frac{\partial T}{\partial \xi_k}\frac{\mathrm{N}_{ki}^{\top}}{J} \,. \tag{3.11}$$

3.2 Favre-Filtered Governing Equations

Applying a linear, commutative, Favre-weighted filtering operator $(\tilde{\cdot})$ to the spatial domain of Eq. (3.6) and Eqs. (3.7–3.11) provides multiple forms of filtered equations depending on the method of computing total energy. As in most published studies [20], the present dissertation does not density-weight the filtered pressure, $\bar{p}$. No temporal filtering is applied in this dissertation.

These choices result in

$$\frac{\partial J\bar{\rho}}{\partial t} + \frac{\partial}{\partial \xi_j}\left[\mathrm{N}_{ji}^{\top}\left(\bar{\rho}\tilde{u}_i\right)\right] = 0\,, \tag{3.12}$$

$$\frac{\partial J\bar{\rho}\tilde{u}_i}{\partial t} + \frac{\partial}{\partial \xi_k}\left[\mathrm{N}_{kj}^{\top}\left(\bar{\rho}\tilde{u}_i\tilde{u}_j + \bar{p}\delta_{ij} - \widetilde{\mathcal{T}}_{ij} + \tilde{\tau}_{\mathrm{sgs}_{ij}}\right)\right] = 0\,, \tag{3.13}$$

$$\frac{\partial J\bar{\rho}\tilde{e}}{\partial t} + \frac{\partial}{\partial \xi_k}\left[\mathrm{N}_{ki}^{\top}\left(\bar{\rho}\tilde{e}\tilde{u}_i + \bar{p}\tilde{u}_i + \widetilde{\mathcal{Q}}_i - \widetilde{\mathcal{T}}_{ij}\tilde{u}_j + \widetilde{E}_{\text{sgs-1}_i} + \widetilde{E}_{\text{sgs-2}_i} - \widetilde{E}_{\text{sgs-3}_i}\right)\right] = 0\,, \tag{3.14}$$

$$\bar{p} = (\gamma - 1)\left(\bar{\rho}\tilde{e} - \frac{1}{2}\bar{\rho}\tilde{u}_i\tilde{u}_i - \widetilde{E}_{\text{sgs-4}}\right)\,, \tag{3.15}$$

$$\tilde{\tau}_{\mathrm{sgs}_{ij}} = \bar{\rho}\left[\widetilde{u_iu_j} - \tilde{u}_i\tilde{u}_j\right]\,, \tag{3.16}$$

$$\widetilde{E}_{\text{sgs-1}_i} = \bar{\rho}\left[\widetilde{u_ie} - \tilde{u}_i\tilde{e}\right] \quad , \quad \widetilde{E}_{\text{sgs-2}_i} = \widetilde{u_ip} - \tilde{u}_i\tilde{p} \quad , \quad \widetilde{E}_{\text{sgs-3}_i} = \widetilde{\mathcal{T}_{ij}u_j} - \widetilde{\mathcal{T}}_{ij}\tilde{u}_j\,, \tag{3.17}$$

$$\widetilde{E}_{\text{sgs-4}} = \frac{1}{2}\bar{\rho}\left[\widetilde{u_iu_i} - \tilde{u}_i\tilde{u}_i\right]\,, \tag{3.18}$$

$$\widetilde{\mathcal{Q}}_i = -\kappa\frac{\partial\widetilde{T}}{\partial\xi_k}\frac{\mathrm{N}_{ki}^{\top}}{J}\,, \tag{3.19}$$

$$\widetilde{\mathcal{T}}_{ij} = 2\mu\left(\widetilde{\mathcal{S}}_{ij} - \frac{1}{3}\delta_{ij}\left(\frac{\partial\tilde{u}_k}{\partial\xi_l}\right)\frac{\mathrm{N}_{lk}^{\top}}{J}\right) \quad , \quad \widetilde{\mathcal{S}}_{ij} = \frac{1}{2}\left(\frac{\partial\tilde{u}_i}{\partial\xi_k}\frac{\mathrm{N}_{kj}^{\top}}{J} + \frac{\partial\tilde{u}_j}{\partial\xi_k}\frac{\mathrm{N}_{ki}^{\top}}{J}\right)\,, \tag{3.20}$$

which is the final system utilized in all of the cases presented in the current dissertation. The SGS terms arising as a result of filtering are closed through applying explicit turbulence models. The models used for these terms in this dissertation are presented in the following chapter.

Chapter 4

Models For Unresolved Nonlinear Terms

The present chapter provides the theoretical and mathematical formulation of the models developed for Eqs. (3.16–3.18) and used to close Eqs. (3.13–3.15). As such, this chapter presents an overview of the history of the development of the stretched-vortex subgrid-scale model and formulates the model in the context of the compressible Navier-Stokes equations. The stretched-vortex SGS model for no-slip-wall boundaries is also presented and discussed with some attention to the application within a generalized curvilinear coordinate system.

4.1 Subgrid-Scale Stress Tensor

For incompressible flows, the subgrid-scale stress tensor, $\tilde{\tau}_{\text{sgs}_{ij}}$, in Eq. (3.13) is the only unresolved nonlinear term which requires modeling. Representing unresolved fluid motions which contribute to the resolved fluid motions, $\tilde{\tau}_{\text{sgs}_{ij}}$ is critical for unresolved turbulent flows. As such, $\tilde{\tau}_{\text{sgs}_{ij}}$ has received extensive research attention and a multitude of $\tilde{\tau}_{\text{sgs}_{ij}}$ models have been developed. In broad terms, most models have either been functional in nature (attempting to capture the effect of $\tilde{\tau}_{\text{sgs}_{ij}}$ without attempting to accurately reconstruct $\tilde{\tau}_{\text{sgs}_{ij}}$) or structural in nature (attempting to reconstruct $\tilde{\tau}_{\text{sgs}_{ij}}$) [21]. While both types of models have proven useful, attempts to extend the models to further unresolved nonlinear terms enjoy a slight advantage when using structural models. Essentially, it is possible to identify a dominant SGS model vector associated with structural models. This SGS vector makes extensions to the other unresolved nonlinear terms relatively straightforward as will be seen shortly.

4.2 Stretched-Vortex Model

Due to the the robust and well-developed nature of the stretched-vortex SGS model, this work adopts the stretched-vortex model for all tests and studies conducted. The following sections

present the history of the stretched-vortex model development along with extensions to a wide range of physics.

4.2.1 History of Development

The stretched-vortex subgrid/sub-analytical-scale (SVS) model, is a structural LES SGS model developed from the assumption that, at high Reynolds numbers and small length-scales, there exists a flow structure guiding the flow evolution of kinetic energy.

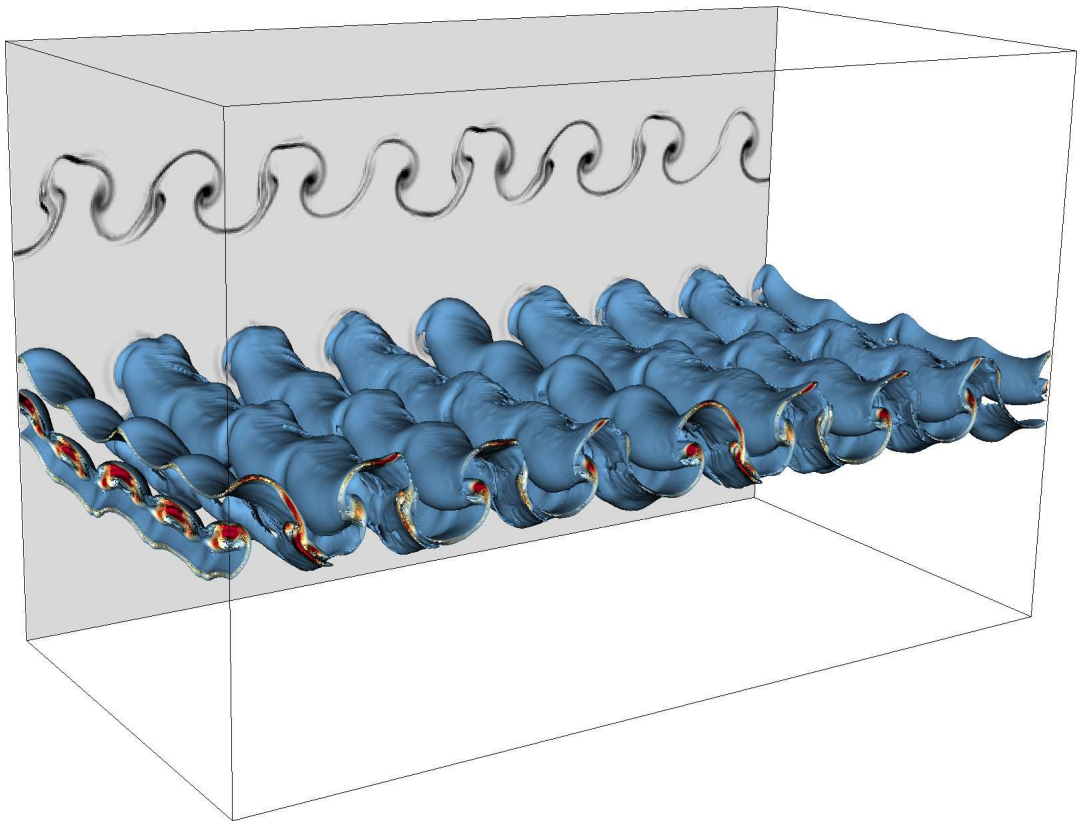

Figure 4.1: Spiral vortices created in a fully periodic double shear flow.

In 1982, Lundgren published an analytical Navier-Stokes solution providing Kolmogorov's -5/3 energy spectrum [44]. Lundgren's solution approach began with the incompressible Navier-Stokes equations and a common shear-flow structure: the spiral vortex. A double-shear flow configuration with typical spiral vortices is depicted in Fig. 4.1, where vortex sheets are rolling

up into vortex cores. Although others had previously modeled fine-scale turbulence using spiral vortices [45], after Lundgren accounted for vortex-strain and time-averaged the solution over the vortex lifetime, he arrived at the desired -5/3 spectrum. Lundgren's spectrum is written as

$$E(\kappa) = \mathcal{K}_0 \epsilon^{2/3} \kappa^{-5/3} \text{exp}\left(-2\kappa^2 \nu / \left(3|\tilde{a}|\right)\right) \ , \tag{4.1}$$

where κ is the wavenumber, $\mathcal{K}_0$ is the Kolmogorov prefactor, ϵ is the energy dissipation rate, ν is the kinematic viscosity of the fluid, and $\tilde{a}$ is the stretching of the subgrid-vortex by the resolved field.

4.2.2 Initial Development

Throughout the 1980's and 1990's, Saffman and Pullin [46–49] further investigated Lundgren's model with the eventual result being Misra and Pullin's stretched-vortex SGS LES model [50]. Misra and Pullin modeled the SGS stress-tensor by approximating the SGS kinetic energy, K, and the orientation unit-vector, $\vec{e^v}$, of the SGS vortices. The model can be presented (in terms of Favre-filtered velocity $\tilde{\vec{u}}$) as

$$\tilde{\tau}_{\text{sgs}_{ij}} = \bar{\rho}\left(\widetilde{u_i u_j} - \tilde{u}_i \tilde{u}_j\right) = \bar{\rho} K \left(\delta_{ij} - e_i^v e_j^v\right) \ , \tag{4.2}$$

where $\delta_{ij} - e_i^v e_j^v$ is a generalized ensemble-average of the SGS vortex orientation probability density function (PDF). In Misra's paper, K was assumed to have the Kolmogorov spectrum

$$E(\kappa) = \mathcal{K}_0 \epsilon^{2/3} \kappa^{-5/3} \ , \tag{4.3}$$

and was determined using a nonlocal procedure well suited for a pseudo-spectral code.

While Misra suggested possible methods for computing K on a physical-space grid, Voelkl and Pullin finished the extension through matching local, second-order velocity structure-functions, F_2,

with an assumed SGS energy spectrum [51],

$$F_2 = \left(\tilde{u}_j\left(\vec{x}_0\right) - \tilde{u_j}\left(\vec{x}_i\right)\right) \cdot \left(\tilde{u_j}\left(\vec{x}_0\right) - \tilde{u_j}\left(\vec{x}_i\right)\right) \ . \tag{4.4}$$

Multiple models for computing K have since been suggested [50–54], but the current study consistently utilizes the model presented by Chung and Pullin [54].

4.2.3 Orientation Models

Originally, Misra and Pullin proposed three models for the ensemble averaged PDF of the SGS vortex orientation vector. It is apparent from Eq. (4.2) that, requiring $K \geq 0$, $e^{\vec{v}}$ alone determines whether the SV model is dissipative or anti-dissipative.

The first of the three models, "model (1a)", used the eigenvectors ($\vec{e}^{\lambda_3}$ and $\vec{e}^{\lambda_2}$) associated with the largest and second-largest eigenvalues (λ_3 and λ_2 respectively) of the strain-rate tensor, $\tilde{\tilde{S}}$. Taking the form

$$\left(\widetilde{u_i u_j} - \tilde{u}_i \tilde{u}_j\right) = K\left[\sigma\left(\delta_{ij} - e_i^{\lambda_3} e_j^{\lambda_3}\right) + (1-\sigma)\left(\delta_{ij} - e_i^{\lambda_2} e_j^{\lambda_2}\right)\right] \ , \tag{4.5}$$

it allowed for unequal weighting to be applied to the eigenvectors through the weighting parameter σ. It was reported that this model provided no kinetic energy back-scatter from the fine to the large turbulent scales, in contrast with DNS results.

The second orientation model, "model (1b)", again included $\vec{e}^{\lambda_3}$. However, instead of relying on $\vec{e}^{\lambda_2}$, it relied on the local, resolved vorticity vector, denoted $e^{\vec{\omega}}$. Assuming the SGS vortices are aligned with the resolved vortices, this orientation model makes physical sense. This model also provided a small amount of energy back-scatter. Similar to the first model, the second model was presented as

$$\left(\widetilde{u_i u_j} - \tilde{u}_i \tilde{u}_j\right) = K\left[\sigma\left(\delta_{ij} - e_i^{\lambda_3} e_j^{\lambda_3}\right) + (1-\sigma)\left(\delta_{ij} - e_i^{\omega} e_j^{\omega}\right)\right] \ . \tag{4.6}$$

Misra's third model, "model (2)", was of a significantly different form than the first two models. Formulated as a time-dependent ordinary differential equation (ODE), the model tracks the evolution of the subgrid-scale vorticity vector over time. The model, given by,

$$\frac{\partial e_i^v}{\partial t} = e_j^v \frac{\partial \tilde{u}_i}{\partial x_j} - e_i^v e_k^v e_j^v \frac{\partial \tilde{u}_k}{\partial x_j} \, , \tag{4.7}$$

was reported to provide significant back-scatter, exceeding the level reported in many DNS simulations. While many further papers report on the results provided by models (1a) and (1b), no further studies provide results derived from the third model, model (2). Several later papers truncated models (1a) and (1b) (Eq. (4.5) and Eq. (4.6) respectively) to a single-direction model based only on the principal eigenvector of the strain-rate tensor by assuming $\sigma = 1$ [54]

$$(\widetilde{u_i u_j} - \tilde{u}_i \tilde{u}_j) = K \left(\delta_{ij} - e_i^{\lambda_3} e_j^{\lambda_3} \right) \, . \tag{4.8}$$

It has been shown that this model is dissipative and numerically stable [52, 55].

Assessment of the models presented above has generally shown that Eq. (4.8) is sufficient for many turbulent flows of interest. Theoretically, this is justifiable in that one would expect the small, unresolved turbulent scales to rapidly respond to and align with the direction of greatest stretching in the flow (the most extensional eigenvector of the strain-rate tensor). However, experimental and numerical studies have generally shown that the bulk of the turbulent vorticity aligns with the intermediate eigenvector of the local strain-rate tensor [56, 57]. For this reason, Eq. (4.5) makes sense as a blending between theoretical and experimentally observed vorticity alignment. The main issue with the experimental and numerical studies has been the locality of the data. If turbulent data is separated into small-scale and large-scale fields, the small-scale turbulence predominantly aligns with the most extensional eigenvector of the large-scale strain-rate tensor [56, 57], confirming the theoretical result that small turbulent scales should react quickly to large-scale flow stretching. Apart from testing the orientation models presented above and unless otherwise noted, the simulations presented in the current study use Eq. (4.8).

4.2.4 Kinetic Energy Estimate

As mentioned, the current dissertation consistently utilizes the SGS kinetic energy approximation model presented by Chung and Pullin [54]. The model requires evaluating the incomplete gamma function, $\Gamma[\cdot]$, the grouped Kolmogorov constant, $\mathcal{K}_0'$, and a cutoff wavenumber, κ_c, and has the form

$$K = \frac{1}{2}\mathcal{K}_0'\Gamma\left[-\frac{1}{3}, \kappa_c^2\right] . \tag{4.9}$$

The cutoff wavenumber, κ_c, is computed using

$$\kappa_c = \frac{\pi}{\Delta_c}\sqrt{\frac{2\nu}{3|\tilde{a}|}} \quad , \quad \tilde{a} = e_i^{\lambda_3}\tilde{S}_{ij}e_j^{\lambda_3} \quad , \quad \nu = \frac{\mu}{\bar{\rho}} \quad , \quad \Delta_c = (\Delta x \Delta y \Delta z)^{1/3} . \tag{4.10}$$

The Kolmogorov constant, $\mathcal{K}_0'$ is given by

$$\mathcal{K}_0' = \frac{\{F_2\}}{\{Q(\kappa_c, d)\}} . \tag{4.11}$$

In Eq. (4.11), $\{\cdot\}$ is an ensemble average of the variables over a spatial domain, Ω, encompassing N points, $\vec{x}_i$, neighboring the evaluation location $\vec{x}_0$

$$\{\phi\} = \frac{1}{N}\sum_{\vec{x}_i \in \Omega \ ; \ \vec{x}_i \neq \vec{x}_0} \phi(\vec{x}_0, \vec{x}_i) , \tag{4.12}$$

where, in this study, $N = 26$. Additionally, Q is a weighting evaluated over all wavenumbers, k, given by

$$Q(\kappa_c, d) = 4\int_0^{\kappa_c} k^{-5/3}\text{exp}\left(-k^2\right)\left(1 - J_0\left(\frac{k}{\kappa_c}\pi d\right)\right)\mathrm{d}k , \tag{4.13}$$

where J_0 is the zeroth-order Bessel function of the first kind, and d is the planar distance from the cell center to the SGS vortex axis

$$d = \frac{r}{\Delta_c} \quad , \quad r^2 = [(\vec{x}_0 - \vec{x}_i)\cdot(\vec{x}_0 - \vec{x}_i)] - \left[(\vec{x}_0 - \vec{x}_i)\cdot e^{\vec{\lambda}_3}\right]^2 . \tag{4.14}$$

Efficient means of computing $\mathcal{K}_0'$, $\Gamma[\cdot]$, and the eigenvalues/eigenvectors are presented by Voelkl and others [51, 53, 58].

4.3 Subgrid-Scale Energy Terms and Compressible Extensions

Once an SGS model vector has been identified, extensions to SGS transport, variable density flows, and compressible flows come naturally.

4.3.1 Subgrid-Scale Scalar Transport and Energy Transport

In addition to Lundgren's original stretched-vortex analysis, Pullin and Lundgren analyzed the effect of allowing for axial flow of velocity through the subgrid-scale vortices and allowing for associated scalar transport. Their findings matched previous theoretical work quite well and motivated an SGS model for passively transported scalars [59, 60].

Assuming a passive scalar, ϕ, is wound around the vortex, Pullin derived the model

$$\widetilde{\phi u_i} - \tilde{\phi}\tilde{u}_i = \frac{\Delta_c}{2} K^{1/2} \left(\delta_{ij} - e_i^v e_j^v\right) \partial_j \tilde{\phi} \,, \tag{4.15}$$

where Δ is the local mesh spacing. Assuming a calorically perfect, single-species flow, the $\widetilde{E}_{\text{sgs-1}_i}$ and $\widetilde{E}_{\text{sgs-2}_i}$ terms from Eq. (3.14) can be combined and rewritten in the form

$$\begin{aligned} \widetilde{E}_{\text{sgs-1}_i} + \widetilde{E}_{\text{sgs-2}_i} &= \bar{\rho}\left[\widetilde{u_i e} - \tilde{u}_i \tilde{e}\right] + \widetilde{u_i p} - \tilde{u}_i \tilde{p} \\ &= \frac{\gamma R}{\gamma - 1} \bar{\rho} \left[\widetilde{u_i T} - \tilde{u}_i \tilde{T}\right] + \frac{1}{2} \bar{\rho} \left[\widetilde{u_j u_j u_i} - \widetilde{u_j u_j}\, \tilde{u}_i\right] \end{aligned} \tag{4.16}$$

Kosovic et al. [61] and Hill et al. [62] modeled the first term on the right using the passive-scalar-transport model in Eq. (4.15). The SGS triple correlation of Eq. (4.16) (the second term on the right) has generally been assumed to be of such small magnitude as to be unnecessary to model [61, 63]. The present study follows both of these modeling choices when modeling

Eq. (4.16) to arrive at

$$\widetilde{E}_{\text{sgs-1}_i} + \widetilde{E}_{\text{sgs-2}_i} = \frac{\gamma \bar{\rho} R \Delta_c}{2\left(\gamma - 1\right)} K^{1/2} \left(\delta_{ij} - e_i^v e_j^v\right) \frac{\partial \tilde{T}}{\partial x_j} \,. \tag{4.17}$$

Hill et al. [62] extended the preceding approximations to model the SGS species convective flux in species transport equations, while Lombardini et al. [63] made an additional extension to account for nonlinearities in SGS molecular heat flux. As the current study investigates calorically perfect, single-species flows, these models are not included here, but future studies of thermally perfect, multi-species flows could include these additional model terms in addition to other terms developed for SGS variation in molecular diffusion coefficients and similar physics.

It is important to note that, while the SGS model Eq. (4.17) is used for all unbounded turbulent flows, this model is turned off for wall-bounded turbulent flows presented in the current dissertation. For these flows and for the resolutions tested here, this model adversely affected the near-wall prediction of the momentum thickness.

4.3.2 Subgrid-Scale Correction for Pressure

Kosovic et al. [61] and Hill, et al. [62] modeled $\widetilde{E}_{\text{sgs}_4}$ using the SGS kinetic energy approximation, K. The results throughout this study do not utilize $\widetilde{E}_{\text{sgs}_4}$ as early simulations showed no measurable difference when this term was utilized. For all but those problems with compressible turbulence (those with turbulent Mach numbers greater than 0.3), this observation is expected [20]. However, for future tests with large turbulent Mach numbers, including the SGS kinetic energy approximation for $\widetilde{E}_{\text{sgs}_4}$ would be necessary.

4.3.3 Subgrid-Scale Turbulence-Chemistry Interactions

While the author is unaware of additional extensions to account for SGS interactions between reactions and turbulence, it is expected that such extensions could be developed using principles similar to those used to derive the original model and the subsequent extensions. Additionally, other concepts of SGS topology and phenomena could be combined with the stretched-vortex

concept to create new, hybrid forms of the SV SGS model. However, this is out of the scope of the present work.

4.4 Modeling or Approximating Boundary Conditions

Following completion of modeling the unresolved SGS terms in Eqs. (3.12–3.15), it is necessary to properly define boundary conditions. Coupled with governing equations, boundary conditions and initial conditions define a flow problem. Without these, a computational problem may be ill-posed. Therefore, properly modeling boundary conditions for unresolved systems is of just as much priority as modeling unresolved terms in the governing equations.

A no-slip wall boundary is one type of boundary that requires careful numerical treatment and SGS modeling. With a zero-velocity condition at the wall and a freestream velocity some distance away from the wall, a velocity gradient forms normal to the wall and freestream momentum is dissipated away in the near-wall region by the presence of the wall. At sufficiently high Reynolds numbers, this boundary-layer flow transitions from a smooth, laminar flow profile to a turbulent one. For a turbulent boundary-layer, between the wall and the freestream velocity state some distance away from the wall, there exists a zone of complex physical interaction containing small-scale turbulence interacting with large-scale turbulence. Accurately predicting these turbulent scales is critical to properly simulating the properties of the boundary-layer and the subsequent effects of the boundary-layer on the overall problem. Predictions of drag force, flow separation and reattachment, near-wall viscous heating, and many other important physical phenomenon rely on an accurate prediction of the turbulent boundary-layer profile. With insufficient mesh resolution, the boundary-layer must be modeled in some form or another. Without a model or sufficient resolution, the wall-shear-stress will naturally be under-predicted and many other boundary-layer properties relying on the shear-stress prediction will be incorrect.

4.4.1 No-Slip Wall Boundaries

No-slip wall boundaries introduce some additional theoretical and practical issues for LES beyond those presented by unbounded, decaying turbulence. Practically speaking, the smallest unresolved scales nearest the boundary disproportionately affect the largest scales within the boundary-layer. Additionally, numerical methods typically exhibit larger numerical error near boundaries due to biased or one-sided spatial approximations.

From the theoretical perspective, LES works with spatially filtered quantities. What happens to the filtering operator near a wall? Does it become biased and eventually one-sided? Does the support region of the filter shrink until it eventually reaches a point or a surface at the wall? Or, should LES exclude the near-wall region altogether? Fig. 4.2 provides a visual demonstration of the various LES interpretations in the context of a cell-based discretization ($\{u\}$ is the time-averaged velocity of the boundary-layer, Δy is the cell height from the wall, j is the index of the wall face, and Δ_f is the LES filter width). Note that, at the center of the wall-adjacent cell in Fig. 4.2, all the filtering methods which are depicted provide the same result. This is to be expected as it is at this point where all the filter definitions coincide with one another. The cell-averaged value, the biased filtering, and the shrinking filter are all able to use the exact same filter size and the exact same data. Below the center of the wall-adjacent cell, the filter size and/or shape of the biased filter and the shrinking filter must change. This sudden beginning to the changing of the filter definition provides a strikingly visible "kink" in the filtered mean velocity profiles at this point. To date, the typical approach to LES assumes the filter must shrink near the wall and the velocity boundary condition must be zero at the wall. The result is that wall shear-stresses must be accurately modeled if the basics of the boundary-layer are to be accurately predicted.

A different interpretation, proposed by Bose & Moin [65], allows the filter size to shrink near the wall while providing a non-zero velocity value at the wall. The resulting "slip-wall" model performs quite well for a range of flows, but shows sensitivity to the choice of subgrid-scale model for the governing equations and the numerical discretization utilized [66]. Additionally, a wall-penetration condition is not only justified, but theoretically necessary to achieve proper growth

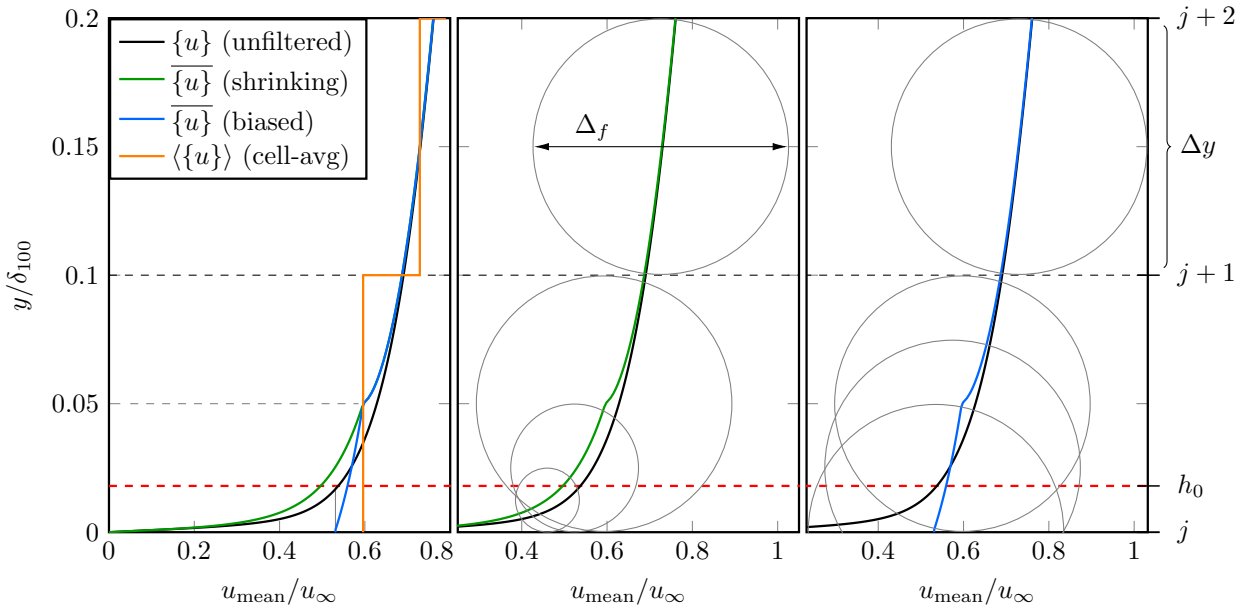

Figure 4.2: Filtering the turbulent boundary-layer mean-velocity in near-wall cells (Musker velocity-profile [64], $Re_\tau \approx 3500$). The cell height is Δy and the wall face-index is j. The filter width, Δ_f, shrinks approaching the wall in the middle panel while it becomes biased approaching the wall in the third panel. In this figure, all velocity data is to scale and $h_0 = 0.18\Delta y$.

rates of the boundary-layer [66]. The possibility of losing mass conservation at the wall boundary leads to the potential for a degradation in physics prediction and overall algorithm robustness for particularly sensitive problems.

Taking another approach, Chung & Pullin [53] assumed a small, near-wall region of the LES domain could be excluded from the simulation. Instead of modeling this small, near-wall region, the boundary of the domain is assumed to be a lifted, "virtual wall" where a slip-velocity is computed. At this virtual wall location, the interior model is also applied at the boundary. Since there is a slip velocity, the wall shear-stress is much less than the actual wall shear-stress and it is necessary to apply the interior model if the correct amount of momentum is to be transported through the virtual wall and out of the domain. In Fig. 4.2, h_0 is the assumed height of the virtual wall where the slip-velocity is computed based on the mean turbulent boundary-layer (TBL) velocity profile ($\{u\}$). One of the main theoretical drawbacks of this method is that a raised, virtual wall should theoretically require the mesh to be slightly offset from the geometry of interest, and this slight offset could complicate mesh generation for complex geometries [67]. In all published literature

however, it is assumed that the virtual-wall slip-velocity is applied at the physical wall location and no modification to mesh generation is utilized. The implementation of this model in this dissertation follows the methodology of Chung & Pullin [53]. The virtual-wall slip-velocity will be applied at what is assumed to be the physical wall face. Similar to the slip-wall model of Bose & Moin, this model has also performed quite well for a range of flows.

It was noted in the current study that, as seen in Fig. 4.2, the biased filtering (where the filter eventually becomes one-sided at the wall rather than shrinking to zero) provides a slip-velocity which is quite close to the mean TBL profile at the virtual wall height. The author of this dissertation tested Re_τ ranging from 200 to one million and discretization sizes ranging from one five-hundredth of the boundary-layer thickness to one-half the boundary-layer thickness. All of these tests showed a remarkably similar result. It was recognized that this result is a consequence of a log profile. Assuming a general log profile for the mean turbulent boundary-layer-velocity of the form

$$u\left(y\right) = \alpha \log\left(\beta y\right) + c\,, \tag{4.18}$$

it is possible to assume a one-sided filtering operation (of filter width $0.5\Delta y$) at the wall and inside a mesh cell of height Δy,

$$\begin{aligned} \bar{u}\left(y\right) &= \frac{2}{\Delta y}\int_0^{\frac{\Delta y}{2}} u\left(y\right)\mathrm{d}y = \frac{2}{\Delta y}\left[\frac{\Delta y}{2}\left(\alpha \log\left(\frac{\beta \Delta y}{2}\right) - \alpha + c\right)\right] \\ &= \alpha \log\left(\frac{\beta \Delta y}{2}\right) - \alpha + c\,. \end{aligned} \tag{4.19}$$

Matching this velocity with the velocity provided by Eq. (4.18), it is instructive to inquire at what height off the wall would Eq. (4.18) have provided the same velocity as the filtered velocity at the wall as shown in Eq. (4.19). Matching the velocities provides

$$\log\left(\beta y\right) = \log\left(\frac{\beta \Delta y}{2}\right) - 1\,, \tag{4.20}$$

from which it is apparent that y is given by

$$y = \frac{\Delta y}{2} e^{-1} \, . \tag{4.21}$$

Therefore, it is seen that, for any logarithmic velocity profile conforming to Eq. (4.18), the ratio of the y height versus the cell height is given as

$$\frac{y}{\Delta y} = \frac{e^{-1}}{2} = 0.18393972 \ldots \, , \tag{4.22}$$

which is extremely close to the 0.18 value which Chung & Pullin and subsequent researchers have found optimal for this model [53, 68]. As a result, it is justifiable to reinterpret this model in this dissertation as the application of a one-sided filtering operation at the domain boundary, which, consistent with the mathematical foundations of LES, provides a non-zero-velocity boundary condition. A consequence of this reinterpretation is that there is no inconsistency in the model when applying the slip-velocity at the physical wall location.

4.4.2 Stretched-Vortex Wall-Model

Motivated by the SGS scalar model work, Chung and Pullin extended the original SVS model to incorporate Pullin and Lundgren's earlier analytical analysis of axial flow of velocity through subgrid vortices. This extended stretched-vortex model led to the development of a particularly capable wall-model [53].

The stretched-vortex wall-model developed by Chung & Pullin hinges on the specification of a slip-velocity at a virtually raised wall that, in practice, is placed at the wall boundary of the simulation domain. Fig. 4.3 presents the basic construction of the wall-model. The lifted virtual wall is assumed to be located at a wall-normal height of h_0, while the viscous sublayer of the boundary-layer is assumed to be located beneath the virtual wall and at a height of h_ν. As detailed by Chung & Pullin, region (I) is the viscous sublayer, while region (III) is the LES outer-flow region used for computing the wall-model update terms [53]. Region (II) is a presumed overlap region

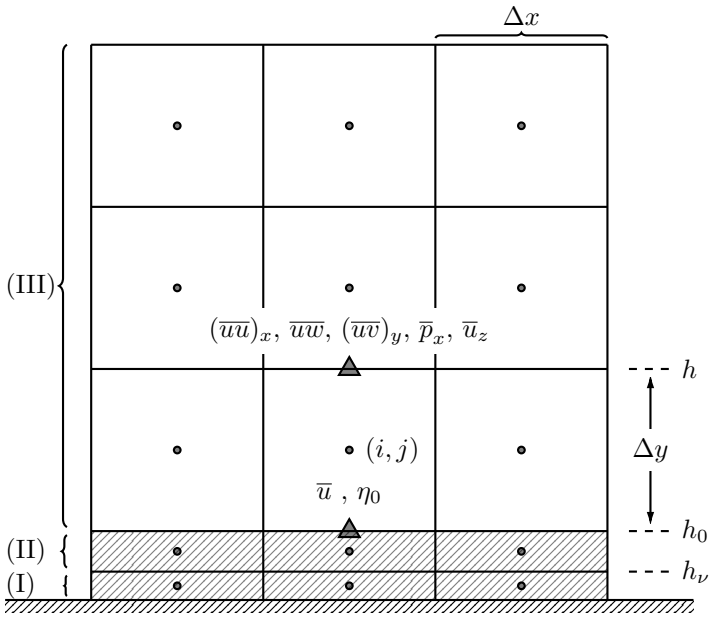

Figure 4.3: Numerical construction of the stretched-vortex wall-model.

which uses the extended stretched-vortex model and where a logarithmic velocity profile is derived based on the extended stretched-vortex model. Assuming the unresolved velocity in the first wall-adjacent cell follows this law-of-the-wall logarithmic profile, the slip-velocity is computable if the local wall shear-stress can be approximated.

One approach to approximate the local wall shear-stress is formulating a temporal evolution equation in terms of the momentum evolution equation. For this, Chung & Pullin assumed that the velocity in a wall-adjacent cell is in a state of quasi-equilibrium and that it is roughly a function of the wall shear-stress alone. In this dissertation, this same assumption is applied to the wall-parallel-filtered streamwise momentum (just as was done by McCann [69]) and using the chain rule, it can be shown that

$$\frac{\partial \hat{q}}{\partial t} = \frac{\partial \hat{q}}{\partial \hat{\eta}_0}\frac{\partial \hat{\eta}_0}{\partial t} \quad , \quad \eta_0 = \left| \frac{\partial \sqrt{u_s^2 + u_p^2}}{\partial n|_{n=0}} \right| \quad , \quad q = \sqrt{(\rho u_s)^2 + (\rho u_p)^2}\,, \tag{4.23}$$

where $\hat{\cdot}$ is a variable filtered in the wall-parallel plane for the purposes of this derivation, η_0 is the wall-normal derivative of the wall-tangential velocity magnitude, q is the magnitude of the wall-tangential momentum, and u_s, u_p, and u_n are the streamwise, spanwise, and wall-normal

components of the wall-oriented velocity vector and are associated with the coordinate directions s, p, and n respectively. Since the form of the momentum evolution equation is already known from the governing equations, the only term for the first part of Eq. (4.23) which requires a model is $\partial\hat{\eta}_0/\partial\hat{q}$.

Just as done by Chung & Pullin [53] (for the streamwise velocity) and McCann [69] (for the streamwise momentum component aligning with the Cartesian coordinate x), this dissertation assumes that an inner-scaling ansatz applies to the magnitude of the local streamwise momentum within a wall-adjacent cell

$$\hat{q} = \hat{\rho}_w \hat{u}_\tau \hat{F}\left(n^+\right) \quad , \quad n^+ = \frac{\hat{\rho}_w \hat{u}_\tau n}{\hat{\mu}_w} \quad , \quad \hat{u}_\tau = \sqrt{\frac{\hat{\mu}_w \hat{\eta}_0}{\hat{\rho}_w}} \, , \tag{4.24}$$

where u_τ is the wall-friction-velocity, and where $\hat{F}\left(n^+\right)$ is an unknown function. Additionally, variables with a subscript w such as ρ_w are wall-variables in that they are evaluated at the wall. Note that this dissertation follows the extension by Cheng et al. [70] to apply the ansatz to the local streamwise velocity vector to incorporate multidimensional effects, except that this dissertation applies the ansatz to momentum. Differentiating the ansatz (the first function of Eq. (4.24)) with respect to η_0, and grouping terms, $\frac{\partial\hat{q}}{\partial\hat{\eta}_0}$ is given as,

$$\begin{aligned} \frac{\partial\hat{q}}{\partial\hat{\eta}_0} &= \hat{F}\left(n^+\right)\frac{\partial\hat{\rho}_w\hat{u}_\tau}{\partial\hat{\eta}_0} + \hat{\rho}_w\hat{u}_\tau\frac{\partial\hat{F}\left(n^+\right)}{\partial\hat{\eta}_0} = \frac{\hat{\rho}_w\hat{u}_\tau}{2\hat{\eta}_0}\hat{F}\left(n^+\right) + \hat{\rho}_w\hat{u}_\tau\frac{\partial\hat{F}\left(n^+\right)}{\partial n^+}\frac{\partial n^+}{\partial\hat{\eta}_0} \\ &= \frac{\hat{\rho}_w\hat{u}_\tau}{2\hat{\eta}_0}\hat{F}\left(n^+\right) + \frac{\hat{\rho}_w\hat{u}_\tau n^+}{2\hat{\eta}_0}\frac{\partial\hat{F}\left(n^+\right)}{\partial n^+} = \frac{\hat{\rho}_w\hat{u}_\tau}{2\hat{\eta}_0}\left[\hat{F}\left(n^+\right) + n^+\frac{\partial\hat{F}\left(n^+\right)}{\partial n^+}\right] . \end{aligned} \tag{4.25}$$

Furthermore, as done by Chung & Pullin [53], the unknown function $\hat{F}\left(n^+\right)$ is eliminated through the clever use of wall-normal integration. Integrating from the wall to some interior wall-distance

h provides

$$\begin{aligned}\frac{1}{h}\int_0^h \frac{\partial \hat{q}}{\partial \hat{\eta}_0}\,\mathrm{d}n &= \frac{\hat{\rho}_w\hat{u}_\tau}{2h\hat{\eta}_0}\int_0^h \left[\hat{F}\left(n^+\right) + n^+\frac{\partial \hat{F}\left(n^+\right)}{\partial n^+}\right]\mathrm{d}n = \frac{\hat{\rho}_w\hat{u}_\tau}{2h\hat{\eta}_0}\int_0^h \frac{\partial}{\partial n^+}\left[n^+\hat{F}\left(n^+\right)\right]\mathrm{d}n \\ &= \frac{\hat{\rho}_w\hat{u}_\tau}{2h\hat{\eta}_0}\int_0^{h^+} \frac{\partial}{\partial n^+}\left[n^+\hat{F}\left(n^+\right)\right]\frac{\hat{\mu}_w}{\hat{\rho}_w\hat{u}_\tau}\,\mathrm{d}n^+ = \frac{\hat{\rho}_w\hat{u}_\tau}{2h^+\hat{\eta}_0}\int_0^{h^+} \frac{\partial}{\partial n^+}\left[n^+\hat{F}\left(n^+\right)\right]\mathrm{d}n^+ \\ &= \frac{\hat{\rho}_w\hat{u}_\tau}{2h^+\hat{\eta}_0}\left[h^+\hat{F}\left(h^+\right)\right] = \frac{\hat{\rho}_w\hat{u}_\tau}{2\hat{\eta}_0}\hat{F}\left(h^+\right) = \frac{\hat{q}|_h}{2\hat{\eta}_0}\,.\end{aligned} \tag{4.26}$$

At this point, it is important to emphasize the irrelevance of the exact form of the unknown function chosen for the inner scaling ansatz. Any function of the inner scaling variable would satisfy the above derivation. As such, there are a wide range of flows that are well modeled by these equations. Substituting this result into the wall-normal integrated form of Eq. (4.23) provides

$$\frac{1}{h}\int_0^h \frac{\partial \hat{q}}{\partial t}\,\mathrm{d}n = \frac{\partial\langle q\rangle}{\partial t} = \frac{\hat{q}|_h}{2\hat{\eta}_0}\frac{\partial \hat{\eta}_0}{\partial t}\,, \tag{4.27}$$

where $\langle\phi\rangle$ is a volume-filtered or volume-averaged variable and is the same as a cell-averaged quantity used in the finite-volume method in this dissertation. Rearranging in a more usable form, we find

$$\frac{\partial \hat{\eta}_0}{\partial t} = \frac{2\hat{\eta}_0}{\hat{q}\big|_h}\frac{\partial\left\langle q\right\rangle}{\partial t}\,. \tag{4.28}$$

With this evolution equation in hand, it is necessary to compute the temporal update for the wall-tangential momentum magnitude. Taking the time derivative of q provides

$$\frac{\partial\langle q\rangle}{\partial t} = \left\langle \frac{\rho u_s}{q}\frac{\partial \rho u_s}{\partial t}\right\rangle + \left\langle \frac{\rho u_p}{q}\frac{\partial \rho u_p}{\partial t}\right\rangle\,. \tag{4.29}$$

This study argues that Eq. (4.29), as a momentum magnitude update, should match as closely as possible to the momentum update used elsewhere in the LES system. In this way, the nature of the dynamics of the LES velocity are preserved as much as possible in the η_0 update equation. To

achieve this goal, this dissertation recognizes that the $\rho u_s/q$ term and the $\rho u_p/q$ term constitute a unit-vector weighting of the momentum evolution equations. In keeping with the derivation of the η_0 update equation, Eq. (4.27), these terms are evaluated at $n = h$. Furthermore, this study argues that evaluating the unit-vector weighting term at $n = h$ is numerically justified in that it presents a more accurate evaluation of the outer-flow ratio of spanwise velocity and streamwise velocity. As a result, Eq. (4.29) is simplified to

$$\frac{\partial \langle q \rangle}{\partial t} = \frac{\rho \hat{u}_s|_h}{\hat{q}|_h} \frac{\partial \langle \rho u_s \rangle}{\partial t} + \frac{\rho \hat{u}_p|_h}{\hat{q}|_h} \frac{\partial \langle \rho u_p \rangle}{\partial t} \, . \tag{4.30}$$

Furthermore, it is fairly straightforward to extend this to match the mapped form of the momentum equations as presented in Eq. (3.13)

$$\frac{\partial \langle Jq \rangle}{\partial t} = \frac{\rho \hat{u}_s|_h}{\hat{q}|_h} \frac{\partial \langle J\rho u_s \rangle}{\partial t} + \frac{\rho \hat{u}_p|_h}{\hat{q}|_h} \frac{\partial \langle J\rho u_p \rangle}{\partial t} \, . \tag{4.31}$$

Inserting this into the mapped form of the η_0 update equation provides

$$\frac{\partial \hat{J\eta}_0}{\partial t} = \frac{2\hat{\eta}_0}{\hat{q}\big|_h} \left[\frac{\rho \hat{u}_s|_h}{\hat{q}|_h} \frac{\partial \langle J\rho u_s \rangle}{\partial t} + \frac{\rho \hat{u}_p|_h}{\hat{q}|_h} \frac{\partial \langle J\rho u_p \rangle}{\partial t} \right] \, . \tag{4.32}$$

The next step in the derivation of the η_0 update equation is to identify the wall-tangential momentum equation update terms. Using a transformation, M_{ij}, between Cartesian coordinates and wall-oriented coordinates the wall-normal coordinate-space momentum terms are obtained through

$$\rho \hat{u}_{s_i}|_h = M_{ij} \rho \hat{u}_j|_h \quad , \quad \frac{\partial \langle J\rho u_{s_i} \rangle}{\partial t} = M_{ij} \left(\frac{\partial \langle J\rho u_j \rangle}{\partial t} \right)^* \, , \tag{4.33}$$

where $\left(\frac{\partial \langle J\rho u_j \rangle}{\partial t} \right)^*$ is a momentum equation update term specifically computed for the wall-model (not exactly identical to the momentum equation update term computed for the outer-flow LES).

The published literature regarding the evaluation of this wall-model assumes that η_0 is updated using streamwise and spanwise derivatives of the LES information at some point within the LES

domain as shown in Fig. 4.3. In the context of a cell-centered finite-volume discretization, this location is assumed to be the first interior face. In other published works, all the wall-tangential derivatives are evaluated in a plane at this location. The wall-normal derivatives are evaluated between the wall and the first interior face assuming that the wall is a no-slip wall and that the wall-shear-stress can be specified using η_0. This dissertation also uses the no-slip wall condition with η_0 being applied as the wall-shear-stress. However, within this dissertation, the wall-tangential derivatives are evaluated at the wall-normal faces so that the η_0 update follows a standard finite-volume method update for the momentum equation. This provides the ability to nearly match the interior LES momentum equation update computed by the outer-flow LES solver, with the only differences being the wall-shear-stress specification and the wall-normal distance used in the evaluation of wall-normal derivatives. More specifically, this dissertation computes $\left(\frac{\partial \langle J\rho u_j\rangle}{\partial t}\right)^*$ using the following form

$$\left(\frac{\partial \langle J\bar{\rho}\tilde{u}_i\rangle}{\partial t}\right)^* = -\frac{1}{\Delta\xi_k^*}\Bigg\{ \left[\mathrm{N}_{kj}^\top \left(\bar{\rho}\tilde{u}_i\tilde{u}_j + \bar{p}I_{ij} - \widetilde{\mathcal{T}}_{ij} + \tilde{\tau}_{\mathrm{sgs}_{ij}}\right)\right]^{\text{Right Face}} - \left[\mathrm{N}_{kj}^\top \left(\bar{\rho}\tilde{u}_i\tilde{u}_j + \bar{p}I_{ij} - \widetilde{\mathcal{T}}_{ij} + \tilde{\tau}_{\mathrm{sgs}_{ij}}\right)\right]^{\text{Left Face}} \Bigg\} . \tag{4.34}$$

where $\Delta\xi_k^* = \Delta\xi_k$ except for in the case of the wall-normal direction ($k = 1$ for example) where $\Delta\xi_1^* = \Delta\xi_1 + 0.18h_0$. Additionally, $\widetilde{\mathcal{T}}_{ij}$ at the wall is evaluated using the wall-modeled velocity gradient, $\frac{\partial u_i}{\partial x_j}$, at the wall which is given by

$$\frac{\partial u_i}{\partial x_j} = \left(M^\top\right)_{ik} \frac{\partial u_{s_k}}{\partial s_l} M_{lj} = M_{ki}\frac{\partial u_{s_k}}{\partial s_l} M_{lj} \ , \tag{4.35}$$

where $\frac{\partial u_{s_k}}{\partial s_l}$ is constructed assuming that all streamwise and spanwise derivatives of velocity are zero and the wall-normal derivatives of the streamwise and spanwise velocity come from the wall-model

$$\frac{\partial u_{s_k}}{\partial s_l} = \begin{bmatrix} 0 & \left(\eta_0 u_s|_{n=h}\right)/\sqrt{u_s^2+u_p^2} & 0 \\ 0 & \frac{\partial u_n}{\partial s_n} & 0 \\ 0 & \left(\eta_0 u_p|_{n=h}\right)/\sqrt{u_s^2+u_p^2} & 0 \end{bmatrix} , \tag{4.36}$$

where the wall-normal derivative of the wall-normal velocity, $\frac{\partial u_n}{\partial s_n}$, comes from the interior-flow LES algorithm performing a one-sided derivative approximation at the wall.

Once Eq. (4.32) is included along with the other governing equations, η_0 can be marched in time. With η_0 at every wall-face on the mesh, the friction velocity, u_τ can be solved for at each face and an approximation of the local, unresolved velocity profile can be constructed. It is through this SGS velocity profile that the slip-velocity at the wall is computed.

In practice, it is necessary to bound η_0, especially near separation regions, as η_0 will show randomly distributed face values that will rapidly increase without bound. While this is seen with only a single face scattered here and there across the wall boundary, this will cause the simulation to fail if appropriate bounds are not in place. For all the flat-plate results presented in this dissertation, η_0 is bounded to one order-of-magnitude higher than the analytically predicted η_0. In test cases without separation, it was seen that the instantaneous η_0 never fluctuated above three times the analytically predicted mean η_0, thereby justifying the use bound of one order-of-magnitude. For the smooth-ramp case, η_0 is bounded to be no more than twice as high as the η_0 value predicted using the Spalding law profile, Eq. (4.40), with an input velocity from the second cell away from the wall boundary. Additionally, a lower bound (a small numerical tolerance just above zero) was enforced so that η_0 never reached zero. From Eq. (4.32), it is clear that if η_0 does reach zero, it will never leave zero. As a result, η_0 is prevented from reaching zero. As pointed out by Cheng et al. [70], flow-singularities where η_0 is zero are not expected to be encountered in practical simulations of turbulent flow, even near flow separation.

4.4.3 Wall Slip-Velocity Boundary Condition

In order to derive a slip-velocity for the wall boundary, Chung & Pullin extended the interior stretched-vortex model to include near-wall streamwise-oriented vortices. From this model, a law-of-the-wall-like velocity profile was derived for the wall-adjacent cells. Cheng et al. [70] extended this model to include a linear velocity profile for regions of separated flow. Separated flow regions are defined to be regions where the local wall-shear-stress, τ_w is less than or equal to zero. The

local wall-shear-stress vector is assumed to align with the velocity at the first interior face, and as a result, separation locations are those regions where the velocity at the first interior face points opposite a problem-defined freestream velocity direction. This form of the model [70] is given as

$$\|u\|_{n=h_0} = \begin{cases} \begin{cases} u_\tau \left(\frac{1}{\mathscr{K}_1} \ln\left(\frac{h_0^+}{h_\nu^+} \right) + h_\nu^+ \right), & h_0^+ > h_\nu^+ \\ u_\tau h_0^+, & h_0^+ \leq h_\nu^+ \end{cases} & \tau_w > 0 \\ u_\tau h_0^+, & \tau_w \leq 0 \end{cases} \tag{4.37}$$

where $\|u\|_{n=h_0}$ is the slip-velocity magnitude at the slip-wall, $h_\nu^+ = h_\nu u_\tau / \nu$ is the inner-scaled height of the viscous sublayer, $h_0^+ = h_0 u_\tau / \nu$ is the inner-scaled height of the virtual wall, and $\mathscr{K}_1$ is a von-Karman-like parameter. In the current dissertation, $\mathscr{K}_1$ is fixed to 0.4 for all of the results presented. Additionally, all results presented here follow literature in approximating h_ν^+ as 11. In defining the freestream velocity direction, the implementation in this dissertation allows for a user-defined global streamwise vector. For all of the tests presented, this direction corresponds to the Cartesian coordinate direction x.

Once the magnitude of the slip-velocity is obtained, this dissertation follows published literature in that the slip-velocity is projected onto the wall-local wall-tangential velocity vector to obtain the slip-velocity vector. Finally, a wall-normal velocity is also specified at the wall. Cheng et al. derived a wall-normal velocity condition based on the mass conservation equation [70] and this dissertation uses this same wall-normal velocity derivation. Since the physical wall is a no-slip wall, mass conservation relates the wall-normal velocity at the virtually-raised slip-wall with the streamwise derivative of η_0 as follows

$$u_n = -\frac{h \|u\|_{n=h_0}}{2\eta_0} \frac{\partial \eta_0}{\partial s} \, . \tag{4.38}$$

Cheng et al. applied a spanwise filter to η_0 prior to computing the derivative in order to avoid spurious overshoots of wall-normal velocity near separation points. The current dissertation also

applies as small filtering operation to η_0 prior to computing the derivative, but it is a simple top-hat or box filter applied over a region with a radius of one neighbor cell-face (i.e. the face of interest and the 9 neighbor points). Additionally, the magnitude of u_n is limited to $\leq 0.1\|u\|_{n=h_0}$. This was found to be sufficiently robust even in regions of flow separation.

4.4.4 Initialization of η_0 Variable

In order to shorten the initial transient phase during the simulation startup, it is best to provide an accurate estimate for η_0 based on the near-wall velocity initial condition. If this is not done, Eq. (4.32) is such that η_0 tends toward the correct value as long as a physically meaningful initial condition for η_0 is provided. By construction from Eq. (4.23), $\eta_0 \geq 0$, and the initial condition can be specified such that $\eta_0 > 0$ in order for η_0 to continue to update to non-zero values. However, it is desirable to reduce the time to reach the correct value, and so a quality initial guess for η_0 is generally computed based on a local law-of-the-wall profile. Useful profiles include the profile developed by Musker [64]

$$\begin{aligned} u^+ = 5.424\tan^{-1}\left[\frac{2y^+ - 8.15}{16.7}\right] + \log_{10}\left[\frac{\left(y^+ + 10.6\right)^{9.6}}{\left(y^{+^2} - 8.15y^+ + 86\right)^2}\right] - 3.52 \\ + 2.44\left\{\Pi\left[6\left(\frac{y}{\delta_{100}}\right)^2 - 4\left(\frac{y}{\delta_{100}}\right)^3\right] + \left[\left(\frac{y}{\delta_{100}}\right)^2\left(1 - \frac{y}{\delta_{100}}\right)\right]\right\}, \end{aligned} \tag{4.39}$$

and the profile developed by Spalding [71]

$$y^+ = u^+ + 0.1108\left[e^{0.4u^+} - 1 - 0.4u^+ - \frac{\left(0.4u^+\right)^2}{2!} - \frac{\left(0.4u^+\right)^3}{3!} - \frac{\left(0.4u^+\right)^4}{4!}\right], \tag{4.40}$$

where $u^+ = u/u_\tau$, $y^+ = yu_\tau/\nu$, δ_{100} is the 100% boundary-layer thickness, and Π is Coles' wake parameter. Both of these equations can be solved for u_τ and then for η_0 if sufficient information is known. For the Musker profile, δ_{100} is required while for the Spalding profile, it is not. Even so, the Musker profile provides high accuracy for determining the wall friction velocity. For all results

presented in this dissertation, the Musker profile in Eq. (4.39) is utilized to initialize η_0 since the initial velocity profiles and the initial target boundary-layer thicknesses are specified.

Chapter 5

Numerical Framework

This chapter provides details regarding the numerical framework which is utilized for simulations within this dissertation. An overview of the finite volume algorithm is presented along with a discussion of two methods of numerical stabilization/regularization (upwinding and limiting). Following this, the numerical implementation of the stretched-vortex model and associated developments unique to this dissertation are described. The chapter concludes with a presentation of the numerical implementation of boundary conditions.

5.1 Finite Volume Algorithm: Chord

All results presented in this study are obtained using the finite volume method (FVM) algorithm, Chord [72–76], built upon the highly parallelizable (scaling to at least 1×10^5 cores) AMR framework Chombo [77]. Chord solves the governing equations for transient, compressible, turbulent, reacting and non-reacting fluid flows with complex geometry. It has been designed to achieve high levels of accuracy and performance for turbulence and combustion simulations on modern high-performance computing architectures. For smooth flows, Chord is fourth-order accurate in space and time (using standard four-stage Runge Kutta time-marching) [72–76]. For flows with strong discontinuities (e.g. shocks or detonation waves), the PPM [78, 79] limiter is used for stability. Chord is capable of additional stabilization by hyperviscosity through fifth-order face-value interpolations. Chord's turbulence modeling capabilities include unsteady Reynolds-averaged Navier-Stokes (URANS), LES, and DNS. Additionally, Chord utilizes AMR in space and subcycling in time and accommodates complex geometry while preserving free-stream conditions using generalized coordinate transformations.

In the present study, all spatially discrete operators are fourth-order accurate by default. However, numerical stabilization in the form of either the PPM limiter or hyperviscosity is tested in conjunction with the SV LES model.

5.2 Fifth-Order Interpolation/Hyperviscosity

In FVMs, flux evaluations at the faces of a computational cell are essential and require knowledge of face values. Reconstructing solution variables at cell faces is one of the fundamental operations in the algorithm and is a major difficulty in terms of stability. Low-dissipation, high-order, centered interpolations can create spurious, high-frequency solution content and allow it to grow, especially near unresolved solution gradients. Adding a high-order viscosity term to the interpolation through a spatially-biased interpolant can help alleviate spurious high-frequency content [80].

Interpolating the face-averaged primitive state, $\langle \mathbf{W} \rangle_{\boldsymbol{i}+\frac{1}{2}\boldsymbol{e}^d}$, from the cell-averaged primitive state, $\langle \mathbf{W} \rangle_{\boldsymbol{i}}$, follows the process described in previous literature [72, 73]. A cell index is denoted by $\boldsymbol{i}$ on an integer lattice and $\boldsymbol{e}^d$ is a unit-vector in direction d. A cell face is reached by a shift of $1/2$. A four-cell, fourth-order, centered approximation to $\langle \mathbf{W} \rangle_{\boldsymbol{i}+\frac{1}{2}\boldsymbol{e}^d}$ is given by

$$\langle \mathbf{W} \rangle^{(4)}_{\boldsymbol{i}+\frac{1}{2}\boldsymbol{e}^d} = \frac{7}{12}\left(\langle \mathbf{W} \rangle_{\boldsymbol{i}} + \langle \mathbf{W} \rangle_{\boldsymbol{i}+\boldsymbol{e}^d}\right) - \frac{1}{12}\left(\langle \mathbf{W} \rangle_{\boldsymbol{i}-\boldsymbol{e}^d} + \langle \mathbf{W} \rangle_{\boldsymbol{i}+2\boldsymbol{e}^d}\right) \ , \tag{5.1}$$

while the right-biased, five-cell, fifth-order approximation is provided by

$$\begin{aligned} \langle \mathbf{W} \rangle^{(5)}_{\boldsymbol{i}+\frac{1}{2}\boldsymbol{e}^d,R} = &\frac{1}{60}\left(-3\langle \mathbf{W} \rangle_{\boldsymbol{i}-\boldsymbol{e}^d} + 27\langle \mathbf{W} \rangle_{\boldsymbol{i}} + 47\langle \mathbf{W} \rangle_{\boldsymbol{i}+\boldsymbol{e}^d} - 13\langle \mathbf{W} \rangle_{\boldsymbol{i}+2\boldsymbol{e}^d}\right) \\ &+ \frac{1}{60}\left(2\langle \mathbf{W} \rangle_{\boldsymbol{i}+3\boldsymbol{e}^d}\right) \ . \end{aligned} \tag{5.2}$$

A reflection of Eq. (5.2) about the face provides a left-biased interpolation. Using both the left and right-biased values, the final face value is the solution of a Riemann problem.

Examining the difference between the two interpolations reveals the high-order, cell-centered numerical dissipation term present in the fifth-order interpolant

$$\begin{aligned}\langle \mathbf{W} \rangle^{(5)}_{\boldsymbol{i}+\frac{1}{2}\boldsymbol{e}^d,R} - \langle \mathbf{W} \rangle^{(4)}_{\boldsymbol{i}+\frac{1}{2}\boldsymbol{e}^d} = \\ \frac{1}{30}\left(\langle \mathbf{W} \rangle_{\boldsymbol{i}-\boldsymbol{e}^d} - 4\langle \mathbf{W} \rangle_{\boldsymbol{i}} + 6\langle \mathbf{W} \rangle_{\boldsymbol{i}+\boldsymbol{e}^d} - 4\langle \mathbf{W} \rangle_{\boldsymbol{i}+2\boldsymbol{e}^d} + \langle \mathbf{W} \rangle_{\boldsymbol{i}+3\boldsymbol{e}^d}\right) \\ \approx \frac{\Delta x^4}{30}\frac{\partial^4}{\partial x^4}\left(\langle \mathbf{W} \rangle_{\boldsymbol{i}+\boldsymbol{e}^d}\right) \ .\end{aligned} \tag{5.3}$$

It is through the high-order numerical dissipation term that the highest frequency content is detected and controlled.

5.3 Piecewise Parabolic Method

The high-order piecewise parabolic method (PPM) is a high-order extension of Godunov's method [78, 79, 81]. Essentially, the PPM consists of two main steps. First, face values are interpolated using high-order finite difference approximations based on the cell-averaged values. If necessary, the interpolants are limited to ensure monotonicity. Second, a parabolic profile is constructed in each cell, using cell and face values, and constrained to keep it monotone. If the local extremum is smooth, as determined by checking adjacent second derivatives, the limiter is not applied. A third-derivative condition is also checked to avoid limiting perturbations of a cubic in multidimensional problems [79]. The PPM scheme delivers a more accurate representation of spatial gradients of smooth flows and a steeper representation of discontinuities. Additional techniques such as artificial dissipation and slope flattening are applied at shocks to suppress unwanted numerical oscillations. In the limit of a complete flattening, the scheme recovers the first-order Godunov method locally near the discontinuities. In the present study, the PPM scheme is implemented closely following the work by McCorquodale and Colella [79].

5.4 Numerical Implementation of the SV SGS Model

When applying the SV SGS model at a coarser filter-length-scale, Δ_f, than the grid filter, Δx, existing AMR infrastructure is used within Chord. Throughout this section, a subscript f associated with Δ refers to the filter length-scale, while a superscript f associated with other variables refers to a fine mesh. Additionally, a superscript c refers to a coarse mesh. More specifically, the fine mesh is the reference mesh of interest and the coarse mesh is a coarsened version of the mesh of interest. As shown in Fig. 5.1, the cell-averaged primitive state on the original fine mesh at cell-index $\boldsymbol{i}$, $\langle \mathbf{W} \rangle_{\boldsymbol{i}}^f$, is averaged to a coarser mesh, $\langle \mathbf{W} \rangle_{\boldsymbol{i}}^c$. The fine mesh has cell spacing Δx. Following the averaging procedure, the coarse cell-averaged value, $\langle \mathbf{W} \rangle_{\boldsymbol{i}}^c$, is deconvolved to obtain

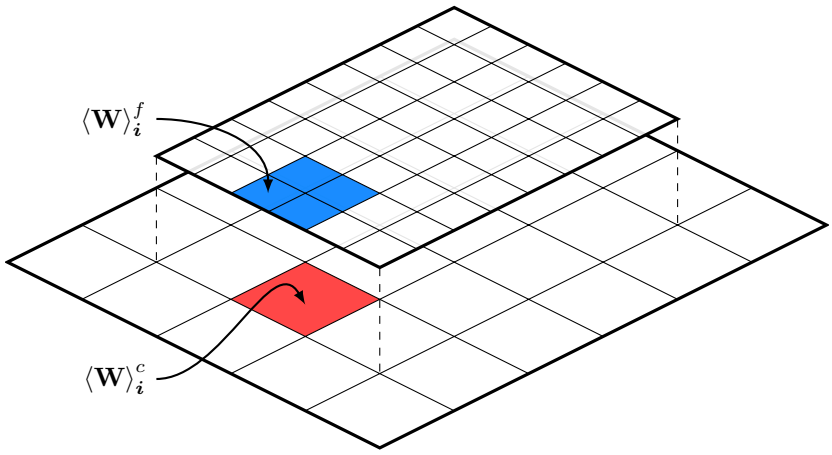

Figure 5.1: Coarsened SGS kinetic energy estimate (example demonstrates $\Delta_f = 2\Delta x$).

the cell-centered value, $\mathbf{W}_{\boldsymbol{i}}^c$, to fourth-order accuracy using the deconvolution [79]

$$\mathbf{W}_{\boldsymbol{i}}^c = \langle \mathbf{W} \rangle_{\boldsymbol{i}}^c - \sum_d \frac{h_d^2}{24} \frac{\partial^2 \langle \mathbf{W} \rangle_{\boldsymbol{i}}^c}{\partial x_d^2} \,, \tag{5.4}$$

where h is the cell spacing of the grid level. Working with the cell-centered state as opposed to the cell-averaged state preserves the order-of-accuracy of the numerical scheme and the SGS energy estimate in smoothly varying solution fields even when computing nonlinear terms. To use the cell-averaged quantities during the computation of nonlinear terms would not preserve the scheme's

order-of-accuracy in nonlinearly-evolving smooth regions of the flow unless rather complicated product-rules of averages were utilized. On the coarser mesh, with cell spacing Δ_f, the SGS kinetic energy estimate is computed using $\mathbf{W}_{\boldsymbol{i}}^c$ and then interpolated to the original mesh. From here, $\langle K_{\text{SGS}} \rangle_{\boldsymbol{i}}^f$ is interpolated to the cell faces where it becomes a face-averaged value, $\langle K_{\text{SGS}} \rangle_{\boldsymbol{i}+\frac{1}{2}\boldsymbol{e}^d}^f$. On the cell faces, the orientation model is computed using $\mathbf{W}_{\boldsymbol{i}}^f$ and combined with K_{SGS}^f to obtain a conservative SGS momentum flux. The detailed steps as presented in an algorithm format are as follows:

1. Average the fine cell-averaged primitive state to a coarser mesh and deconvolve it to obtain the coarse cell-centered primitive state:

$$\langle \mathbf{W} \rangle_{\boldsymbol{i}}^f \rightarrow \langle \mathbf{W} \rangle_{\boldsymbol{i}}^c \rightarrow \mathbf{W}_{\boldsymbol{i}}^c$$

2. Compute the coarsened cell-centered SGS kinetic energy estimate from the cell-centered primitive state, using Eqs. (4.9–4.14) and average it over a coarse cell:

$$\mathbf{W}_{\boldsymbol{i}}^c \rightarrow (K_{\text{SGS}})_{\boldsymbol{i}}^c \rightarrow \langle K_{\text{SGS}} \rangle_{\boldsymbol{i}}^c$$

3. Interpolate the cell-averaged SGS kinetic energy estimate to the fine mesh:

$$\langle K_{\text{SGS}} \rangle_{\boldsymbol{i}}^c \rightarrow \langle K_{\text{SGS}} \rangle_{\boldsymbol{i}}^f$$

4. Interpolate the fine cell-averaged SGS kinetic energy to the cell faces, using Eq. (5.1), and deconvolve it to obtain the fine face-centered SGS kinetic energy estimate:

$$\langle K_{\text{SGS}} \rangle_{\boldsymbol{i}}^f \rightarrow \langle K_{\text{SGS}} \rangle_{\boldsymbol{i}+\frac{1}{2}\boldsymbol{e}^d}^f \rightarrow (K_{\text{SGS}})_{\boldsymbol{i}+\frac{1}{2}\boldsymbol{e}^d}^f$$

5. Compute the fine face-centered turbulent flux using the interpolated SGS kinetic energy estimate and the orientation model computed on the fine mesh with fine mesh data.

As complex as this appears, even without optimizing the computational implementation, for simulations without mapping, the SGS model costs less than 10% of the computation time when the coarsening ratio is 4 ($\Delta_f = 4\Delta x$), and approximately 35% of the computation time when $\Delta_f = \Delta x$ for a three-dimensional simulation.

Using $\Delta_f > \Delta x$ for the SV model has previously been tested, as in the study of Chung and Matheou [82]. Furthermore, it was conclusively demonstrated that grid-converged LES results are obtainable for high-Reynolds number, practical flow simulations. The current study departs from the implementation methodology of Chung and Matheou in that the current study explicitly uses a coarser mesh when computing the SV model SGS kinetic energy estimate rather than implicitly incorporating the larger filter width through the κ_c parameter in Eqs. (4.9–4.11). This difference is utilized in order to enable the coupling of the SV model with numerical regularization. Without computing the SGS kinetic energy estimate on a coarser mesh, the smallest represented information necessary for the SV model SGS kinetic energy calculation would still largely be affected by the numerical regularization. As a result, the model would still register too low of an SGS kinetic energy estimate, even with the increased filter-width size being incorporated into the computations through κ_c. The SV model was originally designed to match an explicitly defined SGS kinetic energy spectra to the smallest representable-scale kinetic energy. Using numerical regularization, it is expected that the scales used to match the SGS kinetic energy spectra should no longer reside near the grid-cutoff, but rather at the scales associated with the equivalent filter size of the LES system.

5.5 Characteristic Boundary Conditions

Correctly and adequately specifying boundary conditions is a critical step in obtaining an accurate numerical solution. Traditionally, boundary conditions for compressible, turbulent flows have largely fallen into several categories, including nonlinear characteristic boundary conditions (CBCs) and absorbing layers (e.g. stretched grids, perfectly-matched layers, etc.) [83]. Absorbing layers either sacrifice some of the usable computational domain through providing extra dissipation near the boundaries or require additional "fake" domain regions outside of the target domain. However, nonlinear CBCs require no such modification of the domain size and are designed to work directly at the domain boundaries without negatively dissipating the near-boundary flow.

To begin the derivation of the nonlinear CBCs, the PDEs of interest are transformed into the characteristic form in order to take advantage of any wave-like structure in the equations. Considering a one-dimensional example of a system of first-order PDEs in conservation form

$$\frac{\partial \mathbf{U}}{\partial t} + \frac{\partial \mathbf{F}}{\partial x} = 0 \,, \tag{5.5}$$

where $\mathbf{U}$ is the conservative variable state-vector and $\mathbf{F}$ is the flux, it is possible to transform the equations into the primitive form

$$\frac{\partial \mathbf{W}}{\partial t} + \mathbf{A}\frac{\partial \mathbf{W}}{\partial x} = 0 \,, \tag{5.6}$$

where $\mathbf{W}$ is the primitive variable state and $\mathbf{A}$ is the coefficient matrix of the primitive equations. Assuming $\mathbf{A}$ is diagonalizable, it can be decomposed into left eigenvectors, $\mathbf{S}^{-1}$, right eigenvectors, $\mathbf{S}$, and eigenvalues, $\mathbf{\Lambda}$, so that Eq. (5.6) becomes

$$\frac{\partial \mathbf{W}}{\partial t} + \mathbf{S}\mathbf{\Lambda}\mathbf{S}^{-1}\frac{\partial \mathbf{W}}{\partial x} = 0 \,. \tag{5.7}$$

Left multiplying Eq. (5.7) by $\mathbf{S}^{-1}$ brings the equations into the characteristic form

$$\frac{\partial \mathbf{V}}{\partial t} + \mathbf{\Lambda}\frac{\partial \mathbf{V}}{\partial x} = 0 \,, \tag{5.8}$$

where the temporal and spatial derivatives of the characteristic variables, $\mathbf{V}$, are defined as

$$\frac{\partial \mathbf{V}}{\partial t} = \mathbf{S}^{-1}\frac{\partial \mathbf{W}}{\partial t} \quad , \quad \frac{\partial \mathbf{V}}{\partial x} = \mathbf{S}^{-1}\frac{\partial \mathbf{W}}{\partial x} \,. \tag{5.9}$$

The characteristic form, Eq. (5.8), presents the original set of PDEs as a set of decoupled equations cast in a form similar to the first-order linear advection equation. Each equation has a particular wave speed, defined by the eigenvalue in the diagonal matrix $\mathbf{\Lambda}$, which determines how fast the associated solution information propagates through the solution domain. Due to the wave-like nature of Eq. (5.8), if the characteristic state is known at one location, the solution is known

along the rest of the characteristic line until nonlinear interactions with another characteristic line changes the solution state. It is this particular feature of the characteristic form of the equations that CBCs take advantage of. If the full wave state is known at the boundaries of a problem domain, then the problem is well-posed. Since outgoing waves only come from the domain interior, only wave information entering the domain needs to be specified to complete the boundary condition. Conveniently, the wave speeds naturally define which waves are entering or exiting the problem domain. The main challenge of CBCs then becomes estimating the amplitudes of the waves and obtaining a BC in terms of $\mathbf{W}$ or $\mathbf{U}$ from the wave amplitudes.

Throughout the CBC literature, $\mathbf{\Lambda}\frac{\partial \mathbf{V}}{\partial x}$ (or, equivalently, $\mathbf{\Lambda}\mathbf{S}^{-1}\frac{\partial \mathbf{W}}{\partial x}$) is typically referred to as the characteristic wave amplitude vector, $\mathcal{L}$ [84, 85]. In the case of finite difference methods (FDM) where a solution node lies on the domain boundary, it is natural to define an external node (a ghost node) and specify a desired flow state at the ghost node as shown in Fig. 5.2. The interior wave

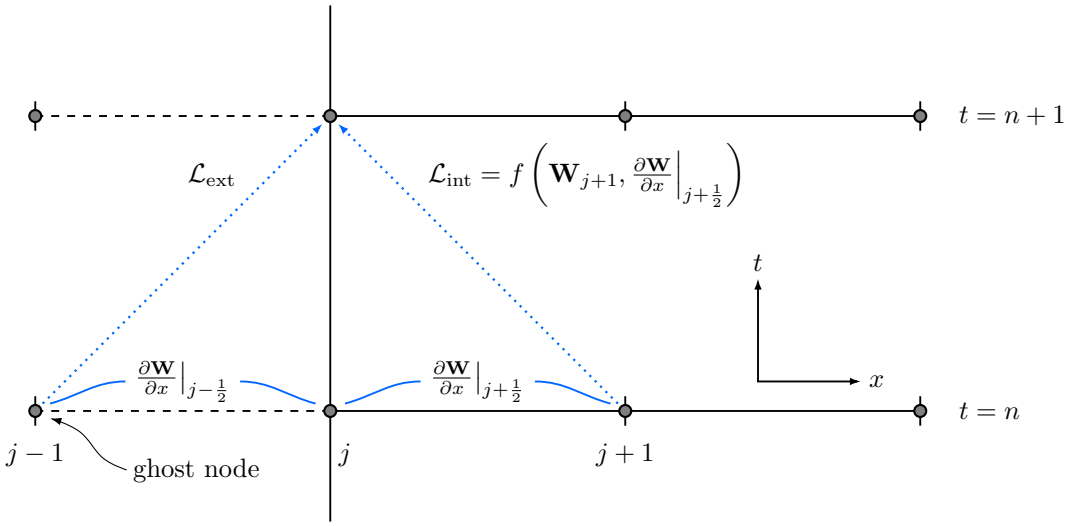

Figure 5.2: Space-time diagram of boundary-node update using characteristic boundary conditions in a finite difference method. For simplicity, the diagram shows left and right moving waves with equal speed, $\lambda_L = \lambda_R$, and a discretization with $\lambda \Delta t / \Delta x = 1$.

amplitudes, $\mathcal{L}_{\text{int}}$, and the exterior wave amplitudes, $\mathcal{L}_{\text{ext}}$, are then easily computed from spatial derivatives of the primitive state $\mathbf{W}$ and the left eigenvectors, $\mathbf{S}^{-1}$, evaluated at a reference state.

Once the wave amplitudes are known, the FDM form of the CBCs updates the boundary node primitive state in time using Eq. (5.7).

In contrast to FDMs, the Godunov-type cell-centered FVMs (finite volume methods) described herein use the cell-averaged solution state to construct an estimate for the face-averaged solution state or the face-averaged flux on the faces between mesh volumes. The face-averaged flux is then used to update the cell-averaged state in time. An extension of the CBC method specific to Godunov-type FVMs using ghost cells has been developed [86]. However, this particular extension is largely unsuitable for the specific type of FVM being used within this dissertation and tests showed undesirable acoustic reflections associated with turbulent outflows.

It is obvious from Fig. 5.3 that the space-time geometry of cell-centered FVMs is different enough from FDMs that the typical CBC method used for FDMs does not fit cleanly into the FVM framework. Just as in the FDM, the cell-centered FVM requires a domain-exterior ghost cell state

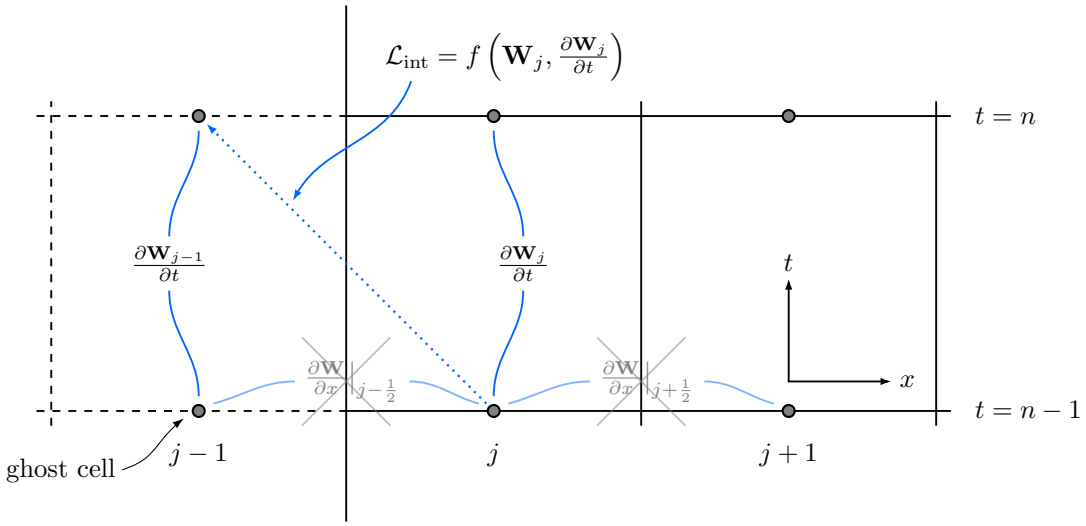

Figure 5.3: Space-time diagram of specifying ghost-cell values using characteristic boundary conditions in a finite volume method.

in order to use the same method of estimating the face-averaged flux for both the interior and boundary faces. However, unlike the FDM CBC, computing $\mathcal{L}_{\text{int}}$ in the FVM CBC by using spatial derivatives would be computing the wave amplitude at the first interior face (which is analogous to

what a Godunov-type FVM already does at faces). Assuming this $\mathcal{L}$ applies to the boundary face would be shifting the characteristic wave away from its correct location. Additionally, attempting to alleviate this problem by computing $\mathcal{L}$ at the boundary face through the use of spatial derivatives would require the CBC-modified ghost cell value to already be known.

The solution developed in the current dissertation relies on reformulating the calculation of $\mathcal{L}$. From Eq. (5.8), it is apparent that

$$\mathcal{L} \equiv \mathbf{\Lambda}\frac{\partial \mathbf{V}}{\partial x} = -\frac{\partial \mathbf{V}}{\partial t} = -\mathbf{S}^{-1}\frac{\partial \mathbf{W}}{\partial t} \ , \tag{5.10}$$

and, as a result, it is apparent that the wave amplitudes are computable by merely swapping temporal derivatives for spatial derivatives and normalizing by the wave speeds, $\mathbf{\Lambda}$. This formulation provides a means of obtaining the wave amplitudes in the first interior cell instead of the wave amplitudes at the first interior face. A simple backward difference in time provides the temporal derivative of $\mathbf{W}$ at the current time step (time step n) using only one previous time-level of information (time step $n-1$)

$$\frac{\partial \mathbf{W}}{\partial t} = \frac{\mathbf{W}^n - \mathbf{W}^{n-1}}{\Delta t} \ . \tag{5.11}$$

While this does increase solution-state storage requirements slightly, in this dissertation, previous time data is only stored from the boundary-adjacent cells (both interior boundary-adjacent cells and ghost cells). To finish the computation of $\mathcal{L}$, a reference state is required for $\mathbf{S}^{-1}$. Since the reference state propagates along the characteristic wave to the neighbor location and since the information propagates forward in time, the previous time state is the natural reference state to choose. As a result, the computation of $\mathcal{L}$ is formulated as

$$\mathcal{L}_j = \left(\mathbf{S}^{-1}\right)_j^{n-1} \left(\frac{\mathbf{W}_j^n - \mathbf{W}_j^{n-1}}{\Delta t} \right) \ . \tag{5.12}$$

It is important to note that the exterior wave amplitudes are computed using the target states at both the previous time (time step $n-1$) and the current time (time step n). In essence, after the entire

CBC calculation is performed and the CBC values have been used to compute the boundary fluxes, the updated exterior ghost cell state is reset back to the target state in preparation for the next time step. This effectively reduces the deviation of the exterior state from the intended target value.

Once $\mathcal{L}_{\text{int}}$ and $\mathcal{L}_{\text{ext}}$ are computed, the ghost cell primitive state is updated using the desired mix of the interior and exterior wave amplitudes and reference states. More specifically, the boundary condition can be set to a non-reflecting CBC, a fully reflecting CBC, or somewhere in between. In the non-reflecting limit, all outgoing waves should exit the domain with no spurious reflections from the domain boundary and all incoming waves should enter the domain while generating no spurious, additional wave information. For cases requiring turbulence to enter or exit the domain without excessive distortion of the interior flow, non-reflecting boundary conditions are ideal. The non-reflecting wave amplitude vector, $\mathcal{L}_{\text{non-reflecting}}$, is a mix of the interior and exterior wave amplitudes

$$\mathcal{L}_{\text{non-reflecting}} = \mathcal{H}\left(-\mathbf{\Lambda}\right)\mathcal{L}_{j-1} + \mathcal{H}\left(\mathbf{\Lambda}\right)\mathcal{L}_{j} \ , \tag{5.13}$$

where $\mathcal{H}\left(\phi\right)$ is the Heaviside step function. To smoothly blend between non-reflecting and reflecting CBCs, a tunable parameter, $\beta \in [0, 1]$, is introduced into the calculation of the wave amplitude state used to update the ghost cell state

$$\mathcal{L}_{\text{update}} = \beta\mathcal{L}_{\text{non-reflecting}} + \left(1-\beta\right)\mathcal{L}_{j-1} \ . \tag{5.14}$$

Additionally, the reference state used to update the ghost cell, $\mathbf{W}_{\text{ref}}^{n-1}$, is modified to incorporate β

$$\mathbf{W}_{\text{ref}}^{n-1} = \beta\mathbf{W}_{\text{non-reflecting}}^{n-1} + \left(1-\beta\right)\mathbf{W}_{j-1}^{n-1} \ , \tag{5.15}$$

where $\mathbf{W}_{\text{non-reflecting}}^{n-1}$ is equal to the exterior state at the previous time, $\mathbf{W}_{j-1}^{n-1}$, unless the boundary condition is an outflow, in which case $\mathbf{W}_{\text{non-reflecting}}^{n-1} = \mathbf{W}_{j}^{n-1}$. For the results presented in this dissertation, $\beta = 1$ is used for results using non-reflecting boundary conditions, while $\beta = 0$ is used for results with reflecting boundary conditions. The right eigenvector, $\mathbf{S}_{\text{ref}}$, is computed

from $\mathbf{W}_{\text{ref}}^{n-1}$. The ghost cell primitive state is updated using a forward difference in time from the reference state with the computed wave amplitudes

$$\mathbf{W}_{j-1}^{n} = \mathbf{W}_{\text{ref}}^{n-1} - \Delta t \mathbf{S}_{\text{ref}} \mathcal{L}_{\text{update}} \ . \tag{5.16}$$

Following the computation of the ghost cell value, a Riemann solution between the exterior and interior states, $\mathbf{W}_{j-1}^{n}$ and $\mathbf{W}_{j}^{n}$, provides the resolved face state, $\mathbf{W}_{j+\frac{1}{2}}^{n}$, used to compute the boundary fluxes.

Essentially, this boundary condition is interpreted as a relaxation of the exterior target state (the state specified in the ghost cell). This relaxation is accomplished by first computing the wave amplitudes defined by the time-variation of the exterior and interior states and then replacing some of the exterior wave amplitudes with the corresponding interior wave amplitudes as necessary.

Chapter 6

Test Cases

Throughout this study, several cases test the concepts and algorithms; the first three are unbounded (i.e. fully periodic), while the last two feature walls. The first is a temporally-evolving mixing-layer [55, 87, 88], while the second case is the decaying, inviscid Taylor-Green vortex where the Reynolds number is infinity [89]. The third case is a decaying, homogeneous turbulence case based on the widely used Comte-Bellot and Corrsin experimental dataset of decaying, grid-generated turbulence [90]. The fourth case presented is a zero-pressure-gradient flat-plate turbulent boundary-layer [68], while the last case is flow-separation over a smooth-ramp [91].

6.1 Time-Evolving Mixing-Layer

The time-evolving mixing-layer considered in the present study is configured as fully-periodic double-shear as shown in Fig. 6.1. The freestream velocities of streams 1 and 2 are $U_{1,\infty} =$

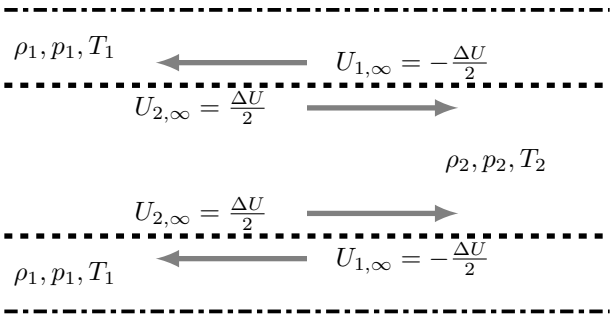

Figure 6.1: Configuration of the time-evolving double mixing-layer.

$34.03\,\mathrm{m/s}$ and $U_{2,\infty} = -U_{1,\infty}$, respectively, and the freestream pressures and densities of both streams are identical. The flow has a Mach number, M, of 0.1 based on the arithmetic mean of $|U_{1,\infty}|$ and $|U_{2,\infty}|$ (equivalent to $|U_{1,\infty}|$ for this case), a Prandtl number, Pr = 0.71, a specific heat

ratio, $\gamma = 1.4$, and a Reynolds number of 11650, based on

$$Re_{\delta_\omega,0} = \frac{\rho\,|U_\infty|\,\delta_\omega}{\mu}\,, \tag{6.1}$$

where δ_ω is the initial vorticity thickness

$$\delta_\omega = \frac{1}{\rho_0}\int_{-L_y/2}^{L_y/2} \bar{\rho}\left(1 - \frac{\tilde{u}^2}{(\Delta u/\,2)^2}\right)\mathrm{d}y\,, \tag{6.2}$$

with L_y being the domain length in the shear-layer normal direction, and Δu being the magnitude of the difference between the two freestream velocities, $\Delta u = |U_{2,\infty} - U_{1,\infty}|$. The momentum thickness, δ_θ, is $\delta_\omega/4$. The computational domain size is, $L_x \times L_y \times L_z$ = $137\delta_\theta \times 137\delta_\theta \times 68\delta_\theta$. The meshes consist of coarse resolutions with $64 \times 64 \times 32$ cells in the streamwise, shear-layer normal, and spanwise directions respectively, medium resolutions with $128 \times 128 \times 64$ cells, and fine resolutions with $256 \times 256 \times 128$ cells.

The velocities in each stream were sinusoidally perturbed and computed from a stream function in order to achieve an analytically divergence-free initial velocity field. This stream function is defined as

$$\Psi = \xi U_{1,\infty}\mathrm{tanh}\left(\frac{\xi}{2\delta_\theta}\right)\,, \tag{6.3}$$

where the factor ξ is defined as

$$\xi = y + \exp\left(-\eta|y|\right)\left(\sum_i b_i \mathrm{sin}\left(\frac{2\pi\omega_i x}{L} + \phi_i\right)\right)\,, \tag{6.4}$$

and the velocities are computed analytically as

$$u = \frac{\partial\Psi}{\partial y} \quad , \quad v = -\frac{\partial\Psi}{\partial x}\,. \tag{6.5}$$

The i-th perturbation mode has phase shift ϕ_i, wavenumber ω_i, and magnitude b_i. The parameter η controls the decay rate of the perturbations in the shear-layer normal direction. For this study,

$\eta = 8\pi/L_y$. Perturbation modes with $\omega = 8$, 4, 2, and 1 were chosen for the streamwise and spanwise directions. The dominant mode with $\omega = 8$ was given $b = 0.1\,(L_y/2)$ for the streamwise direction and $b = 0.05\,(L_y/2)$ for the spanwise direction. All other perturbations were randomly provided magnitudes of either three percent or one percent of the half-domain height. Streamwise and spanwise phase shifts were randomly chosen. Density was initialized from the ideal gas law assuming constant pressure, identical free-stream density values for both shear-layer streams, and using the Crocco-Busemann relation for temperature

$$\rho = \rho_0 \left[1 + \frac{1}{2}\left(\gamma - 1\right) M^2 \left(1 - \tanh\left(\frac{\xi}{2\delta_\theta}\right)\right)\left(1 + \tanh\left(\frac{\xi}{2\delta_\theta}\right)\right)\right] \ . \tag{6.6}$$

Pressure was initialized assuming a constant pressure profile with correction for the velocity perturbations

$$p = p_0 - \frac{1}{2}\rho_0 \left(\hat{u}^2 + 2\hat{u}U_0 \tanh\left(\frac{\xi}{2\delta_\theta}\right) + v^2\right)\left(\gamma - 1\right) \ , \tag{6.7}$$

where $\hat{u}$ is given by

$$\hat{u} = u - U_0 \tanh\left(\frac{\xi}{2\delta_\theta}\right) \ . \tag{6.8}$$

The double-shear problem provides an anisotropic-turbulence test case in which the turbulence is fed by a freestream, large-scale energy reservoir. This energy reservoir continually generates turbulence until the turbulence reaches the periodic boundaries, essentially mimicking a forced turbulence problem. At this point, the energy decays away. Although a relatively simple configuration, the double-shear case provides a test with flow features commonly encountered in real-world engineering problems. The large-scale anisotropy is common in almost any wall-bounded or jet-type flow as is the continual production of turbulent energy from large-scale flow features that persist for long time-periods. For these reasons, the time-evolving shear-layer has been a favorite for testing LES models and algorithms. The SV model has previously been tested with the time-evolving shear-layer by Mattner [55]. While Mattner used a Fourier spectral collocation scheme in the periodic streamwise and spanwise directions and an eighth-order finite-difference scheme

in the slip-wall-bounded shear-layer normal direction, every coordinate direction in the present study uses the finite-volume discretization described in Chapter 5. Additionally, Mattner presented one-dimensional energy spectra while the current study presents three-dimensional energy spectra.

6.2 Inviscid Taylor-Green Vortex

The Taylor-Green vortex flow is initialized in a fully-periodic cube of side-length D with a sinusoidal initial condition given by

$$u = -U_0 \sin\left(\frac{n\pi x}{D}\right) \cos\left(\frac{n\pi y}{D}\right) \sin\left(\frac{n\pi z}{D}\right) \tag{6.9}$$

$$v = U_0 \cos\left(\frac{n\pi x}{D}\right) \sin\left(\frac{n\pi y}{D}\right) \sin\left(\frac{n\pi z}{D}\right) \tag{6.10}$$

$$w = 0 \tag{6.11}$$

$$p = p_0 + \frac{\rho_0 U_0^2}{16}\left(\cos\left(\frac{2n\pi x}{D}\right) + \cos\left(\frac{2n\pi y}{D}\right)\right)\left(\cos\left(\frac{2n\pi z}{D}\right) + 2\right) \tag{6.12}$$

$$\rho = \frac{p}{RT_0} = \frac{p\rho_0}{p_0} \tag{6.13}$$

where U_0 is the velocity fluctuation magnitude and n is the number of vortices contained in the domain in each coordinate direction. The flow has a Mach number based on U_0 of 0.1, a Prandtl number of 0.71, and a specific heat ratio $\gamma = 1.4$. Cell counts of 64^3, 128^3, and 256^3 were used for all of the Taylor-Green vortex cases.

In the limit of infinite Reynolds number, the Taylor-Green vortex provides an ideal test of algorithmic components examined in this study. The vortex evolution begins with "vortex wrap-up", eventually transitioning to a turbulent energy cascade process. It is apparent that all initial kinetic energy eventually resides at the subgrid-scale even though it is never dissipated in this inviscid problem. Once the kinetic energy resides at the subgrid-scale, it is indistinguishable from internal energy except through a model. As a result, the numerical algorithm must sufficiently dissipate represented-scale kinetic energy while correctly capturing the energy cascade process. This test

case will demonstrate the dissipative characteristics of the algorithms when physical viscosity is absent.

6.3 Decaying Homogeneous Turbulence

Decaying, grid-generated turbulence is a classic test of the capabilities of LES models and multiple experimental datasets are readily available for this case [90, 92, 93]. This particular study simulates the Comte-Bellot and Corrsin experiment [90] following the numerical procedure outlined by Rozema, et al. [94] and partially developed by Kang et al. [95].

The experimental case consists of a bulk flow, U_{ref}, of 10 m/s through a mesh with a spacing between wires, L_{ref}, of 0.0508 m. A characteristic time, τ, is defined as

$$\tau = t\frac{U_{\text{ref}}}{L_{\text{ref}}}\,, \tag{6.14}$$

where t is the true physical time. If a reference-frame is chosen to convect with the flow, a change in spatial location can be correlated with a change in time in the convecting reference frame. Measurements of the one-dimensional energy spectra were performed at spatial locations corresponding with characteristic convecting reference frame times of $\tau = 42, 98$, and 171 after the generation of the turbulence by the mesh. At the first measurement station, $\sqrt{u_1^2}$ was measured to be 0.222 m/s and the Kolmogorov scale was determined to be 2.94×10^{-4} m.

To numerically simulate this case, a domain reference length, D_{ref}, was chosen as $11L_{\text{ref}}$ and a local turbulent velocity reference value of u_{ref} was chosen as $0.222\sqrt{3/2}$ m/s in order to match the experimental value of $\sqrt{u_1^2}$. All computational parameters were nondimensionalized by D_{ref} and u_{ref} as necessary. An algorithm-dependent, divergence-free initial condition with random phase shifts was fit to the energy spectrum measured at the first station ($\tau = 42$). Each case was run with the algorithm specific initial condition from $\tau = 0$ to $\tau = 42$. The resulting flow fields were each rescaled following the method proposed by Kang et al. [95] in order to act as the initial condition for the simulations in this particular study. In the present study, the cell-averaged field at $\tau = 42$

was deconvolved using the same method as presented in McCorquodale and Colella [79] to obtain the point-value field that could be rescaled. Following the rescaling of the point values, the rescaled cell-averaged field was computed using a box-filter convolution operator. The rescaled fields were then used as initial conditions to run from $\tau = 42$ to $\tau = 171$. The Reynolds number based on u_{ref} and the domain size was 10400. Meshes of size 64^3, 128^3, and 256^3 are used for all decaying homogeneous turbulence simulations in the present study.

6.4 Data Analysis for First Three Cases

A non-dimensional, characteristic time, τ, is utilized for the first three test cases presented. This "eddy turn-over" time is defined as

$$\tau = t\frac{U}{L}\ , \tag{6.15}$$

where U is a characteristic velocity and L is a characteristic length-scale. For the shear-layer case, the characteristic time scale is computed from the arithmetic mean of the absolute values of the two stream velocities and the initial momentum thickness. For the inviscid Taylor-Green vortex the characteristic scales are chosen to be the velocity fluctuation magnitude, U_0, and the integral length-scale, while for the decaying homogeneous turbulence case, these are the convective velocity and the mesh spacing. The shear-layer spectrum transitions to fully developed turbulence by $\tau \approx 20$. The decaying Taylor-Green cases transition to fully developed turbulence by $\tau \approx 10$. After this point, the kinetic energy decays away due to the energy cascade process.

The results of interest in the first three cases in this study are presented using the three-dimensional kinetic energy spectra from each case. All spectral data is computed from instantaneous flow data using the software package FFTW. To compute the three-dimensional energy spectra, the square of the Fourier-transformed velocity vector is summed over constant-wavenumber shells. The resulting kinetic energy is then normalized using the simulation domain volume and the initial sum of kinetic energy such that the sum of the kinetic energy presented in the spectrum

plots is equal to unity at the start of the simulation. The wavenumber, k, is given with respect to the simulation domain such that $k = 1$ is the largest wave mode fully contained in the periodic simulation domain.

For each of the unbounded turbulent flow test cases presented, the kinetic energy spectrum results are broken into five distinct parts gathered into two separate figures. The first column of the first figure for each test case compares the use of three different numerically regularized algorithms: the fourth-order centered discretization with the SV model (explicit LES), the fourth-order PPM algorithm (implicit LES), and the fifth-order algorithm (implicit LES). The second column of the first figure presents the coupling between the SV model and the last two numerical regularization techniques presented in the first column. This particular set demonstrates issues that arise from naive couplings of the LES SGS model with numerical regularization techniques (when $\Delta_f = \Delta x$). For the third column, the SV model is used with and without numerical regularization and specifically utilizes the coarsening method proposed in this study ($\Delta_f \neq \Delta x$). The second figure of kinetic energy spectrum for each simulation displays the comparison between the various schemes using the coarsened SV model at single mesh resolutions. The first row shows the kinetic energy spectra as previously described, while the second row displays the kinetic energy premultiplied by the wavenumber, k, and placed in a log-linear plot. This last presentation of the results is intended to specifically highlight the largest wave modes and demonstrate whether or not the simulation results are grid-converged. The first two columns of spectra in the first figure are intended to show the baseline performance of the algorithms presented. The last column of the first figure highlights grid-independence achieved by the coarsened SV model computation. The second figure highlights scheme-independence achieved by the coarsened SV model computation, in that all numerical regularization approaches converge to the same result.

6.5 Flat-Plate Turbulent Boundary-Layer

A standard wall-model test case, the zero-pressure-gradient flat-plate turbulent boundary-layer (ZPGFPTBL), was chosen as a test case due to the widely available literature with which to compare the the results of this test. Previous researchers have also used this case to test the stretched-vortex model wall-model, and this case will be based on the incompressible simulations of Inoue & Pullin [68]. The general setup of the simulation is shown in Fig. 6.2.

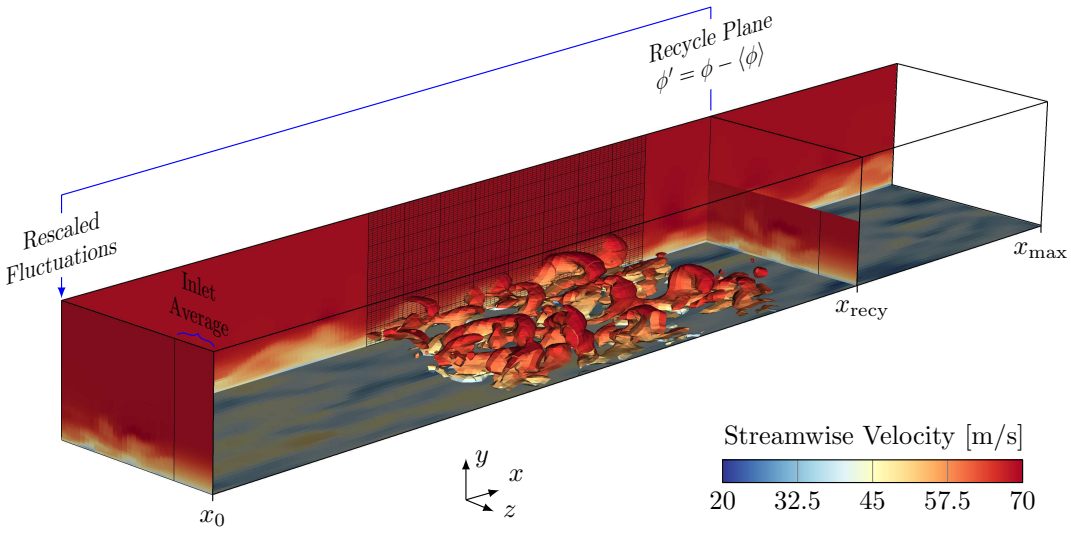

Figure 6.2: Configuration of the flat-plate turbulent boundary-layer.

In terms of the inlet boundary-layer thickness, $\delta_{99,\text{inlet}} = 0.036$, the physical domain size is $L_x \times L_y \times L_z = 85.85\delta_{99,\text{inlet}} \times 4.77\delta_{99,\text{inlet}} \times 7.15\delta_{99,\text{inlet}}$ in the streamwise, wall-normal, and spanwise directions respectively. Throughout this dissertation, two mesh resolutions are used to test the methods presented. The first mesh resolution, what will be referred to as the very-coarse (VC) mesh from here on, has $192 \times 32 \times 16$ cells in the streamwise, wall-normal, and spanwise directions respectively. The second mesh resolution, referred to as the coarse (C) mesh, has $384 \times 64 \times 32$ cells in the streamwise, wall-normal, and spanwise directions. One simulation is presented which was performed using the resolution of the very-coarse mesh, but a domain twice as long ($L_x = 171.7\delta_{99,\text{inlet}}$ and $384 \times 32 \times 16$ cells). This case will be referred to as the VC case with $2L_x$. These

mesh resolutions are compared with Inoue & Pullin who use resolutions of $192 \times 64 \times 32$ (coarse (C) resolution), $384 \times 128 \times 64$ (medium (M) resolution), and $768 \times 256 \times 128$ (fine (F) resolution). Note that Inoue & Pullin used a streamwise-domain-length that was half as long as that used in the current simulations. The simulation has an inlet boundary-layer thickness Reynolds number, $Re_{\delta_{99,\text{inlet}}} = \rho_\infty u_\infty \delta_{99,\text{inlet}}/\mu$, of 167,000, a freestream Mach number, Ma, of 0.2, a Prandtl number, Pr, of 0.71, and a specific heat ratio of 1.4.

In order to achieve a quality solution on a small simulation domain, the case uses a turbulent boundary-layer inflow condition and a characteristic-type outflow boundary. Additionally, the case uses periodic boundaries in the spanwise direction, a farfield, freestream condition as part of a characteristic-type farfield boundary condition at the top of the domain, and an adiabatic no-slip wall as the flat-plate wall-boundary. Inoue & Pullin follow the widely used practice of introducing a developed turbulent boundary-layer as the inlet condition through the method of rescaling-and-recycling [96]. Essentially, a streamwise-normal sample plane is chosen within the domain somewhere downstream of the inlet for the purposes of collecting turbulent fluctuations. For the cases presented in this dissertation, the recycling plane is placed downstream of the inlet at $0.75L_x$. The turbulent fluctuations collected at the sampling plane are rescaled to match the height of the inlet boundary-layer and are recycled to the inlet. Since the fluctuations do not perfectly match the inlet state, a small inlet region is in a state of numerical non-equilibrium and should be excluded when post-processing and analyzing simulation data.

Researchers have previously demonstrated a spurious periodicity in the streamwise turbulence data [97]. Additional research has also demonstrated the development of acoustic amplification when the rescaling-and-recycling method is used in the context of a numerical algorithm solving the compressible Navier-Stokes equations. Various methods have been developed to address both issues, but within this dissertation, the simplest methods that have previously been demonstrated to work are used with success. To alleviate the streamwise periodicity, research has shown that a temporally varying spanwise shift of the recycling plane eliminates the periodicity. It was noticed in the studies presented here that the inlet non-equilibrium zone did not noticeably lengthen with

a temporally varying spanwise shift applied to the recycling plane. As a result, all simulations presented here use the recycling-plane spanwise-shifting. To address the amplification of acoustic waves within the domain, a characteristic boundary condition was developed and implemented at the outlet (see Section 5.5 for more details). The inlet state is set directly to the mean turbulent profile with the turbulent fluctuations added prior to using a Riemann solver between the interior and exterior state to resolve the two. Additionally, the density and temperature fluctuations are recycled independent of pressure. Since the mean state uniformly enforces the freestream pressure value throughout the entire boundary-layer, it is possible to recycle the thermodynamic fluctuations without enforcing the freestream pressure value.

6.5.1 Inflow Turbulent Boundary-Layer Mean State Profile

Simulations of flat-plate turbulent boundary-layers can be particularly sensitive to the profile of the mean inflow conditions. For the simulations presented within this dissertation, the mean van-Driest-transformed streamwise velocity for the inlet-flow profile was computed using Eq. (4.39). The van-Driest transform is a method for transforming compressible boundary-layer profiles to match incompressible boundary-layer profiles. For all the flat-plate cases presented here, the relatively low Mach number should show very little compressible effect in the turbulent boundary-layer profile. As a result, using the van-Driest profile is unnecessary, but for the sake of generality, it is used here.

Starting with the incompressible velocity profile defined by Eq. (4.39), the van-Driest transformation can be reversed to obtain the equivalent compressible boundary-layer profile. The inverse van-Driest transform is defined as

$$u_{vd} = \frac{u_\infty}{\alpha} \sin^{-1}\left(\frac{\alpha u}{u_\infty}\right) \tag{6.16}$$

where u_{vd} is the van-Driest-transformed velocity, u_∞ is the freestream velocity, and α is given by

$$\alpha = \sqrt{\frac{\frac{1}{2}(\gamma-1)M_\infty^2 Pr_t}{1+\frac{1}{2}(\gamma-1)M_\infty^2 Pr_t}}\,, \tag{6.17}$$

where Pr_t is the turbulent Prandtl number and is assumed to be 0.89 for these cases [98].

The mean wall-normal velocity is specified assuming that the mean velocity state is divergence free. To compute the wall-normal velocity, an assumption regarding the streamwise growth of the boundary-layer thickness is required. The boundary-layer thickness is assumed to follow a $1/5$-power-law [99] of the form

$$\delta_{99} = \frac{\beta x^{(1/5)}}{Re_x^{(1/5)}}\,, \tag{6.18}$$

where β is a scaling parameter which can take any value for the wall-normal velocity derivation, and where $Re_x = \rho_\infty u_\infty x/\mu$. At this point, the mean flow is assumed to be divergence free and the streamwise-derivative of the streamwise-velocity is integrated in the wall-normal direction to obtain the wall-normal velocity as

$$\bar{v} = -\frac{\left[(4yu_\tau)\,/\,(5x\kappa^2)\right]\left[1-\ln\left(yu_\tau/\nu_w\right)\right]}{(1/\kappa)+\left[u_\infty \sin^{-1}(\alpha)\,/(\alpha u_\tau)\right]}\,, \tag{6.19}$$

where $\kappa = 0.41$ is used to match the Musker profile as specified in Eq. (4.39). Finally, the mean spanwise velocity is set to be zero.

Once the mean velocity is obtained, the mean temperature variation throughout the boundary-layer can be determined using the Crocco-Busemann relation for an adiabatic wall,

$$\bar{T} = T_\infty\left(1+\frac{1}{2}(\gamma-1)M_\infty^2 Pr_t\frac{u_\infty^2-u^2}{u_\infty}\right)\,. \tag{6.20}$$

Assuming a constant pressure throughout the domain, the density profile is easily obtained through the ideal gas law.

These mean profiles are used when specifying the initial condition for the flat-plate. Additionally, a velocity perturbation is added to the mean velocity profiles with a perturbation strength that is 20% of the freestream velocity magnitude.

6.5.2 Turbulent Inflow Generation

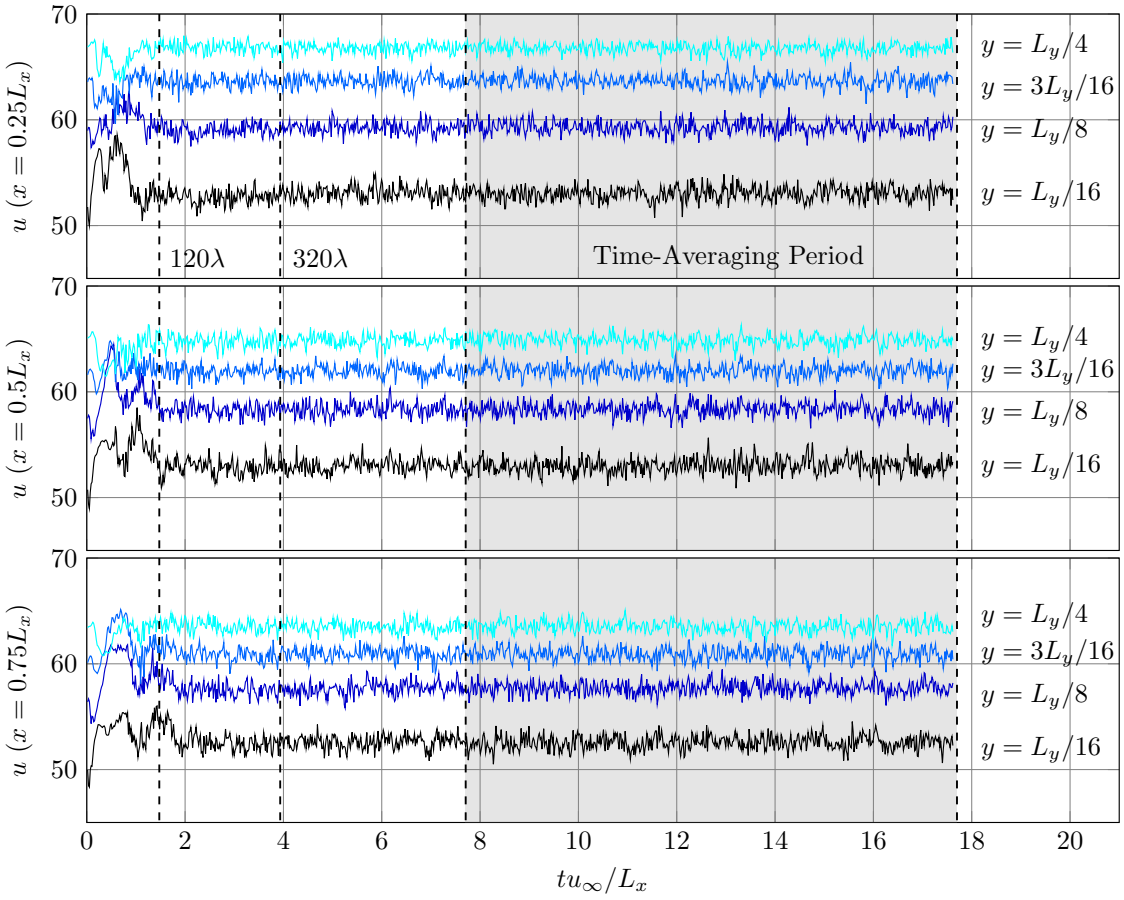

Figure 6.3: Time history of streamwise velocity for the coarsest flat-plate mesh at 3 streamwise sampling locations with 4 vertical sampling locations per streamwise station. Recycling is performed using spanwise-averages of time-averaged data at the sampling plane.

In addition to sensitivity to the mean inflow condition, flat-plate turbulent boundary-layers are sensitive to the method of introducing turbulent fluctuations at the inlet. Within this dissertation,

the rescaling-and-recycling method developed by Lund et al. and used by Inoue & Pullin is used with a similar time-averaging procedure at the recycling plane as proposed by Lund et al. [96].

At the recycling plane, an exponentially decaying time-filter is used to define the time-averaged state of the boundary-layer profile. This exponentially decaying time-filter takes the form

$$\{\langle\phi\rangle\}^n = \frac{\Delta t}{\Delta_\tau}\langle\phi\rangle^n + \left(1 - \frac{\Delta t}{\Delta_\tau}\right)\{\langle\phi\rangle\}^{n-1} \tag{6.21}$$

where ϕ is flow-field parameter being time-averaged, superscript n is a time-step index, Δt is the numerical time-step size, Δ_τ is the temporal filter length, $\{\cdot\}$ denotes a time-averaged quantity, and $\langle\cdot\rangle$ denotes a spanwise averaged quantity in the context of this equation. In order to account for the initial startup phase of the simulation and to allow any initial flow transients to not affect the time-average at the recycling plane, the temporal filter time-scale, Δ_τ, is initially set to $\lambda/2$ where λ is the boundary-layer-thickness characteristic time and is given by $\lambda = \delta_{99,\text{inlet}}/u_\infty$ in the context of this filtering operation. After allowing the transients to relax for 120λ, Δ_τ is changed to 40λ. Finally, in order to provide the highest possible quality for the time-averaged state at the recycling plane, Δ_τ is allowed to assume a running-average value after 320λ and is computed using $\Delta_\tau = t + 40\lambda - 320\lambda$, where t is the current simulation time. This formulation of Δ_τ provides a continuous switch from the constant value of 40λ to a linearly increasing filter size necessary for continuous time-integration.

Fig. 6.3 displays the streamwise velocity at multiple stations throughout the flat-plate domain ($0.25L_x$, $0.5L_x$, and $0.75L_x$) and at 4 unique wall-distances at each sampling station. From Fig. 6.3, it is apparent that the initial transient period largely takes place before the first change in the temporal-filter length-scale, justifying the length of time (120λ) chosen for the first segment of the startup-phase. By 320λ, signs of startup-transients are gone from Fig. 6.3, but the time-averaging of the solution data for the results presented in this dissertation was delayed another 300λ (approximately 4 more domain-length flow-through-times) as an added buffer out of an abundance of caution. Starting the averaging time slightly earlier (starting at 4.8 domain-length flow-through

times or 390λ) and later (starting at 20 flow-through times or 1600λ) was tested, with results showing little to no difference.

6.5.3 Coarsening and Limiting

For the flat-plate simulations, several variations of the wall-modeled LES algorithm were tested in order to begin to identify an appropriate method for coupling the wall-model, the interior stretched-vortex model, and the PPM limiter. It is important to note that, in all testing in the current dissertation, using the coarsened stretched-vortex model all the way to the wall boundary failed to provide sufficiently meaningful boundary-layer results to warrant inclusion in this study. As a result, none of the cases presented here used coarsening of the interior model right at the wall and, to maintain consistency among the models, none of theses cases used coarsening of the wall-model.

The first set of cases, referred to as SV1 from here on, used the LES models without coarsening and with the PPM limiter restricted to the farfield solution above the boundary-layer (retained in the freestream for the purpose of providing stability near the farfield boundary). The purpose for this set of tests is to provide a baseline comparison for all further modifications consisting of using model coarsening or PPM limiting.

The second set of cases, referred to as SV2, used the coarsened LES model up to 5 cells away from the boundary. At this point, the non-coarsened SGS model was blended in such that two-thirds and then one-third of the coarsened model was used at the fourth and third cells away from the boundary respectively. For the second cell away from the boundary and the wall-adjacent cell, only the non-coarsened model was used. Within this set of cases, two simulations of the very-coarse mesh are presented, the normal domain size and the long-domain case.

The third set of cases used the coarsened LES model as described for the second set of tests with the addition of the PPM limiter. Two out of the three test cases, referred to as PPM1, blended in the PPM limiter with the fourth-order centered discretization in the same manner as the coarsened model. That is, the full PPM face-interpolation was used at the fifth interior face, while two-thirds

was used at the fourth interior face and one-third at the third interior face. From the wall-face up to the second interior face, only the fourth-order centered discretization was used. The other method used in this test set, referred to as PPM2, used the PPM limiter everywhere throughout the domain all the way up to and including the wall face.

6.5.4 Data Analysis

The flat-plate results presented in this dissertation are all time-averaged results, with the time-averaging being a simple, time integration of the variables

$$\{\phi\} = \frac{1}{(t_{\text{final}} - t_0)} \int_{t_0}^{t_{\text{final}}} \phi \, \mathrm{d}t \ . \tag{6.22}$$

All results were time-averaged for 10 domain flow-through times. The case referred to as the "long-domain" case was averaged for 10 domain flow-through times as well, except that this time period was twice as long given the fact the domain was twice as long as the other cases. This particular simulation was utilized for testing the time-convergence of the averaging process in addition to testing a later averaging start time. More specifically, this case started averaging at 10 flow-through times which, again, was the equivalent of 20 flow-through times in the domain of normal streamwise length.

In addition to time-averaging the data, all quantities presented were spanwise averaged using a simple, spatial integration of the variables. This allowed for the use of shorter averaging times and is a standard procedure used for turbulence cases with spanwise homogeneity such as the flat-plate case.

For all results presented, $u^+ = u/u_\tau$ is defined as the inner-scaled mean velocity, while $y^+ = yu_\tau/\nu_w$ is the inner-scaled wall-normal distance from the wall using the kinematic viscosity at the wall. The disturbance boundary-layer thickness, δ_{99}, is computed as the wall-normal location where the mean velocity first reaches 99% of the freestream velocity defined globally, u_∞. That is, the local mean freestream velocity may be higher or lower than the globally defined value, but the

globally defined value is still the value utilized (for all the flat-plate cases presented here, the local u_∞ is the same as the global u_∞ as would be expected for a flat-plate case with a freestream farfield boundary condition). The displacement boundary-layer thickness, δ^*, is computed by integrating through the boundary-layer up to δ_{99}. Various definitions of the boundary-layer thickness and the boundary-layer edge values are utilized throughout the literature [100], but this study uses δ_{99}, ρ_∞, and u_∞ for simplicity. The calculation for δ^* is given by

$$\delta^* = \int_0^{\delta_{99}} \left(1 - \frac{\overline{\rho u}}{\rho_\infty u_\infty}\right) \mathrm{d}y \ , \tag{6.23}$$

where $\overline{\rho u}$ represents the time-averaged streamwise momentum. The momentum boundary-layer thickness follows the same method with the following equation

$$\delta^* = \int_0^{\delta_{99}} \left(\frac{\overline{\rho u}}{\rho_\infty u_\infty} - \frac{\overline{\rho u^2}}{\rho_\infty u_\infty^2}\right) \mathrm{d}y \ . \tag{6.24}$$

Empirical estimates of the boundary-layer thickness and the wall-shear-stress are presented as a comparison with the simulation results. These empirical estimates are based on the $1/5$-power-law, and are given as follows [99]

$$\delta_{99} = \frac{0.38x}{Re_x^{1/5}} \quad , \quad \delta^* = \frac{0.048x}{Re_x^{1/5}} \quad , \quad \theta = \frac{0.037x}{Re_x^{1/5}} \quad , \quad \tau_{\text{theoretical}} = \frac{0.059\rho_w u_\infty^2}{2Re_x^{1/5}} \ , \tag{6.25}$$

where Re_x is the ramp-length Reynolds number, $Re_x = \rho_\infty u_\infty x/\mu$, and where x is computed based on the distance from the theoretical start of the plate. The current x location for the empirical estimates presented in the flat-plate results is computed by adding an offset to the simulation coordinates based on $\delta_{99,\text{inlet}}$. Finally, $\overline{u_i' u_j'}$ is computed by time-averaging $u_i u_j$ and then subtracting the product of the time-averaged u_i and u_j

$$\overline{u_i' u_j'} = \overline{u_i u_j} - \bar{u}_i \bar{u}_j \ . \tag{6.26}$$

This method of computation is justifiable given that the filter operator is a time-integration or averaging operator that has been applied to a sufficiently long time period.

6.6 Smooth-Ramp Flow-Separation

The physics of smooth-body separation is critical for many engineering applications, but is generally difficult to predict with LES. As a result, the Fluid Dynamics Technical Committee of the American Institute of Aeronautics and Astronautics (AIAA) organized a workshop, held in January of 2022 [91], which focused on a smooth-body separation case. Details of the smooth-ramp geometry required by the workshop and additional details specific to the results presented in this dissertation are shown in Fig. 6.4 [91]. The general simulation workflow was designed to start with simulations of a zero-pressure-gradient flat-plate turbulent boundary-layer in order to match specified boundary-layer parameters at a specified location within the flat-plate domain. Following a successful simulation of the flat-plate turbulent boundary-layer, a smooth ramp was to be appended after the flat-plate domain. After the ramp, the domain was to continue to an outlet region where grid-stretching, numerical sponges, or filtering could be used to provide a quality outlet boundary region. Additionally, the analytic mapping used to generate the mesh for the

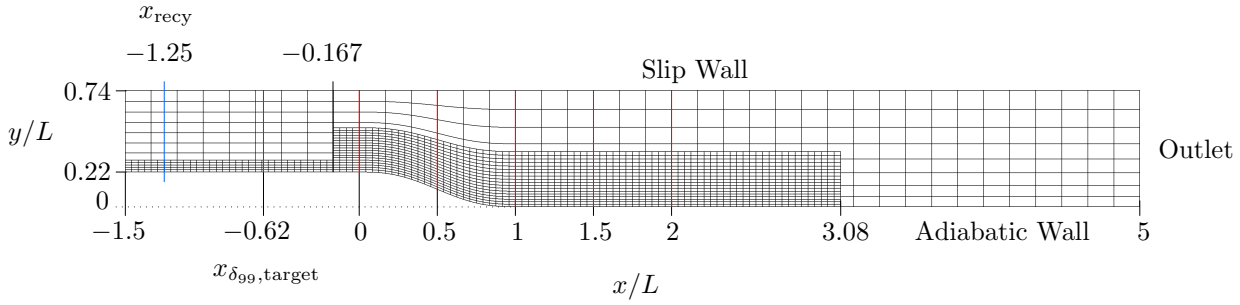

Figure 6.4: Configuration of the smooth-ramp geometry.

results presented in this dissertation is found in Appendix D.

6.6.1 Geometry and Flow Conditions

The smooth-ramp geometry is given by the following fifth-order polynomial

$$y = 0.22\left[1 - 10\left(\frac{x}{L}\right)^3 + 15\left(\frac{x}{L}\right)^4 - 6\left(\frac{x}{L}\right)^5\right], \tag{6.27}$$

where L is the length of the ramp (chosen to be 1 for all results presented here). The decision of the length of the flat-plate region at the domain inlet was left up to the workshop participants, except for the requirement that a target boundary-layer thickness, δ_{99}, be matched at $x/L = -0.62$. The target boundary-layer thickness was $\delta_{99} = 0.032$ in the flat-plate precursor simulations and was measured as the 99% boundary-layer thickness in terms of the freestream velocity prescribed at the inlet. For the results presented in this dissertation, the inlet flat-plate length was chosen to be $1.5L$. In terms of the ramp length, the flat-plate-region domain height was 0.52 while the domain width was 0.128 to allow for reasonable computational costs. After the smooth-ramp, the domain height was 0.74. The workshop specified that the domain was to extend to at least $x/L = 4$ prior to the use of grid-stretching or numerical sponge regions. Later sensitivity studies presented by other participants in the workshop showed that numerical sponge regions or grid-stretching could be applied as early as $x/L = 3$ with little impact on the resulting simulation. One group participating in the workshop did use a domain extending to $x/L = 2$ with extremely fine meshes (over a billion grid points) and the separation bubble eventually did extend nearly to the end of the domain. For the results obtained by this dissertation work, the base mesh extended to $x/L = 5$, while the AMR extended to $x/L = 3.08$.

Workshop participants were to run a sequence of structured mesh simulations with refinement such that cell-count ratios between meshes was approximately 2.5. The coarsest mesh contained approximately 4 million cells while the finest mesh contained approximately 420 million cells. Due to computational cost considerations, the results of the current study were obtained using a single mesh refinement with fixed AMR in two regions as shown in Fig. 6.4. The base-level of the mesh was generated with a refinement ratio 4 times coarser in every coordinate index than the coarsest

workshop mesh. One level of AMR with a refinement ratio of 4 was added to this coarse mesh. Both AMR regions span the entire width of the domain. The first region of AMR covered the entire length of the flat-plate inlet region and extended up to $x/L = 0.296$ or approximately $2.4\delta_{99,\text{target}}$. The second region of AMR connected with the first region of AMR and began at $x/L = -0.167$. From here, this AMR region extended to $x/L = 3$ with an initial height of $y/L = 0.502$ and a final height of $y/L = 0.351$. The total cell count on the coarse mesh was 159,744 while the total cell count on the fine mesh was 3,203,072.

Three separate ramp-length Reynolds numbers, $Re_L = \rho_\infty u_\infty L/\mu$, were initially specified by the workshop, but the majority of the workshop participants chose to run the $Re_L = 1\times10^6$ case. The results presented in this dissertation also use $Re_L = 1\times10^6$. The workshop specified a freestream Mach number, Ma$= u_\infty/\sqrt{\gamma p_{\text{inlet}}/\rho_{\text{inlet}}}$, of 0.2 and a Prandtl number of 0.71. In addition to using these values for the simulation results presented here, the freestream velocity and density were set to $1\,\mathrm{m/s}$ and $1\,\mathrm{kg/m^3}$ respectively while the inlet pressure was set to $17.857\,\mathrm{Pa}$. Assuming an isentropic, divergence-free background flow exists, approximations of the outlet velocity and pressure were computed and, the outlet pressure was set to $18.1\,\mathrm{Pa}$. Additionally, due to the distance of the outlet from the ramp and the grid coarsening used, a reflecting outlet condition was specified at the outlet using an approximation of the outlet mean velocity ($0.7027\,\mathrm{m/s}$) and the outlet pressure. The outlet density was set equal to the inlet density. The rescaling-and-recycling method used for the flat-plate turbulent boundary-layer case was used for this case with an inlet boundary-layer thickness $\delta_{99} = 0.014$. The recycling plane was situated at $x/L = -1.25$ which was found to be sufficiently far from the target location in the flat-plate domain to achieve a developed boundary-layer profile. The entire lower boundary of the domain was set to be an adiabatic no-slip wall, while the top of the domain was set to be an adiabatic slip-wall and the spanwise boundaries were set to be periodic. The initial velocity field was perturbed with a fluctuation magnitude of $0.4\,\mathrm{m/s}$.

6.6.2 Additional Simulation Details

Based on the results from the flat-plate turbulent boundary-layer case, the smooth-ramp simulation was performed without coarsening the stretched-vortex model. The simulation was first allowed to develop for 80 τ_L, where $\tau_L = L/u_\infty$. The case was then restarted and run for an additional 20 τ_L, at which point the solution-data-averaging ran for an additional 40 τ_L. Based on preliminary results and further flat-plate test cases, the PPM limiter was used only at AMR boundaries on the fine-mesh. These boundaries were kept sufficiently far from the turbulent flow to ensure that the limiter did not interact with the turbulence. Additionally, this case was run with the wall-normal velocity at the wall-boundary provided by the wall-model.

6.6.3 Data Analysis

Data analysis for this smooth-body separation case follows that of the flat-plate problem. In addition to the quantities presented by the flat-plate case, the separation and reattachment locations were computed at every time-instant by performing a spanwise average of the wall-shear-stress vector, $\vec{\tau}_w$, and then evaluating the location of the first and last sign change of $\vec{\tau}_w$. While this did capture unsteady vortex shedding events in the output of the reattachment point, these quantities still provide a picture of the instantaneous behavior of the separation bubble.

Nine point-probes were used to collect time-histories of the instantaneous, spanwise-averaged streamwise, wall-normal, and spanwise velocities. These nine probe locations were placed progressively further down the flat-plate and ramp and had $x/L, y/L$ coordinates of (-0.62, 0.238), (-0.15, 0.238), (0, 0.237), (0.25, 0.215), (0.5, 0.16), (0.75, 0.13), (1, 0.108), (1.3, 0.07), and (1.75, 0.039). Additionally, six vertical line-probes were used to sample time-averaged data throughout the domain. These line probes, shown as the vertical red lines in Fig. 6.4, were located at x/L values of -0.62, 0, 0.5, 1, 1.5, and 2.

6.7 High-Performance Computing

In order to meet the demands of modern engineering, CFD must be capable of effectively utilizing modern high-performance computing (HPC) architectures. As mentioned in Section 5.1, the algorithm used for all simulations within this dissertation is built upon a highly parallelizable AMR framework. The scale of several of the simulations tested in this dissertation required parallelization on the order of a few thousand cores and, as a result, moderate to large HPC systems were utilized for most simulations presented here.

For day-to-day operations, testing, and simulations of moderate size, Colorado State University CFD & Propulsion Laboratory has a dedicated HPC cluster, Atlantis, with 9 compute nodes providing a total of 200 cores. Additionally, some of the simulations presented here (most notably, a select few of the Taylor-Green vortex cases) were run on the Department of Energy HPC system Cori. At the time of these simulations (early 2019), Cori was ranked as the 12th fastest computer in the world, with 622,336 cores. The majority of the simulations presented were run using various Department of Defense HPC architectures. In order of relative age (oldest to most recent), Thunder (Air Force Research Laboratory DoD Supercomputing Resource Center, AFRL DSRC, 125,888 cores), Mustang (AFRL, 56,448 cores), Centennial (Army Research Laboratory, ARL, 73,920 cores), Conrad (Navy DSRC, 50,208 cores), Gordon (Navy DSRC, 50,208 cores), Onyx (U.S. Army Engineer Research and Development Center, ERDC, 217,128 cores), Narwhal (Navy DSRC, 290,304 cores), Warhawk (AFRL, 139,776 cores), and Blackbird (AFRL) were utilized for simulations and post-processing work.

Chapter 7

Results

The results are presented following the same order as Chapter 6. The first three cases address the interior stretched-vortex SGS model with periodic domains and decaying turbulence. These three cases consist of a temporally-evolving mixing-layer, a decaying, inviscid Taylor-Green vortex, and a decaying, homogeneous turbulence case. The second-to-last case presents a validation of the stretched-vortex wall-model implementation, while the last case focuses on flow separation over a smooth-ramp.

7.1 Time-Evolving Mixing-Layer

The double-shear-layer results presented in this section consist of a three-dimensional kinetic energy spectra plot demonstrating the kinetic energy evolution in Fig. 7.1, vorticity contours demonstrating the flow evolution in Fig. 7.2, and three-dimensional kinetic energy spectra in Figs. 7.3–7.4.

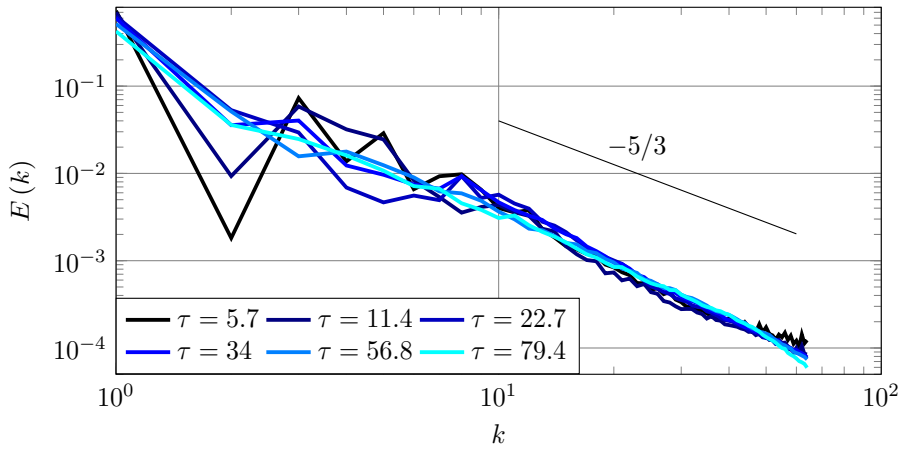

Figure 7.1: Double-shear-layer time evolution of kinetic energy spectrum using the fourth-order SV model and no numerical regularization on a $128 \times 128 \times 64$ mesh with $\Delta_f = \Delta x$.

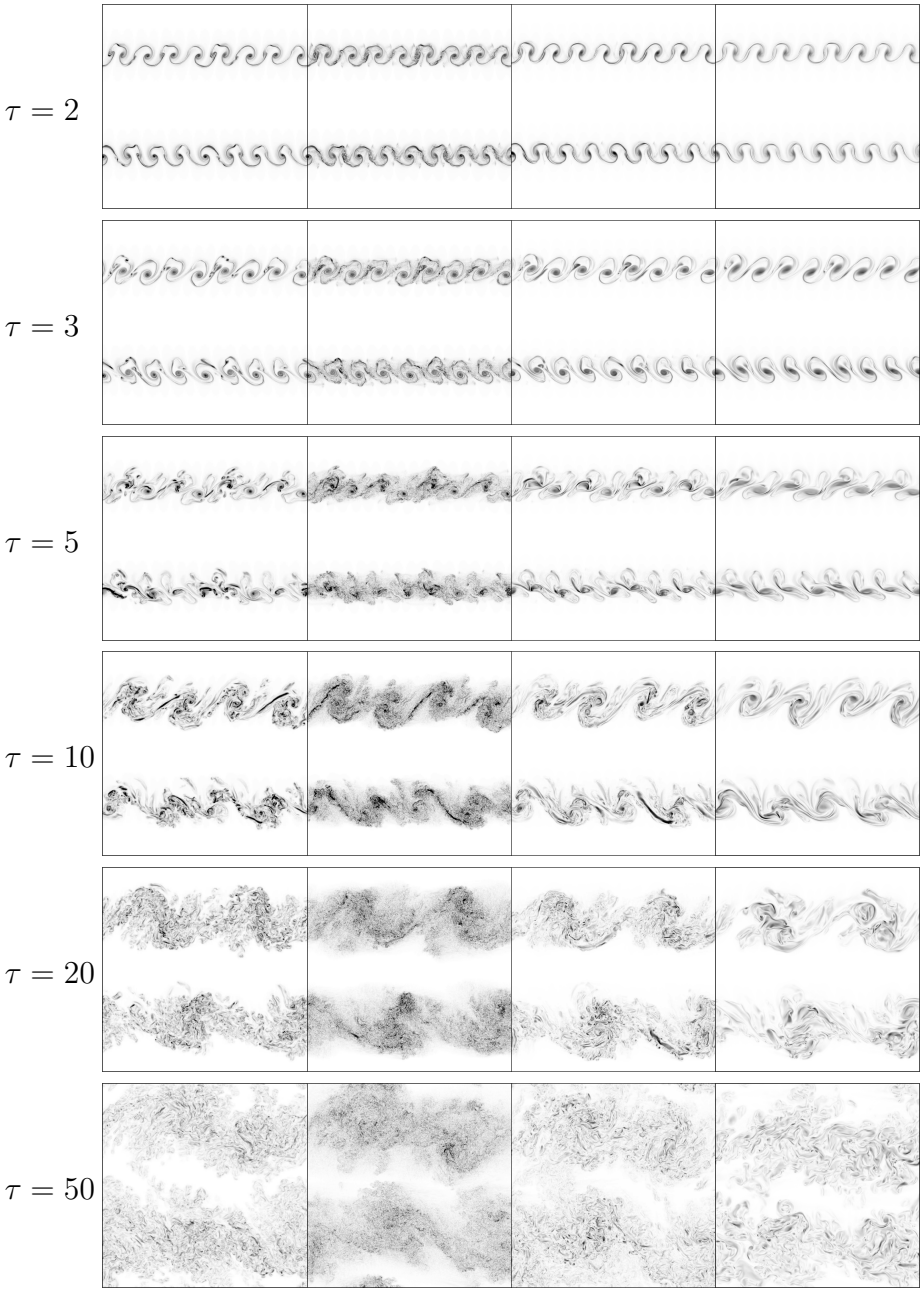

Figure 7.2: Evolution of double-shear-layer vorticity magnitude from $\tau = 2$ to $\tau = 50$, mesh size $512 \times 512 \times 256$. Rows from top to bottom display increasing simulation time while each column presents a different numerical scheme. The vorticity magnitude presented here is in grayscale contours ranging from white = 0 [s^{-1}] to black = 75,000 [s^{-1}].

As shown in Fig. 7.2, the double-shear-layer problem begins with the development of coherent vortices. These vortices rapidly break down and lead to full development of the kinetic energy spectrum by $\tau \approx 20$ as seen with the use of the fourth-order centered discretization with the SV model and no numerical regularization in Fig. 7.1. The two layers continue to evolve in a turbulent manner and grow in the shear-layer normal direction until they begin interacting with one another at $\tau \approx 35$. Between $\tau \approx 20$ and at least $\tau \approx 80$, the kinetic energy spectrum is in a quasi-steady state, mimicking artificially forced turbulence quite well. This quasi-steady state turbulence allows for the study of the various algorithms over long periods of time at moderate Reynolds numbers.

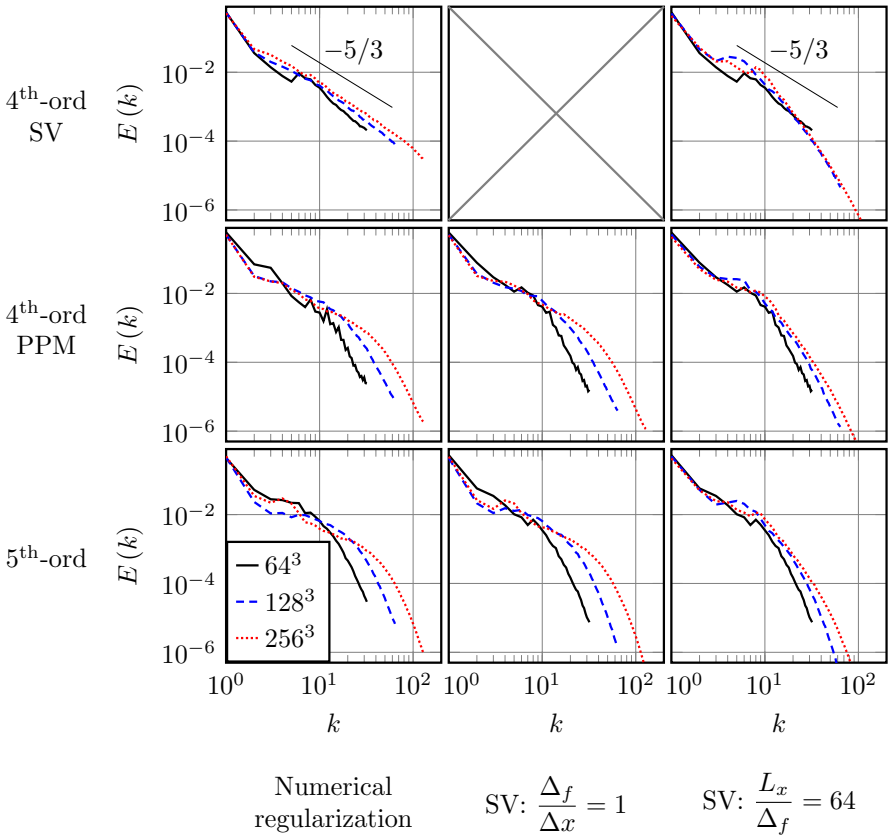

Figure 7.3: Kinetic energy spectra of double-shear-layer case at $\tau = 50$. The first column presents three methods of numerical regularization: the SV model (row 1), the PPM method (row 2), and biased interpolation (row 3). The second column adds the SV model to the PPM method (row 2), and the biased interpolation (row 3). The final column presents the same schemes except with a fixed Δ_f equivalent to $1/64^{\text{th}}$ the streamwise length of the domain.

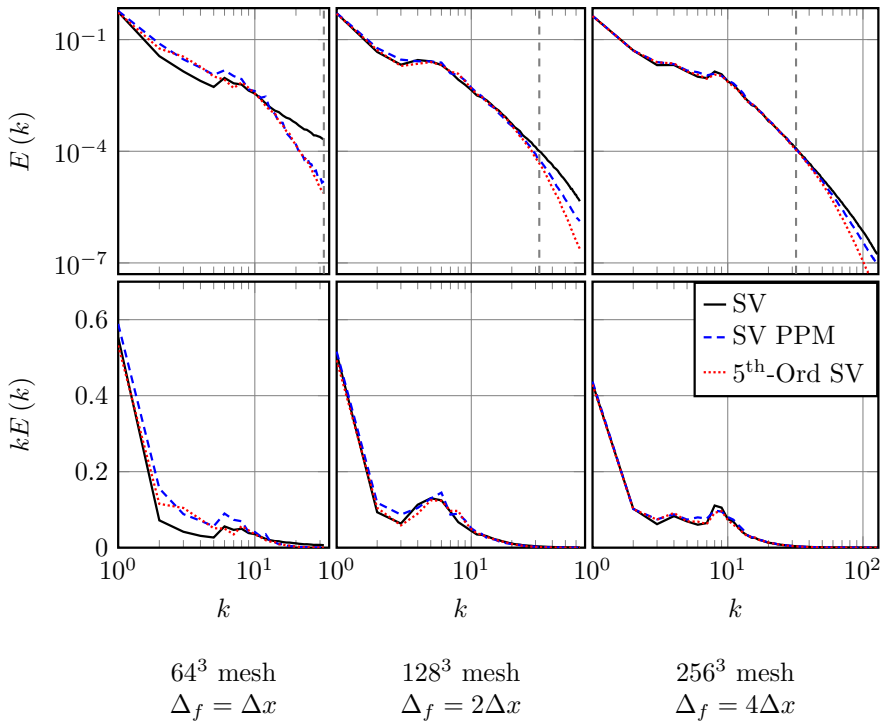

Figure 7.4: Kinetic energy spectra of double-shear-layer case at $\tau = 50$: comparison between the fourth-order SV algorithm, the fourth-order SV PPM algorithm, and the fifth-order SV algorithm with a fixed Δ_f for the SV model. The first column presents the results using a 64^3 mesh with $\Delta_f = \Delta x$, while the second column uses a 128^3 mesh with $\Delta_f = 2\Delta x$ and the third column uses a 256^3 mesh with $\Delta_f = 4\Delta x$. The first row presents the results in log-log form while the second row premultiplies the kinetic energy by the wavenumber, k, and presents the results in log-linear form to highlight the largest scales of the simulation. The dashed gray vertical line at $k = 32$ in the plots of the first row displays the wavenumber at which the model is computed.

Examining Fig. 7.2 provides a means of visualizing the differences between using numerical regularization without the SV model and using the SV model with no additional numerical regularization. The first column presents the results from using the fourth-order PPM scheme with no turbulence model, while the second, third, and fourth columns present the results from using the SV model with $\Delta_f = \Delta x$, $\Delta_f = 2\Delta x$, and $\Delta_f = 4\Delta x$ respectively. From the results of the first column, it is observed that the PPM method dampens most high-frequency solution content (as compared with the SV model results in the second column) while still allowing some small-scale flow features to develop. Examining column two of Fig. 7.2, it is readily apparent that the SV model with $\Delta_f = \Delta x$ allows a larger amount of high-frequency data to remain as compared

with the PPM method. However, as the coarsening factor of the SV model is increased beyond unity ($\Delta_f > \Delta x$), the solution field retains less high-frequency content as displayed in columns three and four of Fig. 7.2. Instead, only the larger-scale vortices remain and the resolvability of the flow field increases. This increase in resolvability decreases the likelihood that poorly resolved fluctuations will contaminate the well-resolved large-scale information. It is also important to note that the overall structure of the largest-scale vortices remains relatively unchanged as the $\Delta_f/\Delta x$ ratio is increased for the SV model. The SV model only removes more of the small scales as the $\Delta_f/\Delta x$ ratio increases, allowing for the potential of grid-independent solutions.

Figure 7.3 presents a comparison of several schemes used to simulate the double-shear case. The first column is a comparison of three methods of numerical regularization: the fourth-order SV algorithm (first row), the PPM method (second row), and fifth-order interpolation/hyperviscosity (third row). The second column adds the SV model to the PPM method (row 2), and the biased interpolation (row 3). In the third column, the SV model is applied at different ratios of $\Delta_f/\Delta x$ with constant Δ_f.

The fourth-order centered discretization with the SV model, presented in the first column of row one of Fig. 7.3, shows more consistency in the largest scales with decreasing Δx than either of the other two numerically regularized schemes presented in the first column. It is evident that the fifth-order interpolation performs worse than the fourth-order PPM scheme when considering the largest scales. From these results, it would be natural to conclude that the fourth-order SV algorithm should be used in this simulation, especially when strong numerical regularization techniques are unnecessary for a low Mach number flow such as this case. However, as this study provides one piece of a foundation for future simulations of high-speed, compressible, reacting turbulent flows, numerical regularization must be tested and compared with the fourth-order SV results. Additionally, it is apparent that none of these methods provides the grid-independent or scheme-independent solutions which are sought within this study.

As previously noted, column two of Fig. 7.3 displays the results of naively coupling the SV model with the last two numerically regularized schemes of the first column. If the SV model with

no additional numerical regularization performs somewhat well, it may be anticipated that adding the SV model to the fourth-order PPM method or the fifth-order interpolation would improve these results. But from the results presented in the second column of Fig. 7.3, it is seen that adding the SV model on top of the already existing numerical regularization does not significantly alter the results obtained using the stand-alone numerically regularized schemes presented in the last two rows of the first column of Fig. 7.3. To make sense of this, the form of the SV model must be considered. The model adds dissipation that is proportional in magnitude to the gradient squared. This is in contrast with methods that target only the highest frequency features in a simulation and are typically proportional to higher powers of the solution gradient. As a result, it is expected that the model dissipation affects more scales than just the smallest represented scales. The dissipation magnitude, however, is computed entirely using the smallest represented scales. When coupled with a small-scale-suppressing numerical regularization method, the SV model perceives almost no small scales and therefore assumes almost no SGS kinetic energy. In essence, the SV model works entirely on the assumption that locally unresolved velocity gradients will exist in unresolved turbulent flows, which is not always the case when numerical regularization techniques are used in the simulation. From the LES point-of-view, the numerical regularization techniques used in this study increase the effective filter width of the complete LES system. To include the SV model in the system in a scheme-consistent manner, the model terms must be computed at the proper effective filter width.

As seen in column three of Fig. 7.3, when the SV model is computed at a coarser scale than the base mesh ($\Delta_f > \Delta x$) as proposed in the present study, the results display less variation across all scales than when the coarsening is not utilized. This phenomenon occurs independent of the scheme tested, but is most pronounced in the numerically regularized cases. To compare the impact of all schemes, Fig. 7.4 compiles the results on one plot for each base mesh size. Figure 7.4 convincingly demonstrates scheme-independent simulations over coarse and medium turbulent scales using the SV model and numerical regularization. Engineering analysis often only considers larger scale dynamics and it is encouraging that by increasing Δ_f, these dynamics

converge to the same result independent of the numerical regularization that is applied. Note that the result of the third column of Fig. 7.4 is not necessarily the most accurate for this case (e.g. a smooth flow). The most accurate solution is probably that using mesh 256^3 from the first row and column of Fig. 7.3. However, for flows with discontinuities, limiting or other stabilization must be added and the approach used for Fig. 7.4 becomes highly attractive.

7.2 Infinite-Reynolds Number Taylor-Green Vortex

Figures 7.5–7.7 present the results of the infinite-Reynolds number Taylor-Green vortex case, with Fig. 7.5 demonstrating the kinetic energy spectrum fill-in over time and Figs. 7.6–7.7 showing the kinetic energy spectrum at $\tau = 20$.

As was mentioned in Section 6.4, the high-frequency information contained in the inviscid Taylor-Green vortex energy spectrum completely fills in by $\tau \approx 10$ as shown in Fig. 7.5. After the high-frequency information is fully developed, the spectrum begins to decay away rather uniformly at the highest frequencies, while the lowest frequencies decay rather non-uniformly into the higher frequencies. The straight, temporally self-similar form of the energy spectrum is expected to continue at higher mesh resolutions and later simulation times due to the lack of physical dissipation.

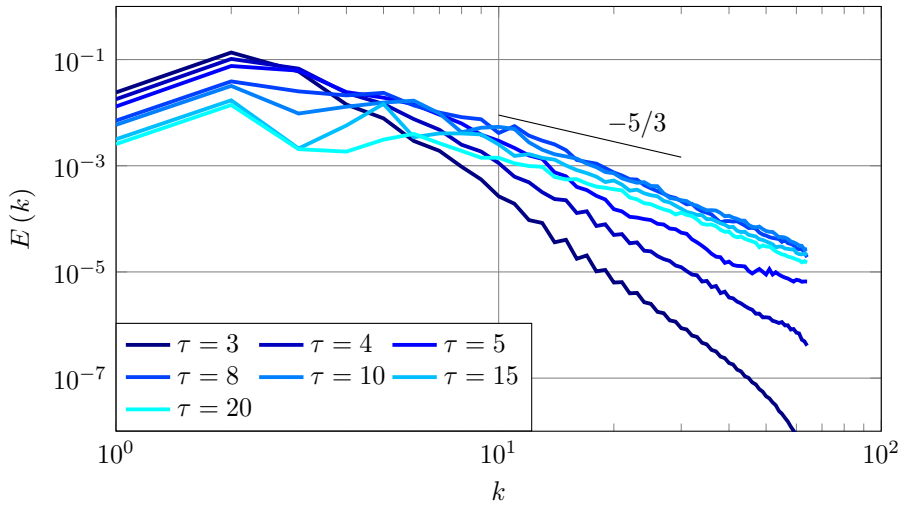

Figure 7.5: The inviscid Taylor-Green vortex energy spectrum time-evolution from the fourth-order centered scheme using the SV model and no numerical regularization with $\Delta_f = \Delta x$ on a 128^3 mesh.

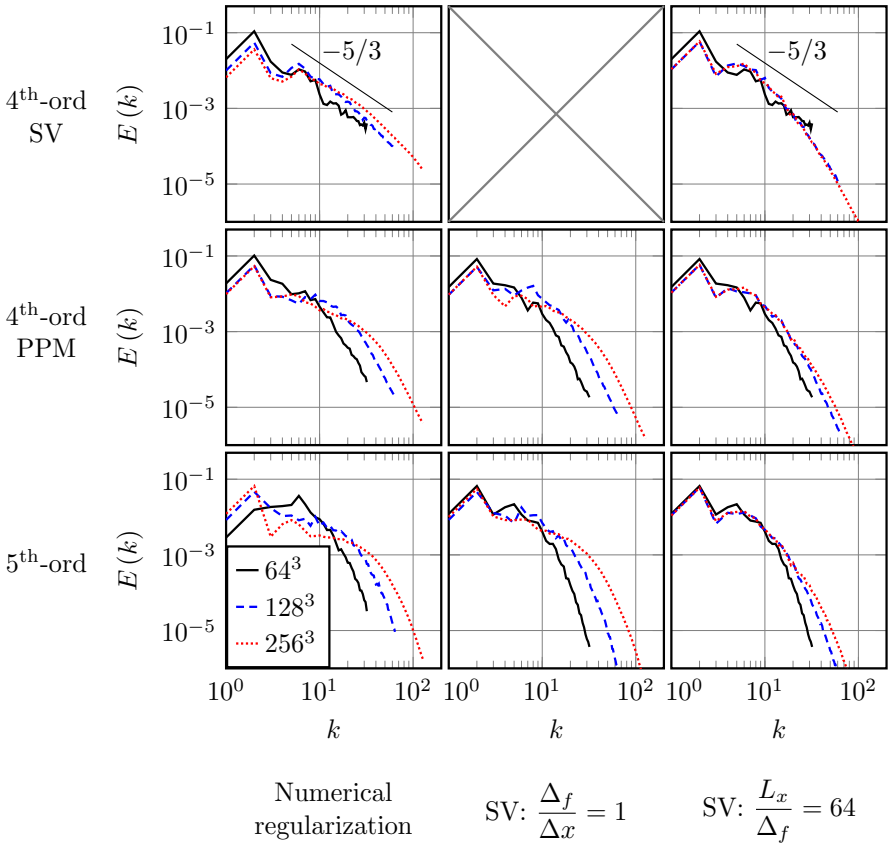

Figure 7.6: The inviscid Taylor-Green vortex kinetic energy spectrum at $\tau = 20$. The first column presents three methods of numerical regularization: the SV model (row 1), the PPM method (row 2), and biased interpolation (row 3). The second column adds the SV model to the PPM method (row 2), and the biased interpolation (row 3). The final column presents the same schemes except with a fixed Δ_f equivalent to $1/64^{\text{th}}$ the length of the domain.

Just as was seen in the previous test case, the simulation results shown in the first column of Fig. 7.6 lack large-scale grid-independence. The last two methods of numerical regularization seen in the first column are typical of implicit LES schemes used to simulate physically complex, high-Reynolds number flows. In cases of extremely-high-Reynolds number flows, where DNS results are impractical or impossible to obtain, difficulties arise when attempting to determine the quality of the implicit LES results. A reasonable expectation is for convergence in medium to large scale features as the grid is refined. This metric is used to judge the quality of the simulations in a

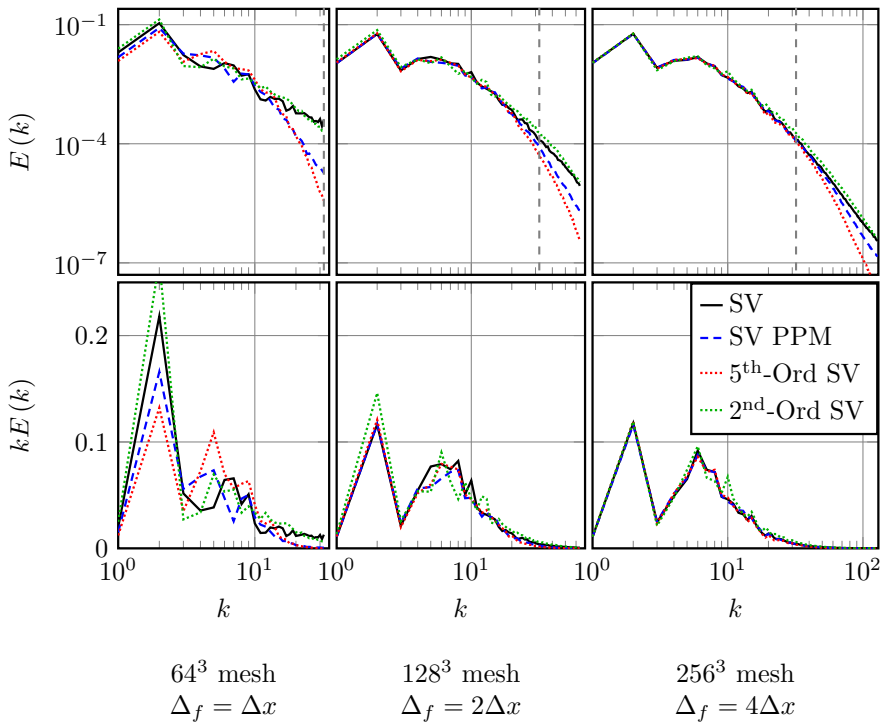

Figure 7.7: Inviscid Taylor-Green vortex kinetic energy spectrum at $\tau = 20$: comparison between the fourth-order SV algorithm, the fourth-order SV PPM algorithm, and the fifth-order SV algorithm with a fixed Δ_f for the SV model. The first column presents the results using a 64^3 mesh with $\Delta_f = \Delta x$, while the second column uses a 128^3 mesh with $\Delta_f = 2\Delta x$ and the third column uses a 256^3 mesh with $\Delta_f = 4\Delta x$. The first row presents the results in log-log form while the second row premultiplies the kinetic energy by the wavenumber, k, and presents the results in log-linear form to highlight the largest scales of the simulation. The dashed gray vertical line at $k = 32$ in the plots of the first row displays the wavenumber at which the model is computed.

meaningful way. As for the previous case, the fourth-order SV scheme shown in the first column of the first row exhibits less overall variation with decreasing Δx.

In contrast with the temporally-evolving shear-layer, column two of Fig. 7.6 shows some improvement in large-scale consistency when the SV model is coupled with the numerical regularization techniques. While the fifth-order discretization shows the most improvement from adding the SV model, the fourth-order PPM scheme shows some improvement as well. As this is an inviscid, infinite-Reynolds number case, it is expected that the numerical regularization will not eliminate all energy at the smallest representable scales. For example, if one considers a highly-compressible flow simulation which contains strong shocks, it will be noted that the smallest representable scales

still contain significant energy, even with the use of numerical regularization. The SV model can still detect small-scale energy and use this to alter the large-scale information over time. As described in the temporally-evolving shear-layer case, it is expected that matching the LES filter width to the equivalent filter size of the numerical method would provide an even greater improvement in the results. These test cases are described next.

Column three of Fig. 7.6 shows the significant improvement provided by the coarsening method. For all three schemes tested, grid-independent LES solutions are obtained with all 128^3 results nearly identical to 256^3 results. The term "grid-independent solutions" is used here in the sense that the numerical errors have been isolated from the SV model effects. Clearly, the grid-independence being seen is due to an increase in grid resolution while introducing little or no new physics to the flow field. Another form of grid-independence would be to fix the filter width with respect to the discretization size and obtain converged solutions even as new physics at smaller scales are introduced to the simulation with an increasing mesh resolution. Ultimately, one expects convergence to DNS. Such a study evaluates both the model and its overall interaction with the CFD scheme. Similar to Chung and Matheou [82], the current study does not perform such a grid-independence test.

Figure 7.7 displays scheme-independent results as were seen in the previous test case. The near complete agreement between the large scales of Fig. 7.7 points to the success of the SV model in properly regularizing high-Reynolds number turbulent flows and to independence from additional numerical regularization. An additional observation concerns the second-order result presented in this figure. The second-order result was added in order to determine whether or not the higher-order FVM provided an advantage while the coarsening was being utilized. It is evident from Fig. 7.7 that the error in the resolved scales still strongly influences the final result. As seen in Fig. 7.7, the differences in the large-scales is significant, thereby more than justifying the usage of the high-order code. The fourth and fifth-order solutions require $\Delta_f = 2\Delta x$ for the large scales to converge while the second-order solution requires $\Delta_f = 4\Delta x$. The second-order solution increases the computational expense by a factor of 2^4 when using an explicit time-marching method.

This particular case demonstrates that large-scale scheme-independence of high-Reynolds number cases is achievable and that the effect of LES SGS models can be isolated without using an explicit-filtering approach. It is also possible that other structural LES SGS models could be used with the coarsening method presented here to obtain similar grid-independent results. With care, this method could be computationally less expensive than traditional explicit filtering methods used to evaluate LES SGS model performance. Instead of computing nonlinear model terms on the base mesh and then filtering the results, the model terms are naturally filtered when they are computed on the coarser mesh, leading to a reduction in the number of necessary computational evaluations. Utilized in the setting of a high-Reynolds number turbulent flow, this method has the potential to provide an ideal test framework for the performance of various LES SGS models.

7.3 Decaying Homogeneous Turbulence

Results of the decaying, homogeneous turbulence case are presented in Figs. 7.8–7.9 which display the three-dimensional kinetic energy spectra at times corresponding with the experimental measurement stations. Figure 7.8 presents the kinetic energy premultiplied by the wavenumber, k, in log-linear format so as to accentuate the larger scales of the simulation. Figure 7.9 compares the various schemes tested using a Δ_f fixed at an equivalent resolution of 64^3.

As stated in Chapter 1, the current study aims to obtain results showing scheme and grid-independence (if possible) while using both the SV model and numerical regularization. Even for low-Reynolds number turbulent flows it may be necessary to incorporate numerical regularization in cases where strong discontinuities exist and where the physics is particularly vigorous as in reacting turbulent flows. While the current test case is not reacting and does not require numerical regularization, future studies of low-Reynolds number reacting flows will require regularization. As a result, this case continues the pattern of the previous test cases in scrutinizing the coupling of the SV model with various numerically regularized algorithms.

Similar to the previous two test cases, column one of Fig. 7.8 demonstrates that the fourth-order PPM method and the fifth-order interpolation display significant variation in the large scales with

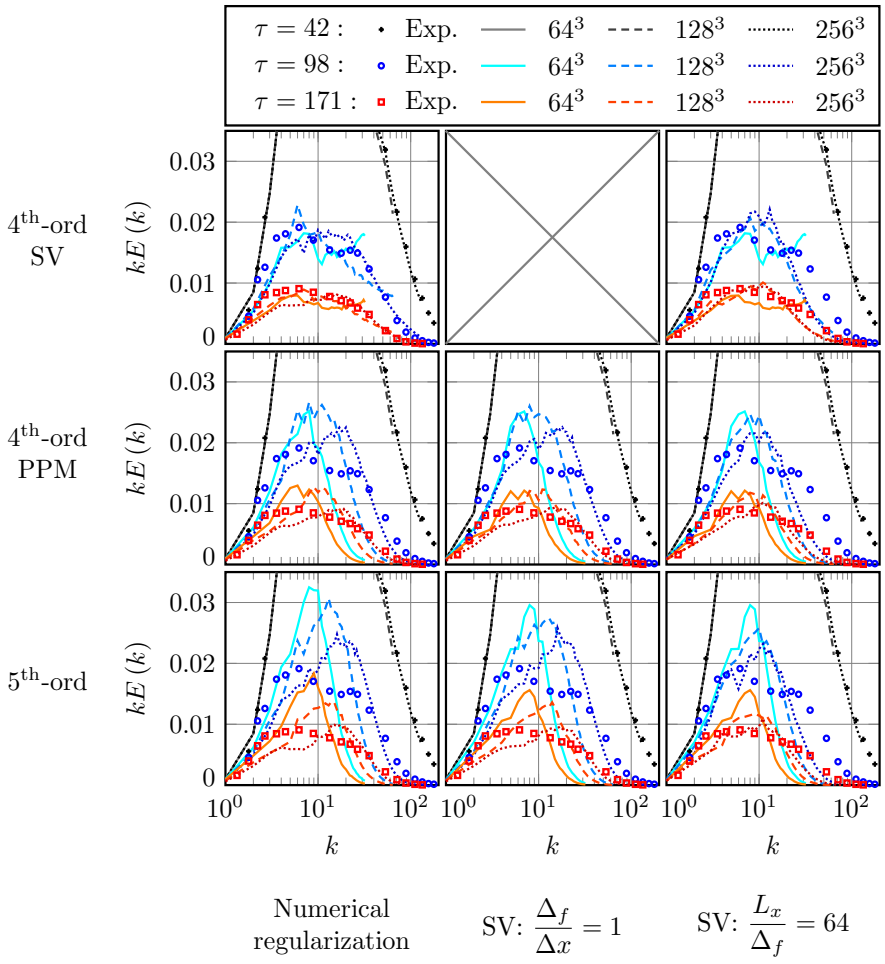

Figure 7.8: Kinetic energy spectrum for decaying homogeneous turbulence. The first column presents three methods of numerical regularization: the SV model (row 1), the PPM method (row 2), and biased interpolation (row 3). The second column adds the SV model to the PPM method (row 2), and the biased interpolation (row 3). The final column presents the same schemes as the second column except with a fixed Δ_f equivalent to $1/64^{\text{th}}$ the streamwise length of the domain. The initial conditions for $\tau = 42$ are all identical to one another and are cropped to emphasize differences in the other time scales.

changing mesh resolution. Additionally, given the experimental data, it is apparent that numerical regularization techniques tested here remove spurious high-frequency solution content while simultaneously retaining too much well-resolved kinetic energy. The resultant kinetic energy overshoot does decrease with increasing mesh resolution as would be expected, but it does not decrease to the point of matching the experimental data. In contrast to this finding is the result obtained with the fourth-order SV scheme. This scheme shows much greater consistency among the scales as mesh resolution changes and is generally much closer to the experimental data than either of the

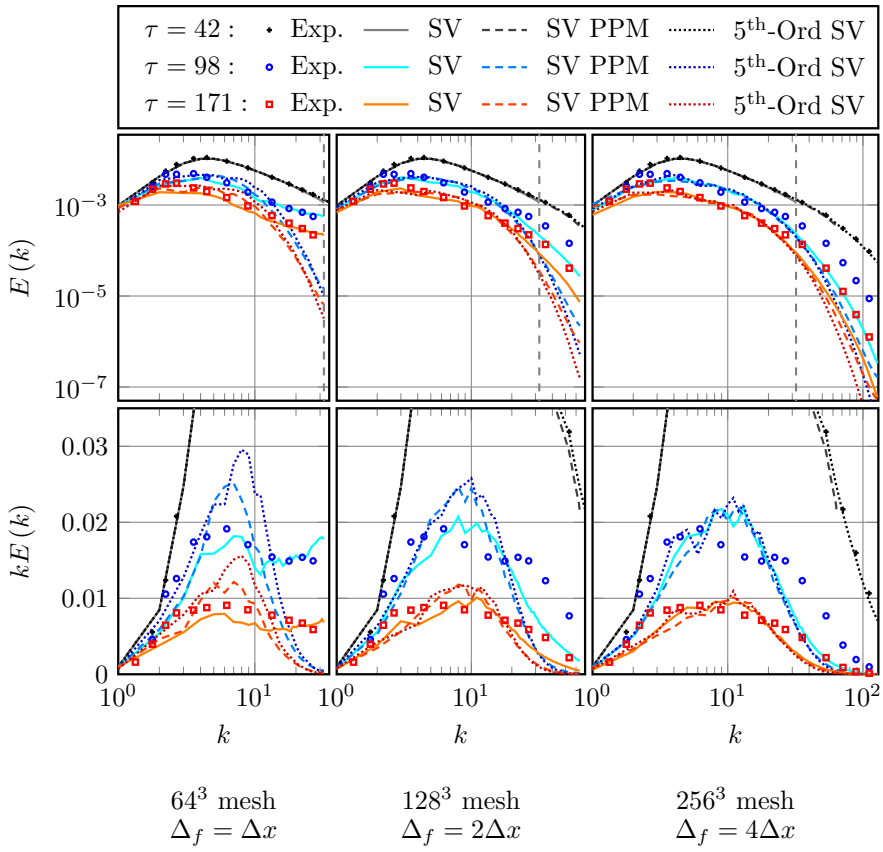

Figure 7.9: Kinetic energy spectrum for decaying homogeneous turbulence: comparison between the fourth-order SV algorithm, the fourth-order SV PPM algorithm, and the fifth-order SV algorithm with a fixed Δ_f for the SV model. The first column presents the results using a 64^3 mesh with $\Delta_f = \Delta x$, while the second column uses a 128^3 mesh with $\Delta_f = 2\Delta x$ and the third column uses a 256^3 mesh with $\Delta_f = 4\Delta x$. The first row presents the results in log-log form while the second row premultiplies the kinetic energy by the wavenumber, k, and presents the results in log-linear form to highlight the largest scales of the simulation. The dashed gray vertical line at $k = 32$ in the plots of the first row displays the wavenumber at which the model is computed.

numerically regularized schemes in column one. The comparisons in the first column demonstrate failings of ILES for this case versus a well-developed model.

As was demonstrated in the first test case, it is seen from the results of the second column of Fig. 7.8 that the naive coupling of the SV model with the fourth-order PPM method or with the fifth-order interpolation makes little to no difference as compared with the regularized schemes without the SV model. It is interesting to note that this was the case with both low-Reynolds number and medium-Reynolds number tests, while the infinite-Reynolds number case showed

some improvement when the SV model with $\Delta_f = \Delta x$ was added to the other two methods of numerical regularization.

When examining the cases utilizing the coarsened SV model as shown in the third column of Fig. 7.8, a substantial improvement over the second column of Fig. 7.8 is noted. In these figures, it must be noted that the simulations have the mesh cutoff in the dissipative range of the turbulent kinetic energy spectra, while the SV model is computed at a length-scale in the inertial range of the kinetic energy spectra. When $\Delta_f = \Delta x$, the SV model well handles a filter cutoff in the dissipative range. Having $\Delta_f > \Delta x$, Δ_f in the inertial range, and Δx in the dissipative range is a curiosity of this case. The result of the third column of Fig. 7.8 clearly shows that this is not a significant cause for concern in the decaying, homogeneous turbulence case. The implications and effects of this will be more exhaustively studied in future work. Nevertheless, grid convergence is more apparent in column 3 versus column 2 for the solutions with numerical regularization.

Similar to the first two test cases, Fig. 7.9 shows that the coarsening method nearly achieves scheme-independent solutions when the separation between the numerical regularization and the SV model is sufficient to allow the SV model to operate appropriately. The results do show some small differences between the schemes even when $\Delta_f = 4\Delta x$. Even for relatively low-Reynolds number decaying turbulence cases such as this, the coarsened SV model provides an improvement over the numerically regularized algorithms, used both with and without the SV model. Again, note that the bare SV model (row 1, column 1 of Fig. 7.8) best fits the data. But if additional numerical regularization is necessary, there is strong evidence of scheme convergence and moderate evidence of grid convergence when the SV model is applied at coarser scales. The coarsening method proposed in the current study shows that even though the SV model was designed for high-Reynolds number flows, it has the capability of working in rather low-Reynolds flows if properly coupled with the existing algorithmic components.

7.4 Flat-Plate Turbulent Boundary-Layer

The results of the zero-pressure-gradient flat-plate turbulent boundary-layer are presented in Figs. 7.10–7.18. To understand the mean velocity and Reynolds stress profiles, the wall-shear-stress provided by the wall-model and the analytical/empirical wall-shear-stress from Eq. (6.25) are presented in Fig. 7.10. The boundary-layer thicknesses δ_{99}, θ, and δ^* are presented in Fig. 7.11. Figures 7.12–7.14 present the time-averaged velocity profiles measured at momentum-thickness Reynolds numbers of $Re_\theta \approx 25,000$ and $Re_\theta \approx 28,000$. The resulting profiles are compared with experimental data from Österlund [101] at $Re_\theta = 25700$ and simulation data from Inoue & Pullin [68]. Finally, Figs. 7.15–7.18 present the streamwise Reynolds stresses, $\overline{u'u'}$, in comparison with experimental data from Fernholz et al. [102].

Just as discussed in previous sections within this chapter and as presented in Chapter 1, the goal of this dissertation is to properly couple the stretched-vortex model for the interior flow, the wall-model, and any numerical regularization/stabilization used in the algorithm. This test case specifically focuses on exploring this objective for a wall-bounded turbulent flow where experimental and numerical results are available for comparison. The following results are organized such that the cases using the interior stretched-vortex model without coarsening and without the PPM limiter are referred to as SV1, while those cases using coarsening up to 5 faces away from the boundary and then blending coarsening in until 3 faces away from the boundary are referred to as SV2. Those cases using the coarsening blending of SV2 along with blending PPM and a fourth-order centered interpolation at the same rate as the coarsening blending are referred to as PPM1, while the cases using full PPM everywhere even up to the wall along with the same coarsening method as SV2 are referred to as PPM2. In all cases presented in this dissertation, the wall-model is not coarsened.

In order to obtain more insightful interpretation of all further data analyses, the mean wall-shear-stress predicted by the wall-model is shown first. The main reason for this is that it has been found within this study that the specific prediction of the wall-shear-stress by the wall-model has a strong impact on all of the other mean-flow profiles. While this is not surprising, given the

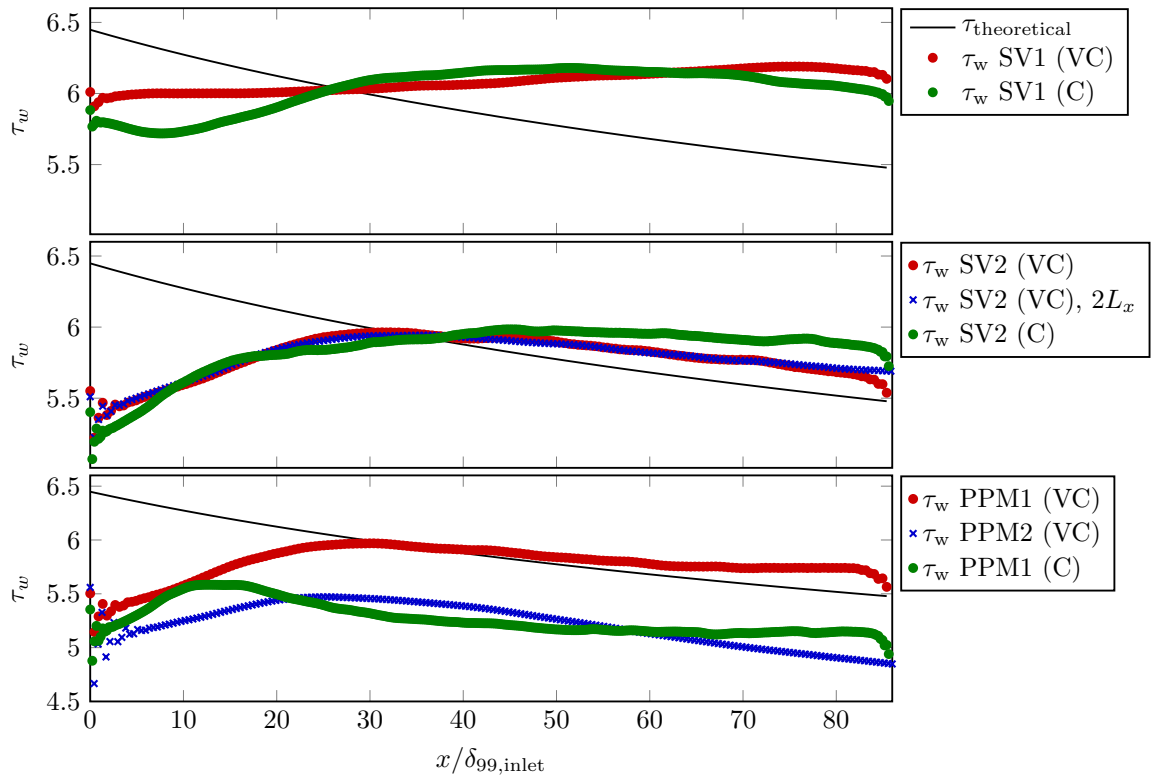

Figure 7.10: Wall-shear-stress from wall-model compared with wall-shear-stress computed based on empirical correlation.

emphasis on wall-modeling within this dissertation and within the LES community, it is important to keep this fact in mind while interpreting the results. It is also important to note that, for the sake of seeing as much detail as possible, the individual plots of Fig. 7.10 do not all have the same vertical axis extent. However, the wall-shear-stresses obtained from Eq. (6.25) is the same in all plots.

Considering the very-coarse and coarse-mesh results using the stretched-vortex model without coarsening and without numerical regularization, it is evident that the wall-model is predicting a much higher wall-shear-stress than what is predicted by the analytical profile. Examining δ_{99} for both of these cases in Fig. 7.11, it is seen that δ_{99} grows at a more rapid rate than a standard power-law estimate of the boundary-layer thickness. Similar findings are repeated for the cases using the coarsened stretched-vortex model, but τ_w has been brought closer to $\tau_{\text{theoretical}}$. Based on these results, it must be that either a slightly high wall-shear-stress prediction from the wall-model grows

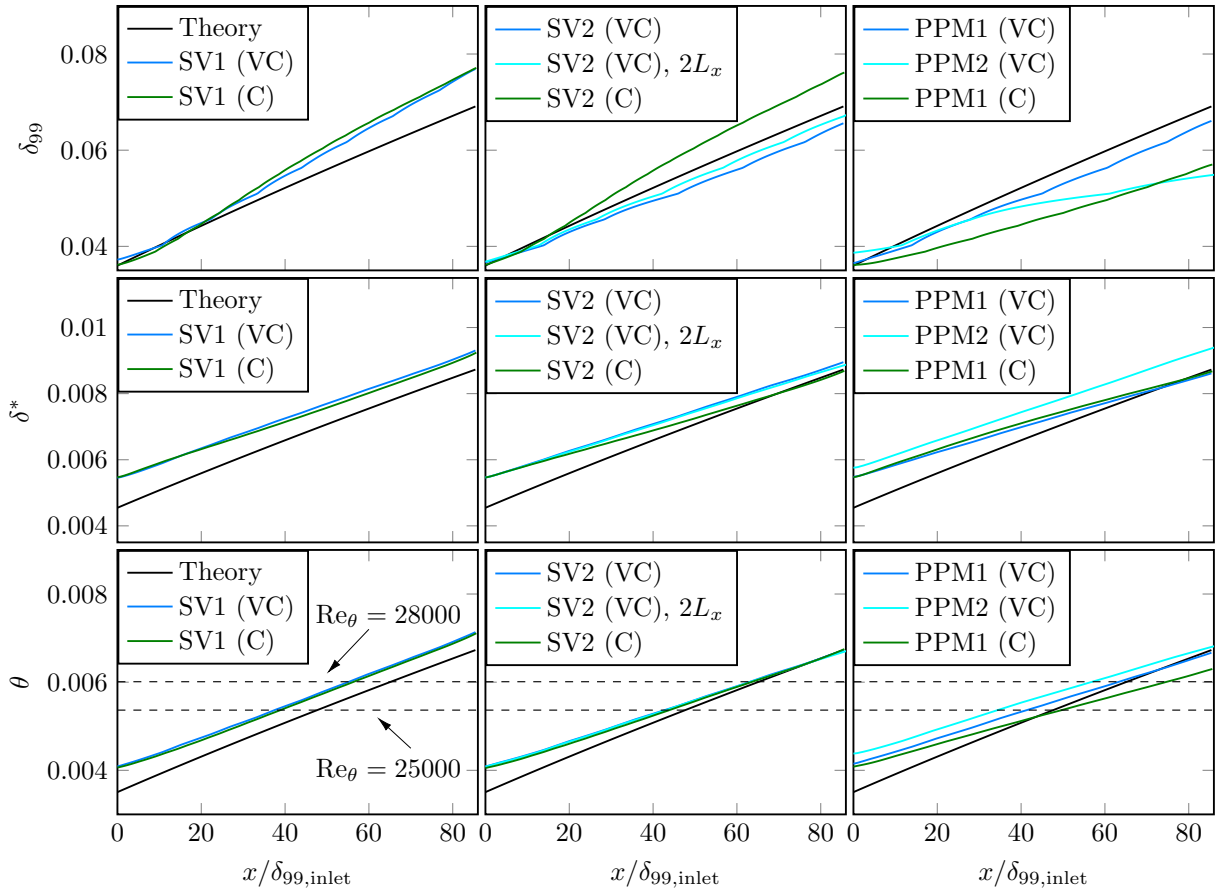

Figure 7.11: Boundary-layer thicknesses (δ_{99}, δ^*, and θ) from the flat-plate turbulent boundary-layer compared with a power-law theoretical estimate.

δ_{99} higher than what it should be or, an intermediate mechanism elevates both quantities. Looking to the displacement and momentum thicknesses for possible answers, it is seen that the results are different between the cases using the non-coarsened stretched-vortex model and the coarsened stretched-vortex model. Without coarsening, δ^* and θ trend at the same rate as the power-law estimate, while with coarsening, they exhibit a slower growth rate. This suggests that an intermediate mechanism (possibly the turbulent fluctuations) is elevating both δ_{99} and τ_w for the cases showing higher values than analytically estimated. Turning to the very-coarse mesh tests run with the coarsened stretched-vortex model, it is evident that the simulations computed using the domain length of $L_x = 81.33\delta_{99,\mathrm{inlet}}$ and the domain length of $L_x = 162.66\delta_{99,\mathrm{inlet}}$ show very similar results to one another. This finding provides confidence that a domain length of $L_x = 81.33\delta_{99,\mathrm{inlet}}$ is sufficiently

long for this case. Finally, the results obtained with the coarsened stretched-vortex model and with the PPM limiter show an under-prediction of δ_{99} in addition to displaying a slower growth rate than estimated for δ^* and θ. The very-coarse mesh using the coarsened stretched-vortex model and partial PPM shows a very similar result to the very-coarse mesh result without PPM inside the boundary-layer region. Specifically, the boundary-layer growth rates and τ_w show similar trends. To make sense of this, it must be considered that, on the very-coarse mesh, $\delta_{99,\text{inlet}}$ only spans 8 cells in the wall-normal direction. Since the PPM blending begins at the third interior face tangential to the wall boundary, the first three-eighths of the boundary-layer has no limiting and full limiting does not begin until fully five-eighths of the boundary-layer thickness away from the wall. The coarse mesh result with partial PPM starts the blending at the same face and cell indices, but this represents a blending starting twice as close to the wall with respect to δ_{99}. This clearly suggests that a percentage of the boundary-layer may need to be free of limiting in order to obtain a quality result on relatively coarse meshes. Otherwise, using limiting too close to the wall or, all the way to the wall as in the full PPM case on the very-coarse mesh, leads to a degradation in the quality of the resulting boundary-layer thicknesses and predicted wall-shear-stress.

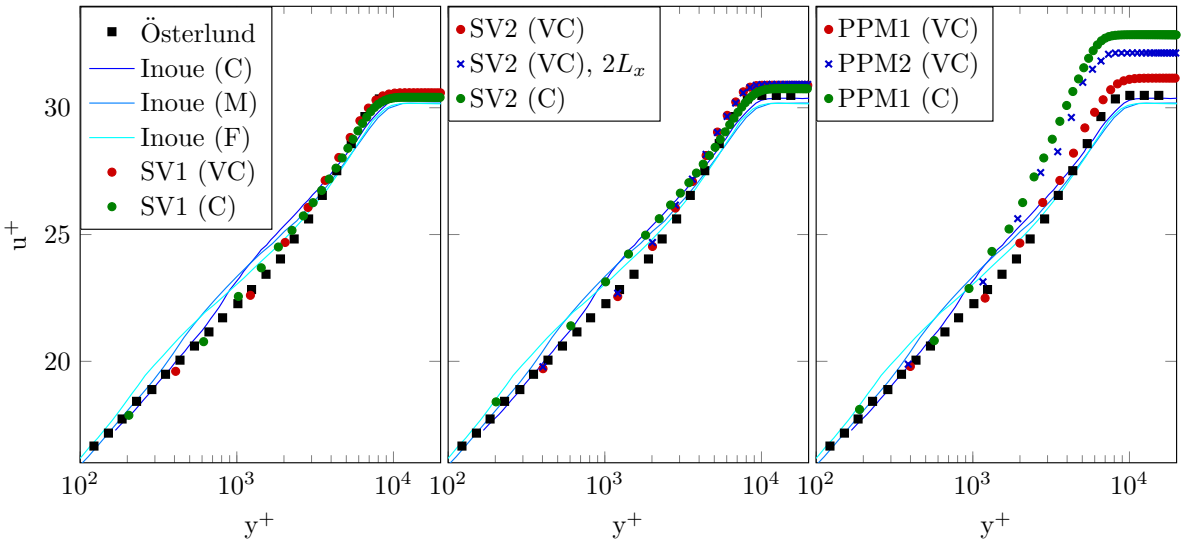

Figure 7.12: Mean streamwise velocity profile in inner-scaled units. $Re_\theta \approx 25000$.

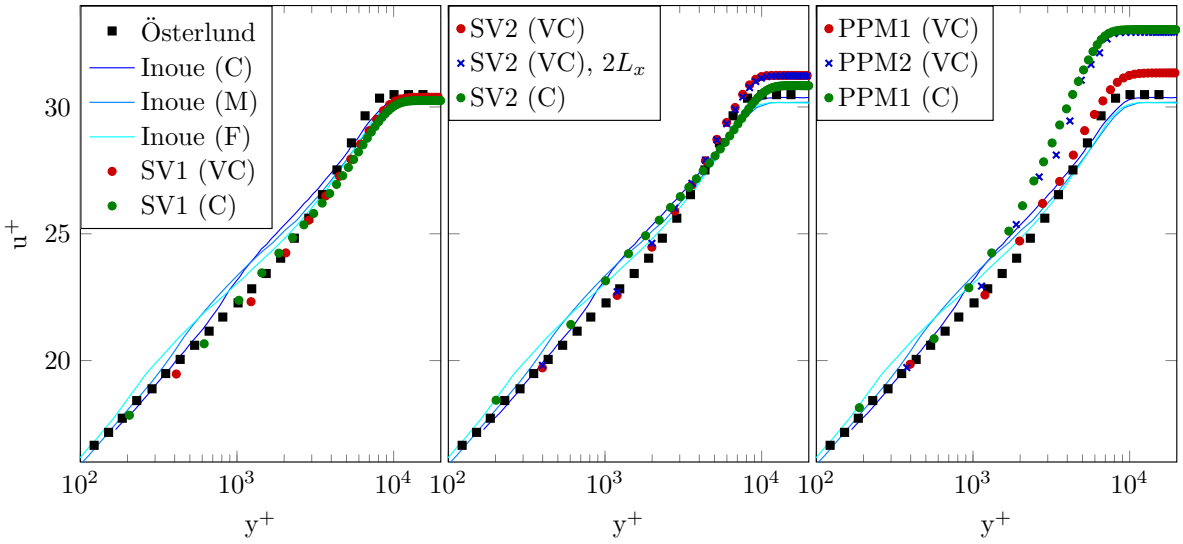

Figure 7.13: Mean streamwise velocity profile in inner-scaled units. $Re_\theta \approx 28000$.

From Fig. 7.12, it is clearly seen that the stretched-vortex model without coarsening and without numerical regularization provides the closest result to published numerical and experimental data. In fact, both the very-coarse and coarse-mesh results without coarsening and without numerical regularization are slightly closer to the experimental data than the numerical results of Inoue & Pullin. While finer results are unavailable to determine if this continues at higher resolution, it is encouraging that results of this quality are obtainable for high-Reynolds number wall-bounded turbulence on coarse meshes.

Examining the results obtained with the coarsened stretched-vortex model, it is seen that the very-coarse mesh results generally follow the same trend as the very-coarse mesh results without model coarsening. However, the coarse mesh results using the coarsened stretched-vortex model follow the coarse mesh results of Inoue & Pullin fairly closely away from the wall and away from the far freestream region. These results show the same "bump" in the mean velocity a few cells away from the wall as reported by Inoue & Pullin, who attribute it to the "log-layer mismatch" problem. Essentially, a consistent over-prediction or under-prediction of the wall-shear-stress leads to a mismatch between the very-near-wall mean-velocity profile and the profile starting a few cells away from the wall [103]. This same problem is barely seen in the results obtained using the

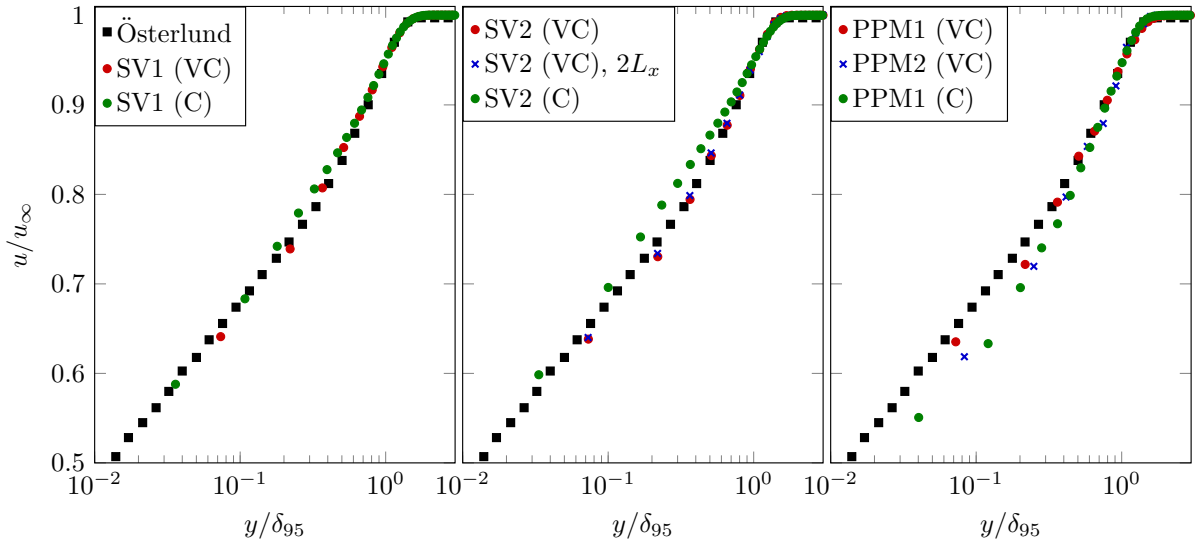

Figure 7.14: Mean streamwise velocity profile scaled by freestream velocity and δ_{95}. $Re_\theta \approx 25000$.

stretched-vortex model without coarsening. It is suggested that further studies should explore the usage of coarsening closer to the wall in an attempt to possibly alleviate this issue.

The PPM results essentially show that the wall-shear-stress is under-predicted. If the wall-shear-stress were correctly predicted by the wall-model, the freestream velocity values would collapse onto the appropriate u^+ value. Additionally, it is seen that the near-wall mean-velocity values come close to the correct value indicating that the wall-model is performing as well as it can given the flow-state that it is working with. As mentioned previously within this study, the limiter is largely suppressing unresolved gradients that are necessary for the correct operation of the interior stretched-vortex model and the wall-model. Although coarsening the model is intended to isolate the model away from the numerical method being used, it is apparent from these results that the model is not isolated sufficiently from the numerical regularization. If limiting were to be used throughout the entire flow-field (even right up to the wall), the model would have to be sufficiently coarsened so as to still view the flow as containing unresolved turbulent scales. Obviously, this requires that the coarsened mesh still adequately resolve the boundary-layer. If it is found that a coarsening ratio of 8 is required, and if the present results hold in that the model can provide quality results with only 8 cells spanning the height of the boundary-layer, the boundary-layer would

still require 64 cells in the wall-normal direction in order to begin to model the boundary-layer correctly. In the near-term, this would negatively impact the viability of this particular near-wall algorithmic-approach for engineering use.

Figure 7.13 displays the mean-velocity profiles slightly downstream at a $\mathrm{Re}_\theta \approx 28000$. Although the flow is nearly developed by the $\mathrm{Re}_\theta \approx 25000$ sampling location, it is fully developed by the $\mathrm{Re}_\theta \approx 28000$ sampling location as can be seen in Fig. 7.11. Most δ_{99} profiles in Fig. 7.11 show three general regions along the domain length. The first region is right at the inlet where all cases show an initially low δ_{99} growth rate. The second region appears quickly after the inlet and is characterized by a corrective trend of the δ_{99} growth rate toward some final δ_{99} growth rate in the third region. The $\mathrm{Re}_\theta \approx 25000$ and $\mathrm{Re}_\theta \approx 28000$ samples are located where the two dashed lines in Fig. 7.11 intersect the θ development lines for each case. As a result, it is apparent that, for nearly every case tested, $\mathrm{Re}_\theta \approx 25000$ is located in the second region of the domain where δ_{99} is still correcting toward a final grow rate. $\mathrm{Re}_\theta \approx 28000$ is located at the start or just inside the third region of the domain. This same observation regarding the development state of the flow can be see when examining the wall-shear-stresses in Fig. 7.10.

The results in Fig. 7.12 and Fig. 7.13 show relatively little difference between each other, but there are a few small differences to be noted. The first difference is seen in the farfield solution. In Fig. 7.13, the simulations without coarsening or limiting have a farfield value that has shifted down and to the positive y^+ direction slightly. This arises due to the SV1 results of Figs. 7.12–7.13 being in a region of increasing τ_w. The other results presented in Figs. 7.12–7.13 are in a region of decreasing τ_w.

The final set of mean-velocity profiles shown in Fig. 7.14 are duplicates of Fig. 7.12 except for the change in scaling. Figure 7.14 is shown with the velocity scaled by u_∞ and the wall-normal distance scaled by δ_{95}. As δ_{95} is only known for the present results and for Österlund's results, the results of Inoue & Pullin are not included for comparison in Fig. 7.14. Additionally, only the $\mathrm{Re}_\theta \approx 25000$ case is considered as a flow scaling such as the one used to create Fig. 7.14 will not be useful when comparing profiles with different Reynolds numbers. Generally speaking, the

results show the same trends as Fig. 7.12 except that the emphasis is now placed near the wall as a result of eliminating the scaling dependence on u_τ. This is especially useful to explore the issue with the PPM results. While Fig. 7.12 shows how the PPM results match experimental results near the wall as a result of τ_w, Fig. 7.14 shows how the PPM results deviate from the experimental results. From Fig. 7.14, it appears that this deviation starts at the beginning of the transition from the outer-flow/wake-region to the log-layer region of the boundary-layer. The exact mechanism for this deviation is unclear, but it is certainly due to the presence of limiting within the boundary-layer. It is perhaps a coincidence, but the very-coarse mesh case with PPM restricts the limiting to the outer region of the flow and obtains results which are of reasonable quality given the resolution, while the coarse mesh case with PPM uses limiting within the log-layer region and obtains results of relatively low quality. It is suggested that further research examine whether restricting limiting away from the log-layer region enhances the quality of simulations using limiting.

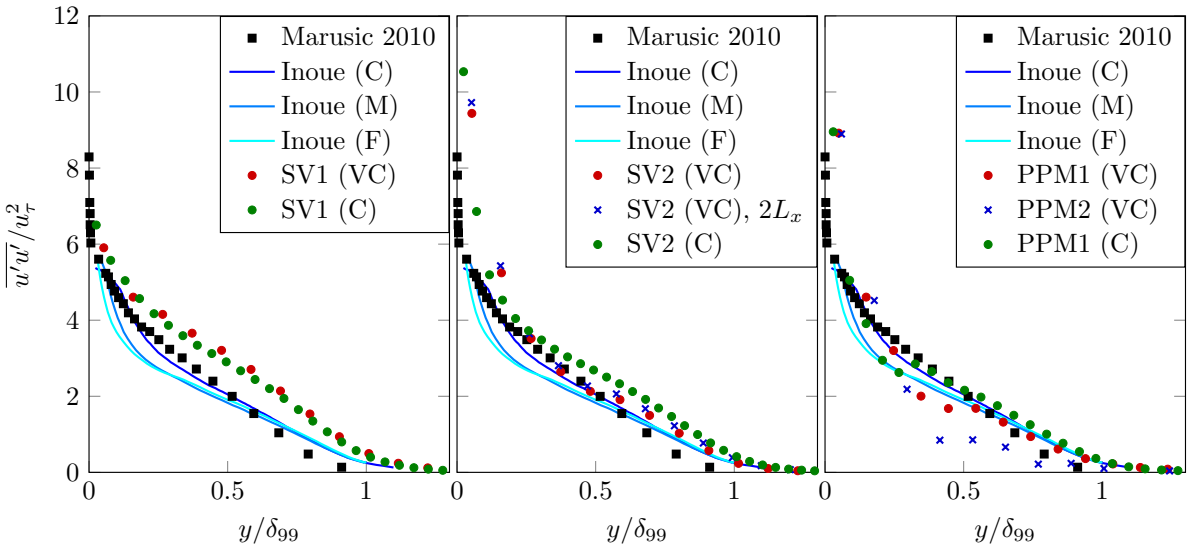

Figure 7.15: Streamwise Reynolds stress, $\overline{u'u'}$, outer-scaled units. $Re_\theta \approx 25000$.

The final set of results displays the streamwise Reynolds stresses, $\overline{u'u'}$ in comparison with data from Inoue & Pullin, Fernholz et al. [102], and Petrie et al. [104]. As the Reynolds stresses are less variable with Reynolds number, Inoue & Pullin were justified in comparing their data at

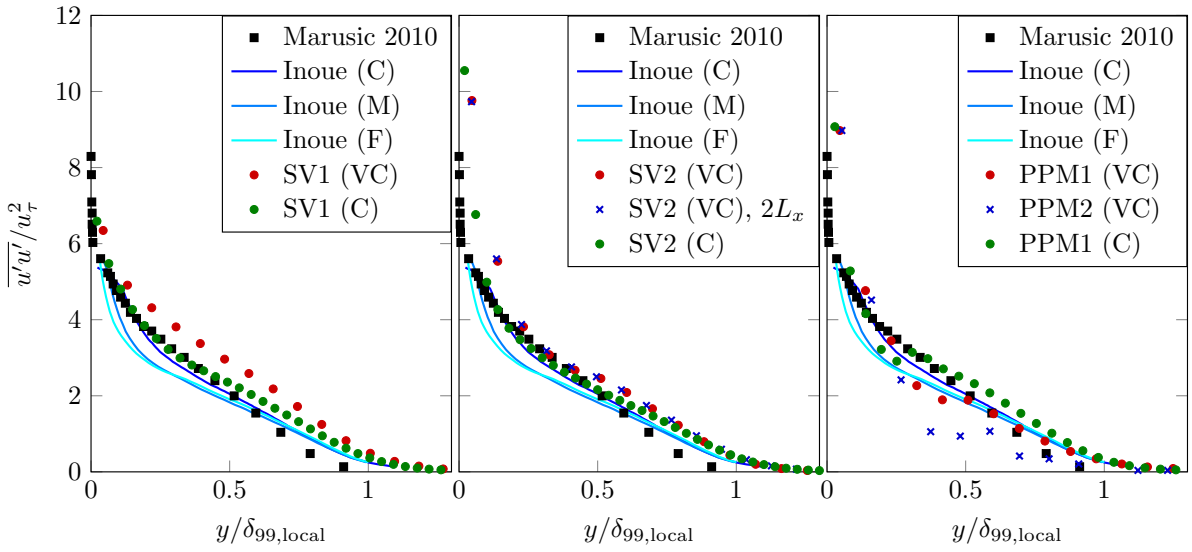

Figure 7.16: Streamwise Reynolds stress, $\overline{u'u'}$, outer-scaled units. $Re_\theta \approx 28000$.

$Re_\theta \approx 25000$ to the data from Marusic et al. [105] at $Re_\theta \approx 20000$. As a result, Fig. 7.15 compares the present results at $Re_\theta \approx 25000$ to Inoue & Pullin's results at the same Reynolds number and to the results presented by Marusic et al. at $Re_\theta \approx 20000$. This figure shows a general trend of the results without coarsening having the highest stresses away from the wall, the results with coarsening having slightly lower stresses away from the wall, but higher stresses near the wall, and the results with coarsening and with PPM having even lower stresses away from the wall and moderately high stresses near the wall. However, as the stresses are slightly more sensitive to the inlet development length than the mean-velocity profiles, it is seen in Fig. 7.16 that comparing the previously described published results (numerical and experimental) with the present results sampled at $Re_\theta \approx 28000$ provides a slightly improved picture of the $\overline{u'u'}$ profiles. The observed decrease in Reynolds stresses in the present results when switching from Fig. 7.15 to Fig. 7.16 is a clear indication that the stresses are still being influenced by inlet-flow non-equilibrium. Based on testing profiles at further locations downstream, $Re_\theta \approx 28000$ is sufficiently far to produce stress profiles that have relatively little impact from inlet-flow non-equilibrium.

From Fig. 7.16, it is observed that an increase in resolution from the very-coarse mesh to the coarse mesh leads to a decrease in $\overline{u'u'}$ in both the simulations without model-coarsening and with

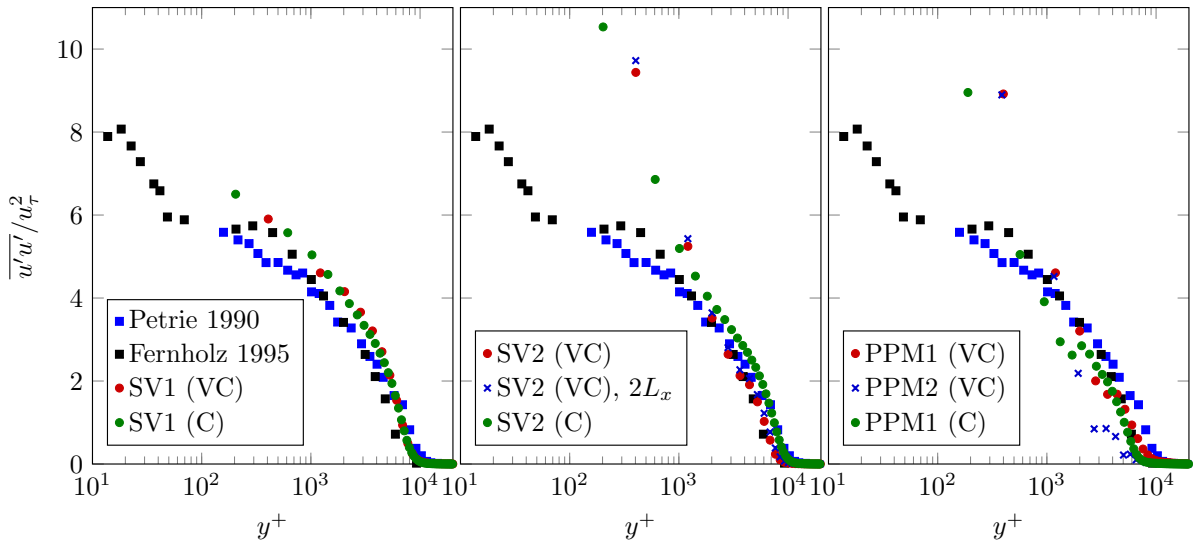

Figure 7.17: Streamwise Reynolds stress, $\overline{u'u'}$, inner-scaled units. $Re_\theta \approx 25000$.

model-coarsening. Furthermore, except for two near-wall cells, $\overline{u'u'}$ increases from the very-coarse mesh to the coarse mesh in the PPM case such that, encouragingly, $\overline{u'u'}$ shows a very similar profile on the coarse mesh in all three algorithms. The near-wall deviation of the stress in the PPM case occurs at the locations where PPM begins to be blended in to the numerical algorithm, suggesting that a slower blending rate may be warranted and that the blending should likely start slightly farther away from the wall as noted in the analysis of the other flow quantities. It is consistently seen in all the current results and in the results of Inoue & Pullin that, higher than $y/\delta_{99,\text{local}} \approx 0.6$ the stresses do not decay as quickly as the experimental results. One issue with experimental determination of turbulent boundary-layer profiles is the issue of determining the boundary-layer thickness. Most experimental results choose boundary-layer thickness variables other than δ_{99} or δ_{95}. As a result, if the scaling values for the experimental data is unclear, it can be difficult to precisely match outer-layer quantities.

Figures 7.17–7.18 compare the stresses with data from Fernholz et al. ($\text{Re}_\theta \approx 20000$) and Petrie et al. ($\text{Re}_\theta \approx 28000$) plotted in inner-scaled units. Although these results do not add significant information beyond the results shown in Figs. 7.16–7.17, a few important pieces of information can be gleaned. First, it is seen in Fig. 7.18 that the outer-layer (sometimes referred to as the

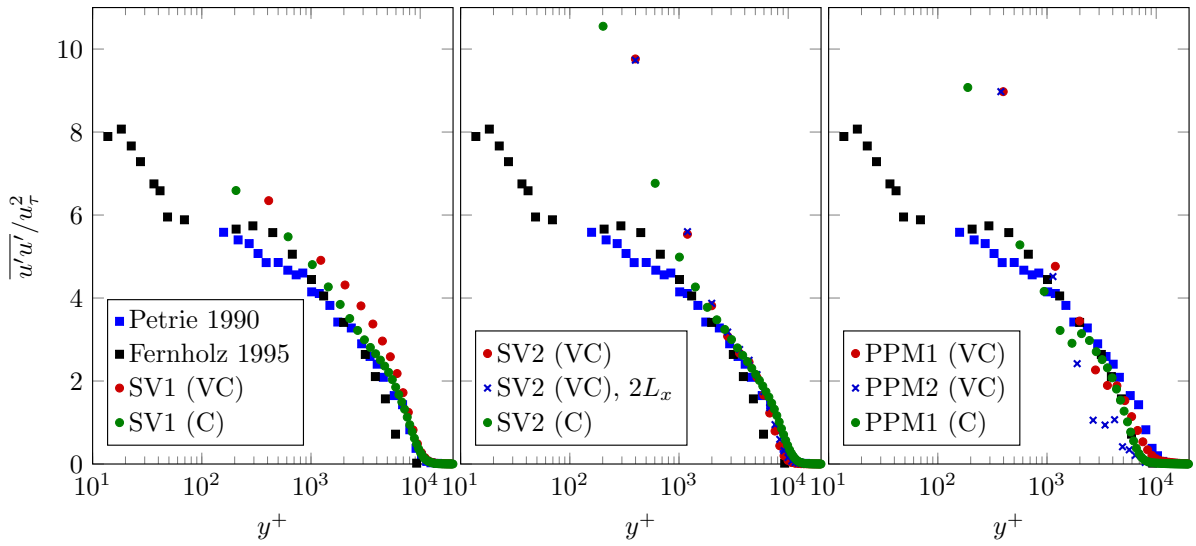

Figure 7.18: Streamwise Reynolds stress, $\overline{u'u'}$, inner-scaled units. $Re_\theta \approx 28000$.

defect-layer) stresses measured by Petrie et al. match the stresses obtained by both the cases using model-coarsening and the cases without model-coarsening. This provides solid evidence that the stretched-vortex model is providing the correct prediction of stresses in the wake-region of the flow. Next is the observation that the near-wall stresses are over-predicted for every simulation tested and are worse with model coarsening. It is unknown whether this is the interaction between the wall-model and the interior stretched-vortex model providing a sense of the unresolved stresses very near the wall or if this is just an artifact of the wall-model.

7.5 Smooth-Ramp Flow-Separation

Results of the smooth-ramp separation case are presented in Figs. 7.19–7.29 in comparison with data presented during the wall-modeled LES section of the 1st AIAA High Fidelity CFD workshop by Larsson and Bermejo-Moreno [106] (these results will be labeled as "UMD-USC" from here on). The UMD-USC results used the wall-model of Kawai & Larsson [107] with a uniform wall-model exchange location at $0.1\delta_0$ away from the wall. One of the main goals of the workshop was for participants using different algorithms to obtain similar results. As DNS-level resolution is currently unachievable for this flow case and there is no known "truth" available,

multiple participating groups with similar results would provide validation through consensus. Unfortunately, this was not the outcome of the workshop, as there was wide variability in results among the 11 groups presenting, and there was no complete agreement on all data between any two groups. The UMD-USC group was one of only two groups showing indications of grid-convergence.

Figures 7.19–7.22 show the time-histories of the separation and reattachment location and time-histories of the streamwise, wall-normal, and spanwise velocities at multiple locations through the domain. Figure 7.23 displays a contour of the mean-streamwise velocity profile demonstrating the zero-valued location associated with the separation bubble. Figures 7.24–7.27 present vertical line probes of the mean velocity profiles and a selection of the Reynolds stresses. This section finishes with Fig. 7.29 displaying the streamwise growth of δ_{95}.

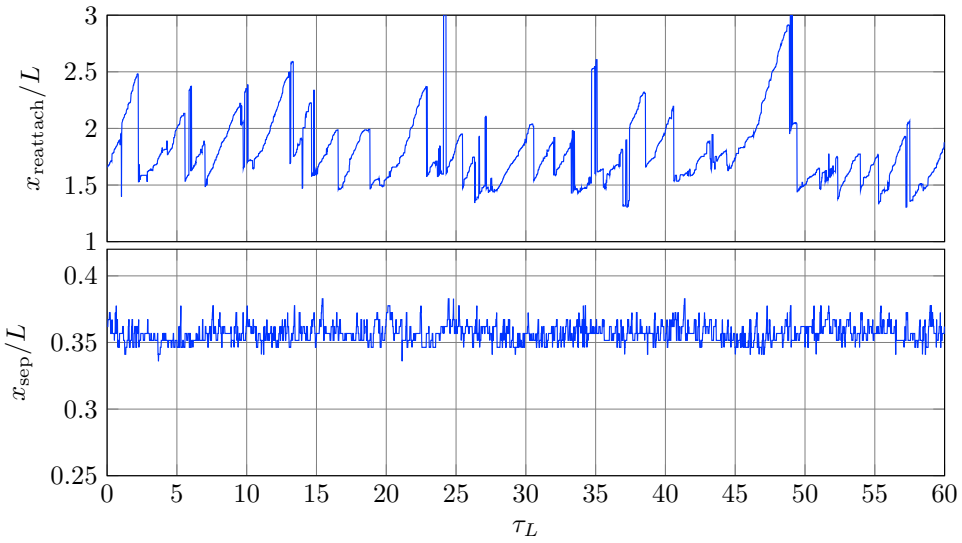

Figure 7.19: Time-histories of separation and reattachment locations for smooth-ramp separation. Separation and reattachment defined, respectively, as the first and last sign-change of the instantaneous spanwise-average of the wall-shear-stress, τ_w.

There are a few observations to be drawn from Fig. 7.19 regarding the separation and reattachment locations. First, the variation of the separation location is rather small in comparison to the ramp length, while the reattachment location shows spatial variations on the order of a ramp-length

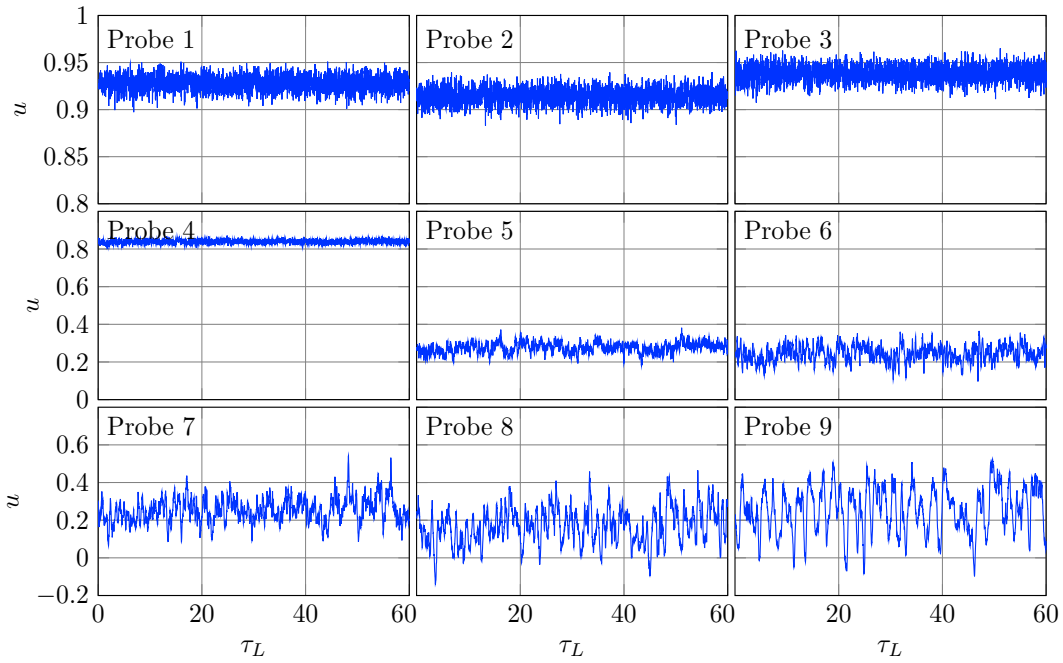

Figure 7.20: Time-histories of spanwise-averaged streamwise velocity from smooth-ramp separation case at 9 probe locations.

even when the simulation is fully temporally-developed. Additionally, these spatial variations in reattachment location are generally biased in time such that the reattachment location will increase with time in a linear fashion and then will suddenly snap back to some earlier location before continuing the same trend. As the separation and reattachment locations are determined by the locations of the first and last change-in-sign of the spanwise-averaged wall-shear-stress, the time history of reattachment is not necessarily showing only a stationary reattachment bubble. In fact, the instantaneous simulation data shows large-scale vortices being shed from the bubble region and convecting downstream. The large deviations in the reattachment location time-history are associated with these large-scale shedding events. The results from most workshop participants are generally in agreement with this observation. In particular, studies from participants suggest that a wider domain would provide a simulation free from large-scale vortex shedding, but as this was not the original objective of the workshop, wider simulations are not performed during the present study.

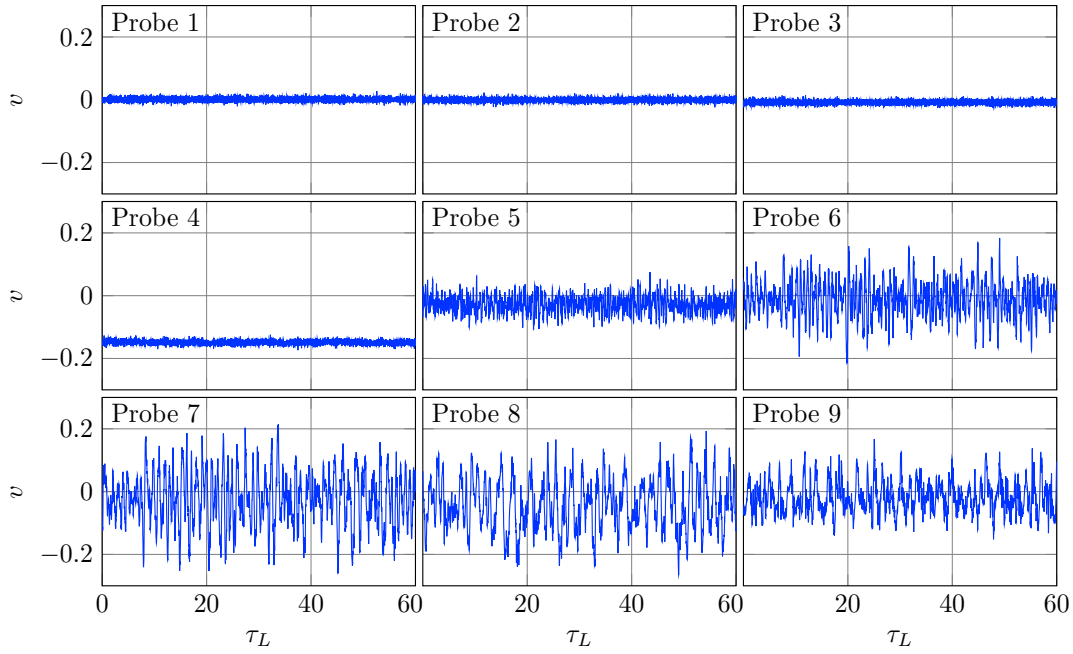

Figure 7.21: Time-histories of spanwise-averaged wall-normal velocity from smooth-ramp separation case at 9 probe locations.

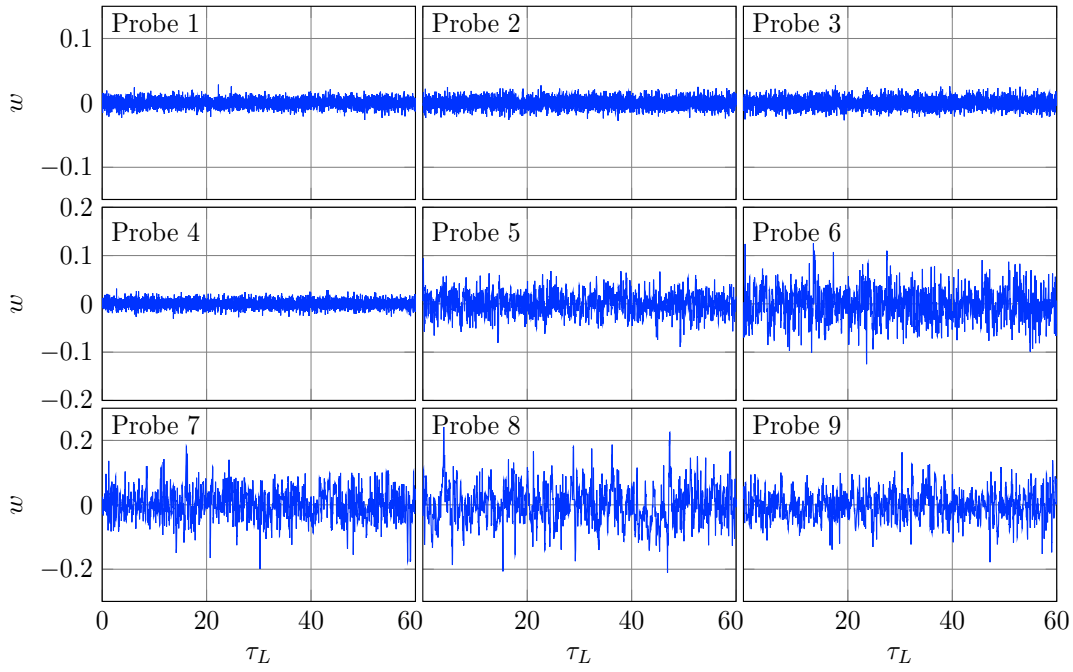

Figure 7.22: Time-histories of spanwise-averaged spanwise velocity from smooth-ramp separation case at 9 probe locations.

All of the velocity time-histories in Figs. 7.20–7.22 show that the velocity components are free of transients at the very beginning of the simulation. This is not surprising given that the simulation was started from a previously developed result. Examining the streamwise velocity data in Fig. 7.20, it is seen that the fluctuations in the flat-plate region of the flow are of relatively similar magnitude before suddenly decreasing in magnitude at Probe 4. As this probe is just prior to the start of the separation region, the increase in negative wall-normal velocity is rapidly shrinking the boundary-layer prior to the start of the ramp and the turbulent fluctuations are decreasing. Considering Probes 5 – 9, it is observed that the separation region introduces larger fluctuations as would be expected. Probes 6 – 9 all show some level of indication of large-scale vortex structures moving past the probe in the same manner as Fig. 7.19. Figures 7.21–7.22 show similar trends of fluctuation magnitudes for v, and w.

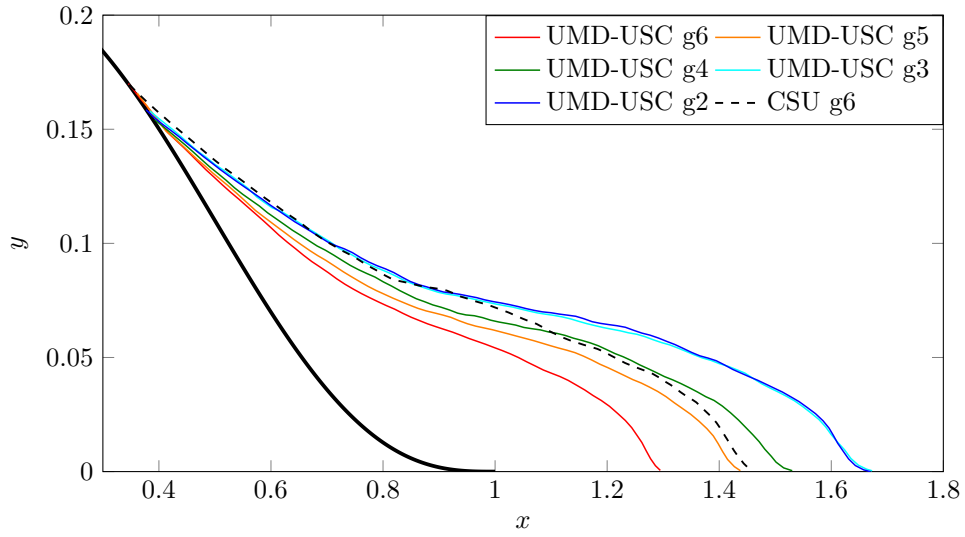

Figure 7.23: Smooth-ramp separation bubble compared with data from the AIAA 2022 WMLES workshop. The separation bubble boundary is identified as the zero-valued contour of the spanwise-averaged and time-averaged streamwise velocity.

Although the results for this case are only obtained for one specific mesh, it is instructive to see how these results compare with those from a different algorithm showing grid-convergence in the majority of quantities analyzed. Figure 7.23 shows the boundary of the separation bubble. This

region of separated, recirculating flow forms as a result of the adverse pressure gradient created by the sudden expansion of the flow over the ramp. This boundary is defined as the zero-valued contour line of the spanwise-averaged and time-averaged streamwise-velocity. The thick black line shown in Fig. 7.23 is the ramp profile. It is encouraging that the results obtained in the current study are generally in agreement with the UMD-USC results. Prior to $x/L = 1$, the current profile starts slightly higher than the UMD-USC results and follows the finest UMD-USC data quite closely. After $x/L = 1$, the current result deviates from the finest UMD-USC profile and agrees quite well with the coarser UMD-USC profiles. As nearly all participants to the workshop noted growing separation bubbles with increasing refinement, it is expected that further refinement of the case performed in this dissertation would lead to a larger separation bubble than that currently shown from grid 6.

Figures 7.24–7.27 show vertical line profiles of data at several sampling locations in the domain. Note that these are not all wall-normal profiles as the profile at $x/L = 0.5$ is in the middle of the ramp (with respect to the streamwise direction). Figure 7.24 shows that the current results for the mean streamwise velocity fall within the range of variation of the UMD-USC results except for a small region below $y/L = 0.035$ at $x/L = 0.5$ and another small region around $y/L = 0.155$. The first deviation of the current results from the UMD-USC range demonstrates a prediction of a stronger recirculation within the separation bubble, while the second deviation is well outside the separation bubble. Similar findings are true for the wall-normal mean-velocity profiles as shown in Fig. 7.25. The results fall within the UMD-USC cases except for a small region near $y/L = 0.02$ at $x/L = 0.5$ and a larger region at $x/L = 1.5$. The difference in the first region is due to the stronger counter flow within the separation bubble, while the difference in the second region is again outside the separation bubble. It is interesting to note that, in both Fig. 7.24 and Fig. 7.25, the current results show near-wall profiles that generally follow the finest UMD-USC results prior to $x/L = 1$. Starting at $x/L = 1$, the current results show agreement with the coarse UMD-USC results. Not surprisingly, this matches the exact same trend exhibited by the separation bubble in Fig. 7.23. Since the wall-normal velocity is largely governed by the expansion of the ramp and the

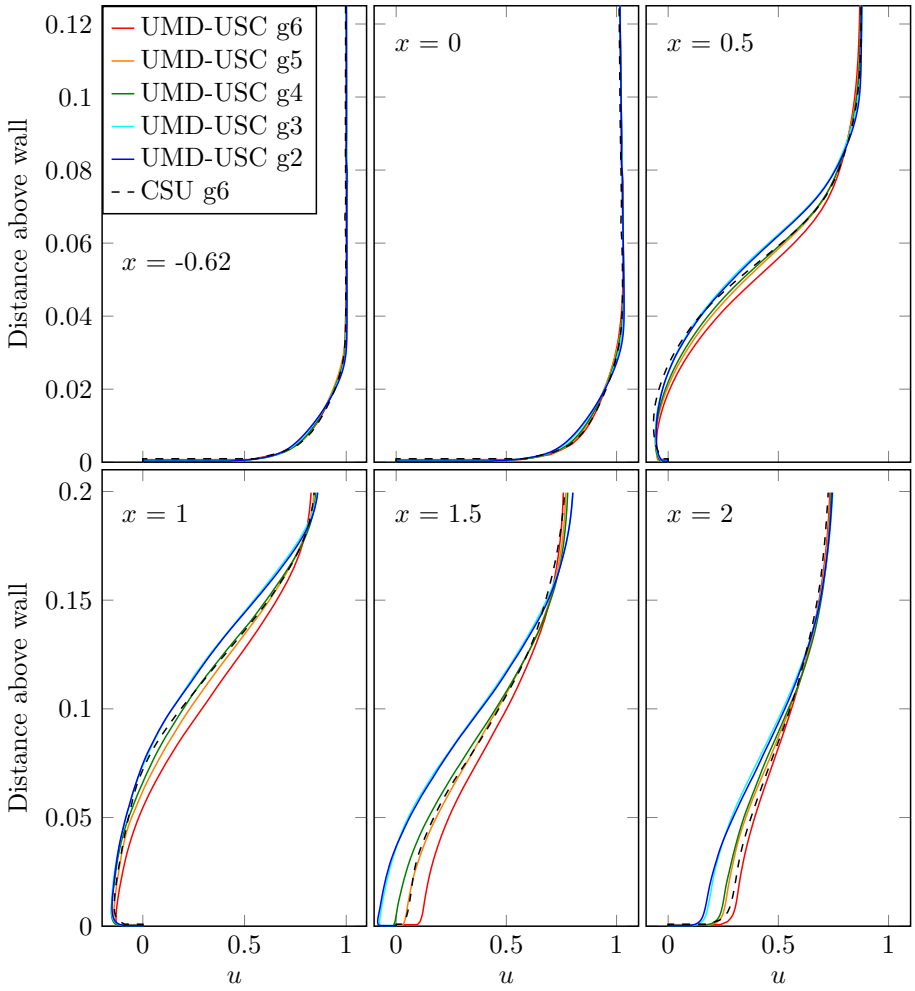

Figure 7.24: Smooth-ramp wall-normal line-probes of streamwise velocity compared with data from the AIAA 2022 WMLES workshop.

overall shape of the separation bubble, the wall-normal velocity and the separation bubble should follow the same trends as one another.

Figure 7.26 and Fig. 7.27 present $\overline{u'u'}$ and $\overline{u'v'}$ respectively. Aside from a slight under-prediction of $\overline{u'u'}$ near the wall in the flat-plate region and a few other notable exceptions just above the separation bubble, both $\overline{u'u'}$ and $\overline{u'v'}$ fall within the variability of the coarse-to-fine-mesh range of the UMD-USC results. Examining the under-prediction of $\overline{u'u'}$ in the flat-plate region, it is theorized that the adverse pressure gradient induced by the smooth-ramp may be already changing the behavior of the near-wall solution upstream of the separation point more than

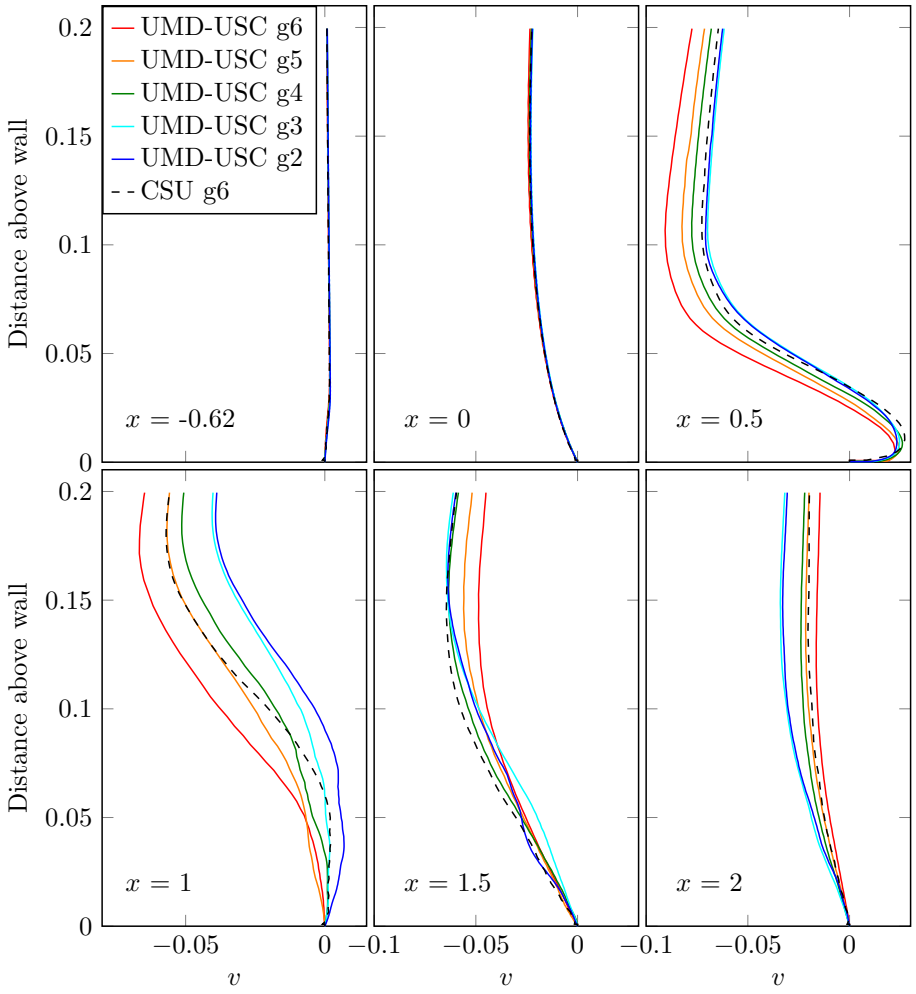

Figure 7.25: Smooth-ramp wall-normal line-probes of wall-normal velocity compared with data from the AIAA 2022 WMLES workshop.

in the UMD-USC results. The other notable difference between the two datasets is the overprediction of $\overline{u'u'}$ within a shear-layer starting very close to the beginning of the separation zone and spreading in the wall-normal direction as it convects downstream. This over-prediction is clearly seen around $y/L = 0.13$ at $x/L = 1$, $y/L = 0.05$ at $x/L = 1.5$, and $y/L = 0.02$ at $x/L = 2$, along with an over-prediction of the $\overline{u'v'}$ magnitude seen around $y/L = 0.125$ at $x/L = 1$ and $y/L = 0.06$ at $x/L = 1.5$. An additional over-prediction of $\overline{u'u'}$ is seen near the wall at $x/L = 1$. While an exact mechanism for these over-predictions of $\overline{u'u'}$ and $\overline{u'v'}$ is not known, future studies should determine whether or not these originate with the upstream boundary-layer and also which

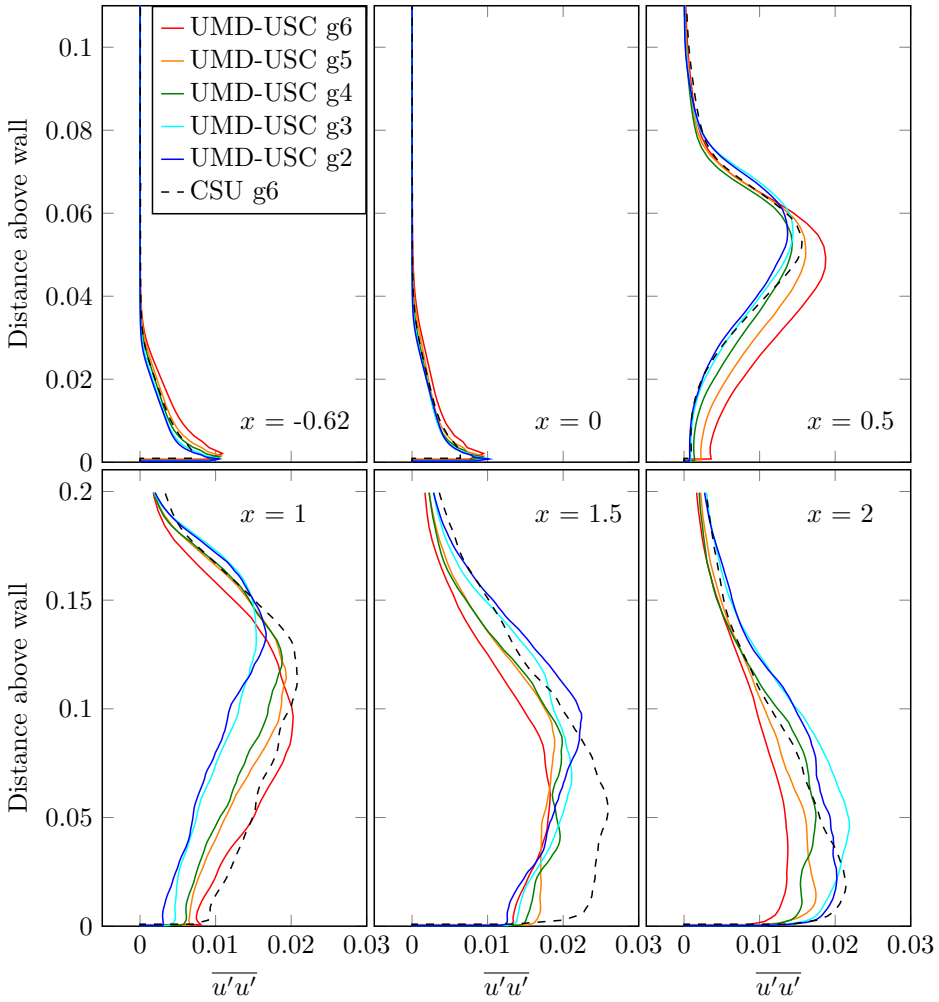

Figure 7.26: Smooth-ramp wall-normal line-probes of $\overline{u'u'}$ compared with data from the AIAA 2022 WM-LES workshop.

simulation is correct (the UMD-USC results or the current results) as the true value is not known. Further refinement would elucidate the differences between the datasets.

Figure 7.28 displays the time-averaged, spanwise-averaged wall shear-stress, τ_w, provided by the wall-model for the current results. Prior to the separation region, τ_w is seen to follow the same shape as the UMD-USC results, but at a slightly lower value. The initial bump in τ_w is due to the inlet development region of the recycled turbulence and the inlet boundary condition. Given the rather coarse resolution in the boundary-layer of the flat-plate region, it is expected that the prediction of τ_w in this region of the domain will change with increased refinement. Following

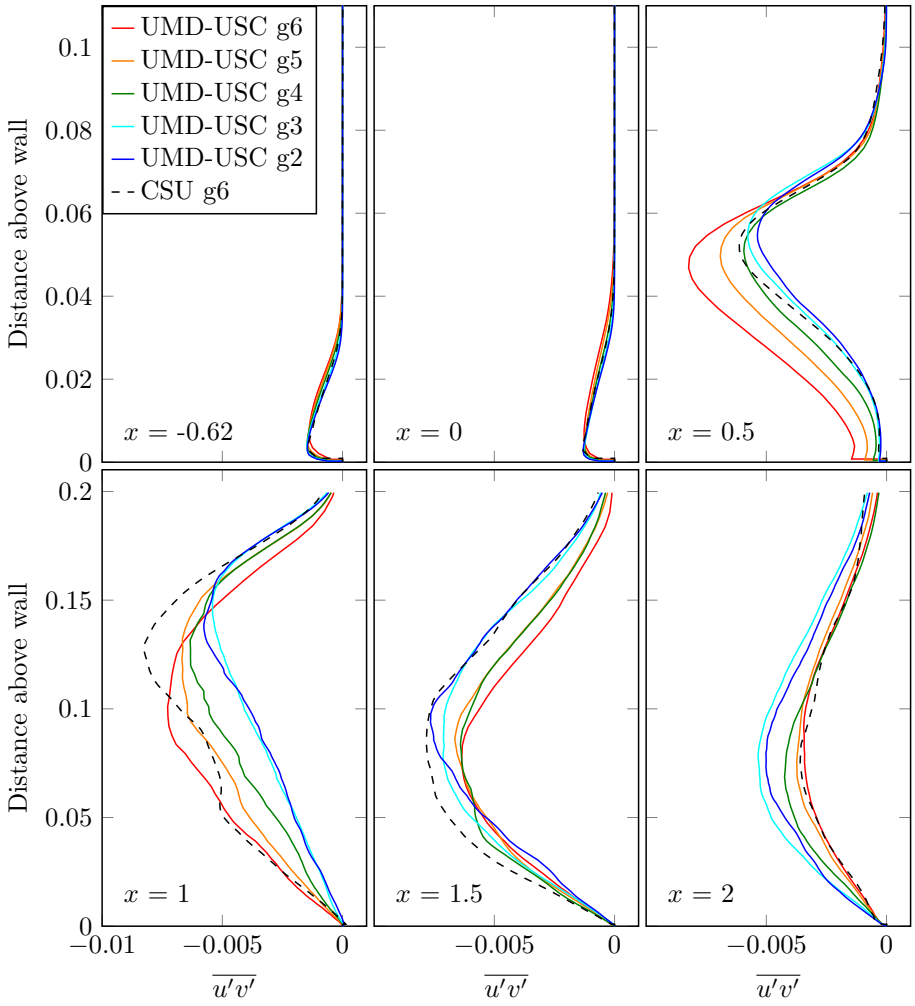

Figure 7.27: Smooth-ramp wall-normal line-probes of $\overline{u'v'}$ compared with data from the AIAA 2022 WMLES workshop.

separation, τ_w from the current case generally agrees with the UMD-USC results up until the AMR boundary is reached, after which point, τ_w is severely under-predicted due to lack of mesh resolution.

Finally, Fig. 7.29 displays δ_{95} for the present results. The simulation was ran with an inlet $\delta_{99} = 0.014$ in order to reach the target δ_{99} in the flat-plate domain and, when the smooth-ramp was added, the boundary-layer shrunk slightly. This is not surprising as the separation region creates a negative (toward the wall) wall-normal velocity that is felt by the boundary-layer at some distance upstream of the beginning of the ramp. This negative wall-normal velocity impedes the

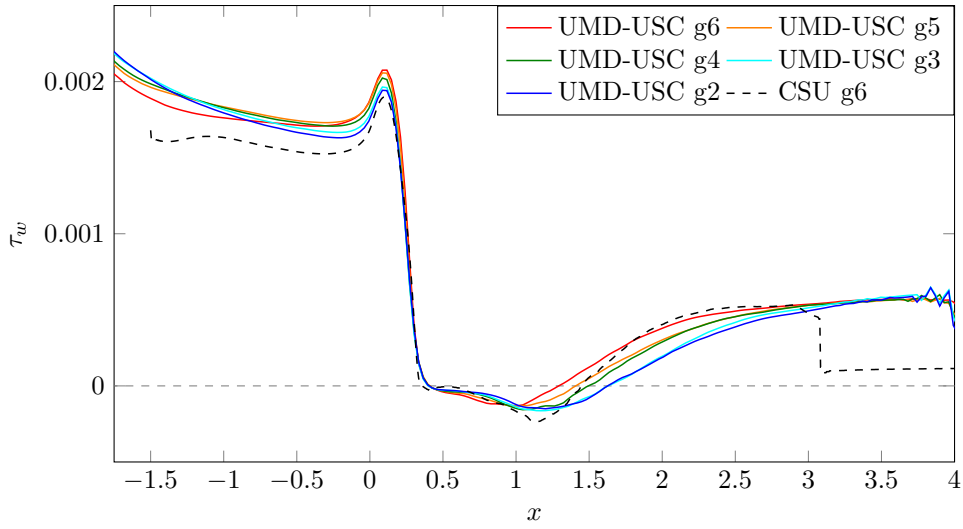

Figure 7.28: Smooth-ramp wall-shear-stress compared with data from the AIAA 2022 WMLES workshop.

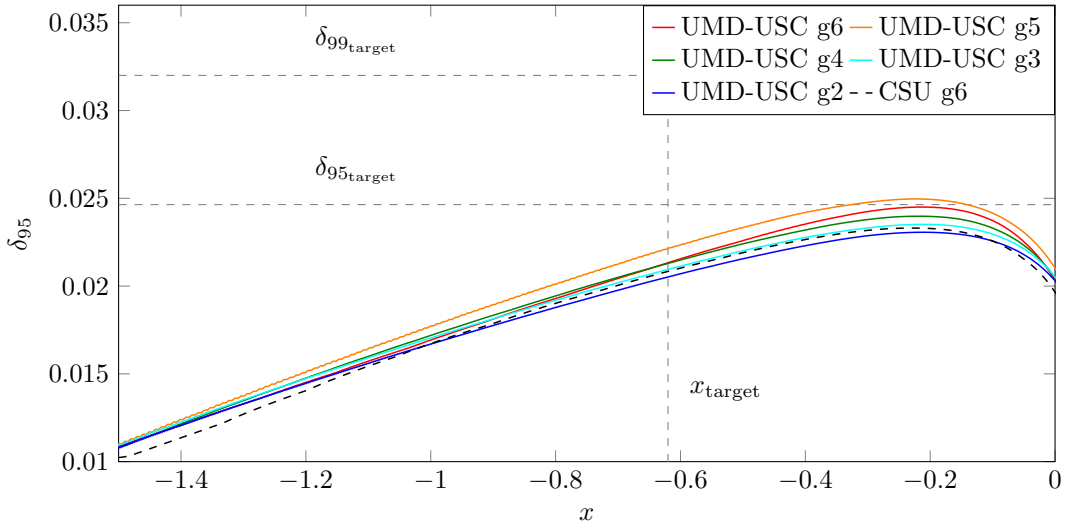

Figure 7.29: Smooth-ramp 95% boundary-layer thickness, δ_{95}, growth rate compared with data from the AIAA 2022 WMLES workshop.

growth of the boundary-layer slightly and causes the target δ_{99} and δ_{95} not to be reached in the smooth-ramp simulation. However, it is seen in Fig. 7.29 that the boundary-layer develops at a similar rate as the UMD-USC results, confirming that the boundary-layer thickness growth rate is well developed prior to reaching the target location.

Chapter 8

Conclusions

8.1 Conclusions

In conclusion, the present study describes the mathematical foundations of LES and a novel coupling of the stretched-vortex model with algorithmic components such as numerical regularization that are a necessary component of general-purpose compressible CFD solvers. The results from this coupling method conclusively demonstrate that scheme and grid-independent LES solutions of high-Reynolds number flows are obtainable for unbounded turbulent flows when the turbulence model is appropriately isolated from any numerical regularization used in the numerical algorithm. For wall-bounded turbulent flows, less conclusive evidence was obtained regarding coupling the LES models and algorithmic components to obtain grid-independent and scheme-independent results. However, it was demonstrated that the wall-model and the stretched-vortex model presented in this dissertation were able to reproduce numerical and experimental results for the canonical zero-pressure-gradient flat-plate turbulent boundary-layer at very coarse resolutions. Predictions of separated flows are within the uncertainty of the community consensus and demonstrate quality results on extremely coarse grids. Guidance was provided for future investigations into adequately coupling the wall-model with numerical regularization methods. Overall, the stretched-vortex model is shown to be a promising SGS and wall model for general-purpose compressible CFD solvers operating on coarse grids at high Reynolds numbers.

8.2 Original Contributions

Original contributions provided by the final study improve the simulation of turbulent flows using the stretched-vortex LES model with high-order finite volume methods. These original contributions include:

1. implementation of the stretched-vortex LES model and the stretched-vortex wall-model within a large-scale CFD code infrastructure featuring fourth-order finite volume methods and mapped, multiblock grids with adaptive mesh refinement;

2. extension of the slip-wall type, stretched-vortex subgrid-scale wall-model to account for compressible flow physics;

3. integration of the stretched-vortex model with numerical regularization in a unique, coarsened computation framework which effectively links the various components of the algorithm as a whole and provides scheme-independent and grid-independent LES simulation results;

4. demonstration of the interaction between the interior stretched-vortex model, the wall-model and numerical regularization in the context of wall-bounded turbulent flows.

8.3 Future Work

This dissertation establishes the base LES capability in support of studies pushing toward accurately simulating unresolved, reacting turbulent flows of engineering and scientific interest. As such, future studies will require the SVS model to be coupled with reaction-turbulence interaction models to improve the physical fidelity of these simulations. Optimal strategies for integrating the wall-model with limiters are yet to be proposed. Considerations of the stability of shock-boundary-layer interactions appear necessary since this work indicates that limiters must be disengaged near the wall for accuracy, at least at coarse resolutions. Finally, improvements to the numerical boundary conditions, the addition of moving geometries and embedded-boundary meshes, as well as the addition of further physics models will provide a means by which the fourth-order finite volume algorithm, Chord, can simulate a wide range of problems encountered in engineering design.

Bibliography

[1] J. Slotnick, A. Khodadoust, J. Alonso, D. Darmofal, W. Gropp, E. Lurie, and D. Mavriplis, "CFD vision 2030 study: A path to revolutionary computational aerosciences," Tech. Rep. 218178, NASA/CR, 2014. https://ntrs.nasa.gov/citations/20140003093.

[2] A. Cary, J. Chawner, E. Duque, W. Gropp, B. Kleb, R. Kolonay, E. Nielsen, and B. Smith, "The CFD vision 2030 roadmap: 2020 status, progress and challenges," tech. rep., cfd2030.com, 2020. http://cfd2030.com/report.html.

[3] T. Mauery, J. Alonso, A. Cary, V. Lee, R. Malecki, D. Mavriplis, G. Medic, J. Schaefer, and J. Slotnick, "A guide for aircraft certification by analysis: Establishing a 20-year vision for virtual flight and engine testing," Tech. Rep. 20210015404, NASA/CR, 2021. https://ntrs.nasa.gov/citations/20210015404.

[4] A. N. Kolmogorov, "The local structure of turbulence in incompressible viscous fluid for very large Reynolds numbers," *Dokl. Akad. Nauk SSSR*, vol. 30, no. 4, pp. 299–303, 1941.

[5] O. Reynolds, "On the dynamical theory of incompressible viscous fluids and the determination of the criterion," *Philosophical Transactions of the Royal Society of London*, vol. 186, pp. 123–164, 1895.

[6] A. S. C. A. C. Subcommittee, "The opportunities and challenges of exascale computing," tech. rep., DOE, 2010.

[7] S. B. Pope, "Ten questions concerning the large-eddy simulation of turbulent flows," *New Journal of Physics*, vol. 6, pp. 1–24, 2004.

[8] P. A. T. Cocks, M. Soteriou, and V. Sankaran, "Impact of numerics on the predictive capabilities of reacting flow LES," *Combust. and Flame*, vol. 162, pp. 3394–3411, 2015.

[9] Z. J. Wang, K. Fidkowski, R. Abgrall, F. Bassi, D. Caraeni, A. Cary, H. Deconinck, R. Hartmann, K. Hillewaert, H. T. Huynh, N. Kroll, G. May, P.-O. Persson, B. van Leer, and M. Visbal, "High-order CFD methods: current status and perspective," *Int. J. Numer. Methods Fluids*, vol. 72, no. 8, pp. 811–845, 2013.

[10] S. Walters, X. Gao, H. Johansen, and S. Guzik, "Assessing stretched-vortex subgrid-scale models in finite volume methods for unbounded turbulent flows," *Flow Turb. Comb.*, 2020.

[11] P. Sagaut, *Large Eddy Simulation for Incompressible Flows: An Introduction*. Springer-Verlag, 3rd ed., 1998.

[12] F. F. Grinstein, L. G. Margolin, and W. J. Rider, *Implicit Large Eddy Simulation: Computing Turbulent Fluid Dynamics*. Cambridge University Press, 1st ed., 2007.

[13] M. Karaca, N. Lardjane, and I. Fedioun, "Implicit Large Eddy Simulation of high-speed non-reacting and reacting air/H_2 jets with a 5th order WENO scheme," *Comput. Fluids*, vol. 62, pp. 25–44, 2012.

[14] P. Fernandez, N. C. Nguyen, and J. Peraire, "The hybridized discontinuous Galerkin method for implicit Large-Eddy Simulation of transitional turbulent flows," *J. Comput. Phys.*, vol. 336, pp. 308–329, 2017.

[15] R. C. Moura, G. Mengaldo, J. Peiro, and S. J. Sherwin, "On the eddy-resolving capability of high-order discontinuous Galerkin approaches to implicit LES/under-resolved DNS of Euler turbulence," *J. Comput. Phys.*, vol. 330, pp. 615–623, 2017.

[16] C. Carton de Wiart, K. Hillewaert, L. Bricteux, and G. Winckelmans, "Implicit LES of free and wall-bounded turbulent flows based on the discontinous Galerkin/symmetric interior penalty method," *Int. J. Numer. Method. Fluids*, vol. 78, pp. 335–354, 2015.

[17] S. Walters, S. Guzik, and X. Gao, "Evaluation of the stretched-vortex subgrid-scale model for large-eddy simulation with a fourth-order finite volume algorithm," in *2019 AIAA SciTech Forum*, no. AIAA 2019-1886. https://doi.org/10.2514/6.2019-1886.

[18] S. Walters, X. Gao, and S. Guzik, "Large-eddy simulations of wall-bounded flows using high-order finite volume methods with adaptive mesh refinement," in *2020 AIAA SciTech Forum*, 2020.

[19] S. M. Murman, L. T. Diosady, A. Garai, and M. Ceze, "A space-time discontinuous-Galerkin approach for separated flows," in *54th AIAA Aerospace Sciences Meeting*, no. 2016-1059, AIAA SciTech Forum, 2016.

[20] E. Garnier, N. Adams, and P. Sagaut, *Large Eddy Simulation for Compressible Flows*. Springer-Verlag, 1st ed., 2009.

[21] P. Sagaut, *Large Eddy Simulation for Incompressible Flows: An Introduction*. Springer, 3rd ed., 2005.

[22] L. C. Evans, *Partial Differential Equations*. American Mathematical Society, 2nd ed., 2015.

[23] M. Germano, "Differential filters for the large eddy numerical simulation of turbulent flows," *Phys. Fluids*, vol. 29, pp. 1755–1756, June 1986.

[24] C. D. Pruett, T. B. Gatski, C. E. Grosch, and W. D. Thacker, "The temporally filtered Navier-Stokes equations: Properties of the residual stress," *Phys. Fluids*, vol. 15, no. 8, pp. 2127–2140, 2003.

[25] C. G. Speziale, "Invariance of turbulent closure models," *Phys. Fluids*, vol. 22, pp. 1033–1037, June 1979.

[26] C. G. Speziale, "Galilean invariance of subgrid-scale stress models in the large-eddy simulation of turbulence," *J. Fluid Mech.*, vol. 156, pp. 55–62, 1985.

[27] C. G. Speziale, "Second-order closure models for rotating turbulent flows," ICASE NASA-CR-178005, Institute for Computer Applications in Science and Engineering, 1985.

[28] C. G. Speziale, "Subgrid scale stress models for the large-eddy simulation of rotating turbulent flows," *Geophys. Astrophys. Fluid Dynamics*, vol. 33, pp. 199–222, 1985.

[29] R. A. Clark, J. H. Ferziger, and W. C. Reynolds, "Evaluation of subgrid-scale turbulence models using a fully simulated turbulent flow," Technical Report NASA-CR-152642, NASA, March 1977.

[30] S. T. Bose, P. Moin, and D. You, "Grid-independent large-eddy simulation using explicit filtering," *Phys. Fluids*, vol. 22, no. 10, 2010. https://doi.org/10.1063/1.3485774.

[31] S. T. Bose, P. Moin, and F. Ham, "Explicitly filtered large eddy simulation on unstructured grids," annual research briefs 2011, Center for Turbulence Research, 2011.

[32] Y. Dakhoul and K. Bedford, "Improved averaging method for turbulent flow simulation. part i: Theoretical development and application to Burgers transport equation," *International Journal for Numerical Methods in Fluids 6.2*, pp. 49–64, 1986.

[33] Y. Dakhoul and K. Bedford, "Improved averaging method for turbulent flow simulation. part II: Calculations and verification," *International Journal for Numerical Methods in Fluids 6.2*, pp. 65–82, 1986.

[34] A. A. Aldama and D. R. F. Harleman, "The approximation of nonlinearities in the filtered Navier-Stokes equations," *Adv. Water Resources*, vol. 14, pp. 15–30, July 1991.

[35] D. Carati and A. Wray, "Time filtering in large-eddy simulations," in *Proceedings for the Summer Program*, pp. 263–270, Center for Turbulence Research, 2000.

[36] J. Duan, P. Fischer, T. Iliescu, and T. M. Özgökmen, "Bridging the Boussinesq and primitive equations through spatio-temporal filtering," *Applied Mathematics Letters*, vol. 23, pp. 453–456, 2010.

[37] S. Walters, S. Guzik, and X. Gao, "Favre-averaged spatiotemporal-filtered large eddy simulation," in *2018 AIAA Aerospace Sciences Meeting*, no. AIAA 2018-0373, AIAA SciTech Forum, 2018. https://doi.org/10.2514/6.2018-0373.

[38] C. D. Pruett, "Eulerian time-domain filtering for spatial LES," in *Recent Advances in DNS and LES: Proceedings of the Second AFOSR Conference held at Rutgers*, AFOSR, 1999.

[39] C. D. Pruett, "Eulerian time-domain filtering for spatial large-eddy simulation," *AIAA Journal*, vol. 38, pp. 1634–1642, September 2000.

[40] C. D. Pruett, "Toward the de-mystification of LES," in *DNS/LES Progress and Challenges. Proceedings of the Third AFOSR International Conference on DNS/LES*, AFOSR, 2001.

[41] C. D. Pruett, B. C. Thomas, C. E. Grosch, and T. B. Gatski, "A temporal approximate deconvolution model for large-eddy simulation," *Phys. Fluids*, vol. 18, no. 2, p. 028104, 2006.

[42] A. Favre, "Turbulence: Space-time statistical properties and behavior in supersonice flows," *Phys. Fluids*, vol. 26, pp. 2851–2863, Oct. 1983.

[43] J. D. Jackson and B. Launder, "Osborne Reynolds and the publication of his papers on turbulent flow," *Annu. Rev. Fluid Mech.*, vol. 39, pp. 19–35, January 2007.

[44] T. S. Lundgren, "Strained spiral vortex model for turbulent fine structure," *Phys. Fluids*, vol. 25, pp. 2193–2203, December 1982.

[45] D. I. Pullin and P. G. Saffman, "Vortex dynamics in turbulence," *Annu. Rev. Fluid Mech.*, vol. 30, pp. 31–51, 1998.

[46] D. I. Pullin and P. G. Saffman, "On the Lundgren-Townsend model of turbulent fine scales," *Phys. Fluids*, vol. 5, pp. 126–145, January 1993.

[47] D. I. Pullin and P. G. Saffman, "Reynolds stresses and one-dimensional spectra for a vortex model of homogeneous anisotropic turbulence," *Phys. Fluids*, vol. 6, pp. 1787–1796, May 1994.

[48] D. I. Pullin, J. D. Buntine, and P. G. Saffman, "On the spectrum of a stretched spiral vortex," *Phys. Fluids*, vol. 6, pp. 3010–3027, September 1994.

[49] P. G. Saffman and D. I. Pullin, "Anisotropy of the Lundgren-Townsend model of fine-scale turbulence," *Phys. Fluids*, vol. 6, pp. 802–807, February 1994.

[50] A. Misra and D. I. Pullin, "A vortex-based subgrid stress model for large-eddy simulation," *Phys. Fluids*, vol. 9, pp. 2443–2454, August 1997.

[51] T. Voelkl, D. I. Pullin, and D. C. Chan, "A physical-space version of the stretched-vortex subgrid-stress model for large-eddy simulation," *Phys. Fluids*, vol. 12, pp. 1810–1825, July 2000.

[52] T. W. Mattner, "A refined stretched-vortex model for large-eddy simulation of turbulent mixing layers," in *17th Australasian Fluid Mechanics Conference*, December 2010.

[53] D. Chung and D. I. Pullin, "Large-eddy simulation and wall modelling of turbulent channel flow," *J. Fluid Mech.*, vol. 631, pp. 281–309, 2009.

[54] D. Chung and D. I. Pullin, "Direct numerical simulation and large-eddy simulation of stationary buoyancy-driven turbulence," *J. Fluid Mech.*, vol. 643, pp. 279–308, 2010.

[55] T. W. Mattner, "Large-eddy simulations of turbulent mixing layers using the stretched vortex model," *J. Fluid Mech.*, vol. 671, pp. 507–534, 2011.

[56] P. E. Hamlington, J. Schumacher, and W. J. A. Dahm, "Direct assessment of vorticity alignment with local and nonlocal strain rates in turbulent flows," *Phys. Fluids*, vol. 20, p. 111703, 2008.

[57] V. Mugundhan, R. S. Pugazenthi, N. B. Speirs, R. Samtaney, and S. T. Thoroddsen, "The alignment of vortical structures in turbulent flow through a contraction," *J. Fluid Mech.*, vol. 884, p. A5, 2020.

[58] D. A. Shetty and S. H. Frankel, "Assessment of stretched vortex subgrid-scale models for LES of incompressible inhomogeneous turbulent flows," *Int. J. Numer. Meth. Fluids*, vol. 73, pp. 152–171, 2013.

[59] D. I. Pullin, "A vortex-based model for the subgrid flux of a passive scalar," *Phys. Fluids*, vol. 12, pp. 2311–2319, September 2000.

[60] D. I. Pullin and T. S. Lundgren, "Axial motion and scalar transport in stretched spiral vortices," *Phys. Fluids*, vol. 13, pp. 2553–2563, September 2001.

[61] B. Kosovic, D. I. Pullin, and R. Samtaney, "Subgrid-scale modeling for large-eddy simulations of compressible turbulence," *Phys. Fluids*, vol. 14, pp. 1511–1522, April 2002.

[62] D. J. Hill, C. Pantano, and D. I. Pullin, "Large-eddy simulation and multi-scale modelling of a Richtmyer-Meshkov instability with reshock," *J. Fluid Mech.*, vol. 557, pp. 29–61, 2006.

[63] M. Lombardini, D. J. Hill, D. I. Pullin, and D. I. Meiron, "Atwood ratio dependence of Richtmyer-Meshkov flows under reshock conditions using large-eddy simulations," *J. Fluid Mech.*, vol. 670, pp. 439–480, 2011.

[64] A. J. Musker, "Explicit expression for the smooth wall velocity distribution in a turbulent boundary layer," *AIAA Journal*, vol. 17, no. 6, pp. 656–657, 1979.

[65] S. T. Bose and P. Moin, "A dynamic slip boundary condition for wall-modeled large-eddy simulation," *Phys. Fluids*, vol. 26, p. 015104, 2014. https://doi.org/10.1063/1.4849535.

[66] H. J. Bae, A. Lozano-Durán, S. T. Bose, and P. Moin, "Dynamic slip wall model for large-eddy simulation," *J. Fluid Mech.*, vol. 859, pp. 400–432, 2019. https://doi.org/10.1017/jfm.2018.838.

[67] S. T. Bose and G. I. Park, "Wall-modeled large-eddy simulation for complex turbulent flows," *Annu. Rev. Fluid Mech.*, vol. 50, pp. 535–561, 2018.

[68] M. Inoue and D. I. Pullin, "Large-eddy simulation of the zero-pressure-gradient turbulent boundary layer up to $Re_\theta = \mathcal{O}(10^{12})$," *J. Fluid Mech.*, vol. 686, pp. 507–533, 2011.

[69] B. T. McCann, *A Wall Model for Large-Eddy Simulation of Compressible Channel Flows*. Ph.D. dissertation, University of Washington, 2014.

[70] W. Cheng, D. I. Pullin, and R. Samtaney, "Large-eddy simulation of separation and reattachment of a flat plate turbulent boundary layer," *J. Fluid Mech.*, vol. 785, pp. 78–108, 2015.

[71] D. B. Spalding, "A single formula for the "law of the wall"," *J. Appl. Mech.*, vol. 28, no. 3, pp. 455–458, 1961. https://doi.org/10.1115/1.3641728.

[72] X. Gao, S. M. J. Guzik, and P. Colella, "Fourth order boundary treatment for viscous fluxes on Cartesian grid finite-volume methods," in *52nd AIAA Aerospace Sciences Meeting*, no. 2014-1277, 2014.

[73] S. M. Guzik, X. Gao, L. D. Owen, P. McCorquodale, and P. Colella, "A freestream-preserving fourth-order finite-volume method in mapped coordinates with adaptive-mesh refinement," *Comput. Fluids*, vol. 123, pp. 202–217, 2015.

[74] S. M. Guzik, X. Gao, and C. Olschanowsky, "A high-performance finite-volume algorithm for solving partial differential equations governing compressible viscous flows on structured grids," *Comput. Math Appl.*, vol. 72, pp. 2098–2118, 2016.

[75] X. Gao, L. D. Owen, and S. M. J. Guzik, "A parallel adaptive numerical method with generalized curvilinear coordinate transformation for compressible Navier-Stokes equations," *Int. J. Numer. Meth. Fluids*, vol. 82, pp. 664–688, 2016.

[76] L. D. Owen, S. M. Guzik, and X. Gao, "A high-order adaptive algorithm for multispecies gaseous flows on mapped domains," *Comput. Fluids*, vol. 170, pp. 249 – 260, 2018.

[77] P. Colella, D. T. Graves, N. Keen, T. J. Ligocki, D. F. Martin, P. McCorquodale, D. Modiano, P. Schwartz, T. Sternberg, and B. V. Straalen, *Chombo Software Package for AMR Applications - Design Document*. Lawrence Berkeley National Laboratory, 2009. `https://seesar.lbl.gov/anag/chombo/ChomboDesign-3.0.pdf`.

[78] P. Colella and M. Sekora, "A limiter for PPM that preserves accuracy at smooth extrema," *J. Comput. Phys.*, vol. 227, no. 15, pp. 7069–7076, 2008.

[79] P. McCorquodale and P. Colella, "A high-order finite-volume method for conservation laws on locally refined grids," *Comm. App. Math. Comput. Sci.*, vol. 6, no. 1, pp. 1–25, 2011.

[80] C. Chaplin and P. Colella, "A single-stage flux-corrected transport algorithm for high-order finite-volume methods," *Comm. App. Math. Comput. Sci.*, vol. 12, pp. 1–24, May 2017.

[81] P. Colella and P. R. Woodward, "The piecewise parabolic method PPM for gas-dynamical simulations," *J. Comput. Phys.*, vol. 54, pp. 174–201, 1984.

[82] D. Chung and G. Matheou, "Large-eddy simulation of stratified turbulence. part i: A vortex-based subgrid-scale model," *Journal of the Atmospheric Sciences*, vol. 71, pp. 1863–1879, May 2014.

[83] T. Colonius, "Modeling artificial boundary conditions for compressible flow," *Annu. Rev. Fluid Mech.*, vol. 36, pp. 315–345, 2004.

[84] T. Poinsot and S. Lele, "Boundary conditions for direct simulations of compressible viscous flow," *J. Comput. Phys.*, vol. 101, no. 1, pp. 104–129, 1992.

[85] G. Lodato, P. Domingo, and L. Vervisch, "Three-dimensional boundary conditions for direct and large-eddy simulation of compressible viscous flows," *J. Comput. Phys.*, vol. 227, pp. 5105–5143, 2008.

[86] E. Motheau, A. Almgren, and J. B. Bell, "Navier-Stokes characteristic boundary conditions using ghost cells," *AIAA Journal*, vol. 55, no. 10, pp. 3399–3408, 2017.

[87] C. Pantano and S. Sarkar, "A study of compressibility effect in the high-speed turbulent shear layer using direct simulation," *J. Fluid Mech.*, vol. 451, pp. 329–371, 2002.

[88] T. L. Jackson and C. E. Grosch, "Absolute/convective instabilities and the convective Mach number in a compressible mixing layer," tech. rep., NASA, 1989.

[89] J. R. Bull and A. Jameson, "Simulation of the compressible Taylor Green vortex using high-order flux reconstruction schemes," in *7th AIAA Theoretical Fluid Mechanics Conference*, no. AIAA 2014-3210, AIAA Aviation Forum, 2014.

[90] G. Comte-Bellot and S. Corrsin, "Simple Eulerian time correlation of full and narrow-band velocity signals in grid-generated, 'isotropic' turbulence," *J. Fluid Mech.*, vol. 48, pp. 273–337, 1971.

[91] J. Larsson, R. Baurle, C. Brehm, D. Garmann, I. Bermejo-Moreno, M. Galbraith, D. Gonzalez, and D. Rizzetta, "Large eddy simulation workshop on smooth-body separation." Accessed online, January 2022. https://wmles.umd.edu/workshop-2021/.

[92] T. Skeledzic, J. Krauss, H. Lienhart, Ö. Ertunc, and J. Jovanovic, "Characterization of turbulence generated by an active grid with individually controllable paddles," in *New Results in Numerical and Experimental Fluid Mechanics XI*, (Cham), pp. 105–114, Springer International Publishing, 2018.

[93] R. J. Hearst and P. Lavoie, "The effect of active grid initial conditions on high Reynolds number turbulence," *Experiments in Fluids*, vol. 56, p. 185, Sep 2015.

[94] W. Rozema, H. J. Bae, P. Moin, and R. Verstappen, "Minimum-dissipation models for large-eddy simulation," *Phys. Fluids*, vol. 27, p. 085107, 2015.

[95] H. S. Kang, S. Chester, and C. Meneveau, "Decaying turbulence in an active-grid-generated flow and comparisons with large-eddy simulation," *J. Fluid Mech.*, vol. 480, pp. 129–160, 2003.

[96] T. S. Lund, S. Wu, and K. D. Squires, "Generation of turbulent inflow data for spatially-developing boundary layer simulations," *J. Comput. Phys.*, vol. 140, pp. 233–258, 1998.

[97] X. Wu, "Inflow turbulence generation methods," *Annu. Rev. Fluid Mech.*, vol. 49, pp. 23–49, 2017.

[98] G. Urbin and D. Knight, "Large-eddy simulation of a supersonic boundary layer using an unstructured grid," *AIAA Journal*, vol. 39, pp. 1288–1295, July 2001.

[99] Y. A. Çengel and J. M. Cimbala, *Fluid Mechanics: Fundamentals and Applications*. McGraw-Hill, 1st ed., 2006.

[100] C. Wenzel, B. Selent, M. Kloker, and U. Rist, "DNS of compressible turbulent boundary layers and assessment of data/scaling-law quality," *J. Fluid Mech.*, vol. 842, pp. 428–468, 2018.

[101] J. M. Österlund, *Experimental studies of zero pressure-gradient turbulent boundary layer flow*. Ph.D. dissertation, KTH, 1999.

[102] H. H. Fernholz, E. Krause, M. Nockemann, and M. Schober, "Comparative measurements in the canonical boundary layer at $\mathrm{Re}_{\delta_2} \leq 6x10^4$ on the wall of the German-Dutch windtunnel," *Phys. Fluids*, vol. 7, pp. 1275–1281, 1995.

[103] X. I. A. Yang, G. I. Park, and P. Moin, "Log-layer mismatch and modeling of the fluctuating wall stress in wall-modeled large-eddy simulations," *Phys. Rev. Fluids*, vol. 2, p. 104601, 2017.

[104] H. L. Petrie, A. A. Fontaine, S. T. Sommer, and T. A. Brungart, "Large flat plate turbulent boundary layer evaluation," Tech. Rep. 89-207, Penn State Applied Research Laboratory, 1990.

[105] I. Marusic, R. Mathis, and N. Hutchins, "Predictive model for wall-bounded turbulent flow," *Science*, vol. 329, p. 5988, 2010.

[106] J. Larsson and I. Bermejo-Moreno. personal communication, Jan. 2022.

[107] S. Kawai and J. Larsson, "Wall-modeling in large eddy simulation: Length scales, grid resolution, and accuracy," *Phys. Fluids*, vol. 24, p. 015105, 2012.

[108] C. Rosales and C. Meneveau, "Linear forcing in numerical simulations of isotropic turbulence: Physical space implementations and convergence properties," *Phys. Fluids*, vol. 17, p. 095106, 2005.

[109] A. Garai, L. T. Diosady, N. K. Madavan, and S. M. Murman, "DNS of low-pressure turbine cascade flows with elevated inflow turbulence using a discontinuous-Galerkin spectral-element method," in *Proceedings of ASME Turbo Expo 2016: Turbomachinery Technical Conference and Exposition*, ASME, June 2016.

[110] M. R. Petersen and D. Livescu, "Forcing for statistically stationary compressible isotropic turbulence," *Phys. Fluids*, vol. 22, p. 116101, 2010.

[111] R. A. Clark, J. H. Ferziger, and W. C. Reynolds, "Evaluation of subgrid-scale models using an accurately simulated turbulent flow," *J . Fluid Mech.*, vol. 91, pp. 1–16, 1979.

[112] L. G. Margolin, "Finite-scale equations for compressible fluid flow," *Phil. Trans. R. Soc. A*, vol. 367, pp. 2861–2871, 2009.

Appendix A

Additional Equations

From the conservation equations, other useful equations are easily derived. These equations include the time-evolution of velocity,

$$\frac{\partial u_i}{\partial t} + u_j \frac{\partial u_i}{\partial x_j} + \frac{1}{\rho}\frac{\partial p}{\partial x_i} - \frac{1}{\rho}\frac{\partial \tau_{ij}}{\partial x_j} = f_i \,, \tag{A.1}$$

time-evolution of kinetic energy, ($k = \rho u_i u_i/2$),

$$\frac{\partial k}{\partial t} + \frac{\partial}{\partial x_j}\left(k u_j + p u_j\right) - p\frac{\partial u_j}{\partial x_j} - u_i \frac{\partial \tau_{ij}}{\partial x_j} = f_i u_i \,, \tag{A.2}$$

time-evolution of dilitational velocity (divergence of velocity),

$$\frac{\partial}{\partial t}\left(\frac{\partial u_i}{\partial x_i}\right) + \frac{\partial}{\partial x_i}\left(u_j \frac{\partial u_i}{\partial x_j}\right) - \frac{1}{\rho^2}\left(\frac{\partial \rho}{\partial x_i}\right)\left[\frac{\partial p}{\partial x_i} - \frac{\partial \tau_{ij}}{\partial x_j}\right] + \frac{1}{\rho}\frac{\partial}{\partial x_i}\left[\frac{\partial p}{\partial x_i} - \frac{\partial \tau_{ij}}{\partial x_j}\right] = \frac{\partial f_i}{\partial x_i} \,, \tag{A.3}$$

time-evolution of vorticity, ω,

$$\frac{\partial \omega_p}{\partial t} + \epsilon_{pqi}\frac{\partial \epsilon_{ijk}\omega_j u_k}{\partial x_q} - \frac{\epsilon_{pqi}}{\rho^2}\left(\frac{\partial \rho}{\partial x_q}\right)\left[\frac{\partial p}{\partial x_i} - \frac{\partial \tau_{ij}}{\partial x_j}\right] - \frac{\epsilon_{pqi}}{\rho}\frac{\partial^2 \tau_{ij}}{\partial x_q \partial x_j} = \epsilon_{pqi}\frac{\partial f_i}{\partial x_q} \,, \tag{A.4}$$

and time-evolution of velocity gradient,

$$\frac{\partial}{\partial t}\left(\frac{\partial u_i}{\partial x_k}\right) + \frac{\partial}{\partial x_k}\left(u_j \frac{\partial u_i}{\partial x_j}\right) + \frac{\partial}{\partial x_k}\left(\frac{1}{\rho}\frac{\partial p}{\partial x_i}\right) - \frac{\partial}{\partial x_k}\left(\frac{1}{\rho}\frac{\partial \tau_{ij}}{\partial x_j}\right) = \frac{\partial f_i}{\partial x_j} \,. \tag{A.5}$$

Appendix B

Artificially Forced Turbulence

B.1 Turbulence Forcing Motivation

Simulations of artificially forced turbulence provide a tool for assessing the quality of turbulence models and numerical methods used for simulating turbulent flows. Various quantities such as kinetic energy, energy dissipation, and acoustic energy can be specified and targeted using forcing methods. The methods presented here are designed to maintain constant resolved kinetic energy over time while assuming a stationary mean flow. To achieve this, a forcing term is added to the momentum equations, while it is assumed that the forcing term for internal energy exactly balances the forcing term for kinetic energy. As a result, the total energy remains unchanged. A simple interpretation of this type of forcing is that as viscosity dissipates kinetic energy into internal energy, the forcing term removes this internal energy and dumps it back into kinetic energy. The result is that total energy is conserved, kinetic energy is approximately conserved, and momentum is not necessarily conserved (obviously, momentum conservation is maintained only for source terms which can be written in divergence form).

B.2 Kinetic Energy Forcing

Considering a forcing term for the momentum equations, most studies begin with a forcing term of the form

$$f_i = B\rho u_i \tag{B.1}$$

where B is a constant throughout the spatial domain and a variable with respect to time and is given by [108–110]

$$B = \frac{\text{PD} + \epsilon}{\rho u_i u_i}. \tag{B.2}$$

Using this form of B, the kinetic energy equation shown above will reach a steady-state value in the long-term. The constant, B, is computed using a domain averaged kinetic energy for the denominator and a specified turbulent dissipation rate in the numerator. Pressure dilatation is assumed to be small or is lumped in with the turbulent dissipation term.

One issue with this method of forcing involves the acoustic energy level in the turbulence simulation. Over long time periods, the acoustic energy in the simulation can grow to an unacceptably large level [110]. While various acoustic control mechanisms have been developed [110], most of these methods still retain the form of the forcing term shown above. During the course of the current research, a different forcing method was developed in order to prevent the development of acoustic energy.

B.3 Divergence-Free Forcing Term

The basic idea behind this forcing term is that a forcing term which is guaranteed to be divergence-free will not force the dilatational velocity as shown in Eq. (A.3). A simple start to a divergence-free source-term begins with a momentum equation source term using the curl of momentum instead of velocity

$$f_i = B\epsilon_{ijk}\frac{\partial \rho u_k}{\partial x_j} \tag{B.3}$$

where, to reach a constant kinetic energy value, B becomes

$$B = \frac{\text{PD} + \epsilon}{u_i \epsilon_{ijk}\frac{\partial \rho u_k}{\partial x_j}}. \tag{B.4}$$

A similar approach is taken as compared with the velocity forcing in that a domain averaged helicity, $u_i\epsilon_{ijk}\frac{\partial \rho u_k}{\partial x_j}$, is computed while the pressure dilatation and turbulent dissipation rate are specified.

B.4 Results

Results of the two forcing types are presented below. As already mentioned, researchers implementing the velocity forcing in compressible solvers report that kinetic energy tends to transfer from rotational, turbulent modes to dilatational, acoustic modes over time [110]. While some researchers have noted that this trend continues in an unbounded fashion for hundreds of characteristic times, others have seen the acoustic field reach a steady-state saturation level. Even a steady-state level of acoustic energy is, if not sufficiently low, undesirable for cases necessitating very low acoustic energy levels.

On the other hand, the tendency of the divergence-free forcing is to prevent acoustic energy generation from the source term, resulting in a very quiet flow field. However, the vorticity forcing does display an initial peak in enstrophy and kinetic energy that is higher than the initial spike shown by velocity forcing. This feature arises as a result of the vorticity forcing method creating a non-zero domain-summed helicity value. A period of time is required before the simulation reaches an equilibrium state and during this initial period of time, the forcing creates an overshoot in the enstrophy and kinetic energy.

The divergence-free forcing shows the most stable domain-summed quantities of any forcing method the author has seen throughout the literature covering forced compressible flows. It is seen in Figs. B.1–B.6 that the domain-averaged quantities show very few deviations from the overall mean value specified in the simulation. Whether or not this is useful remains to be seen. Future researchers may be interested in testing this method if they choose to use forced turbulence as a test case.

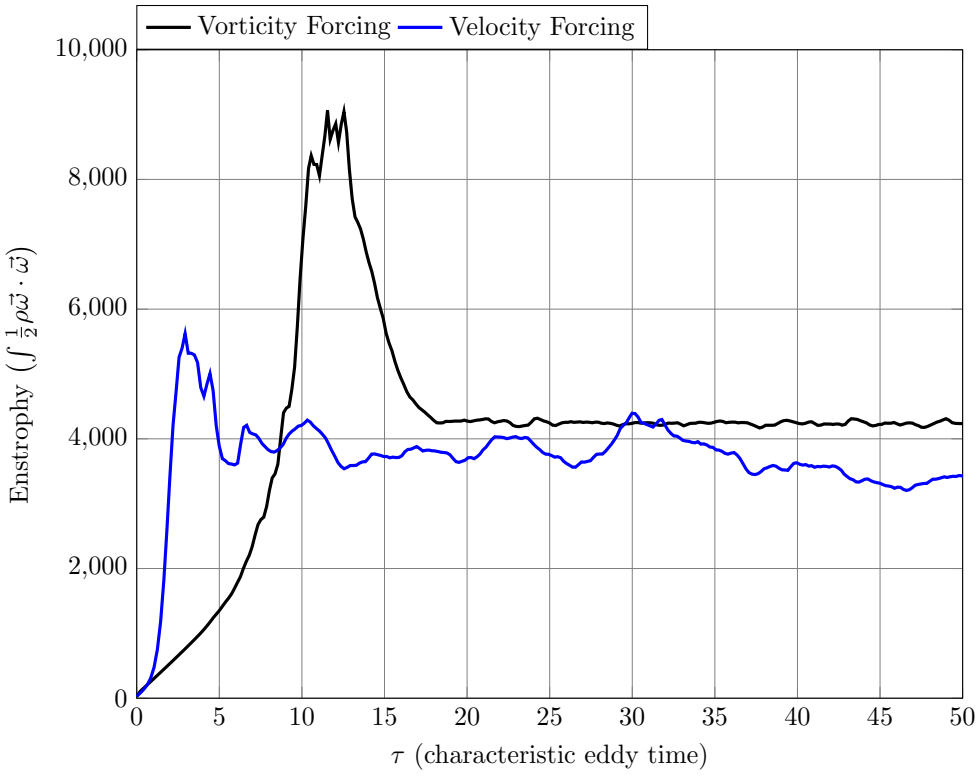

Figure B.1: Enstrophy over time: Mach 0.1

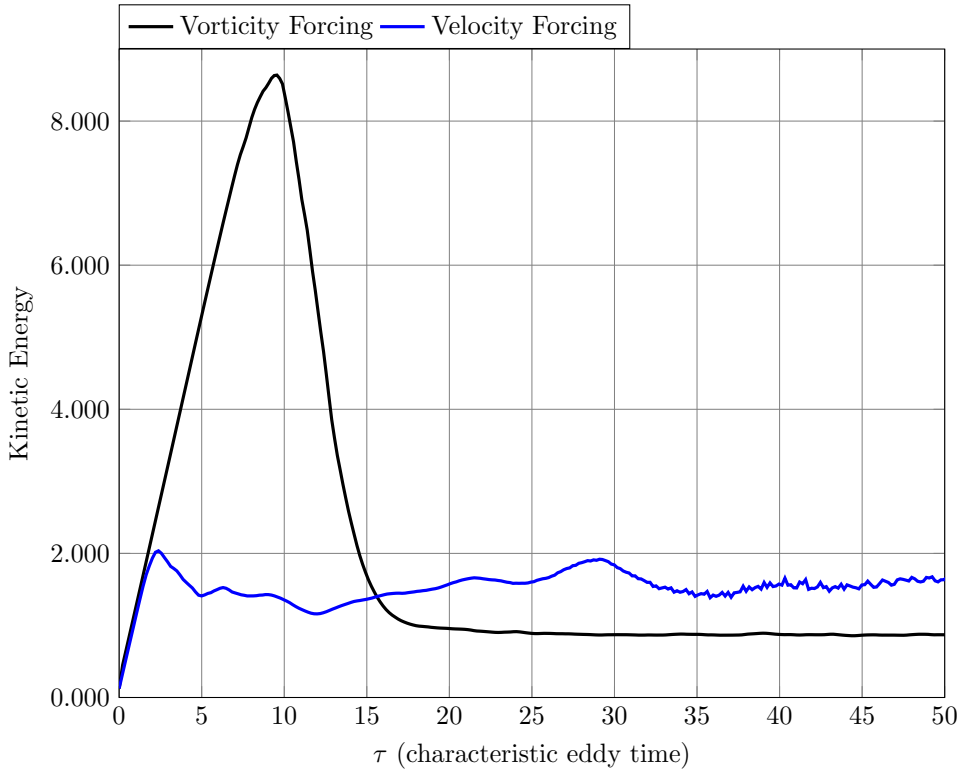

Figure B.2: Kinetic energy over time: Mach 0.1

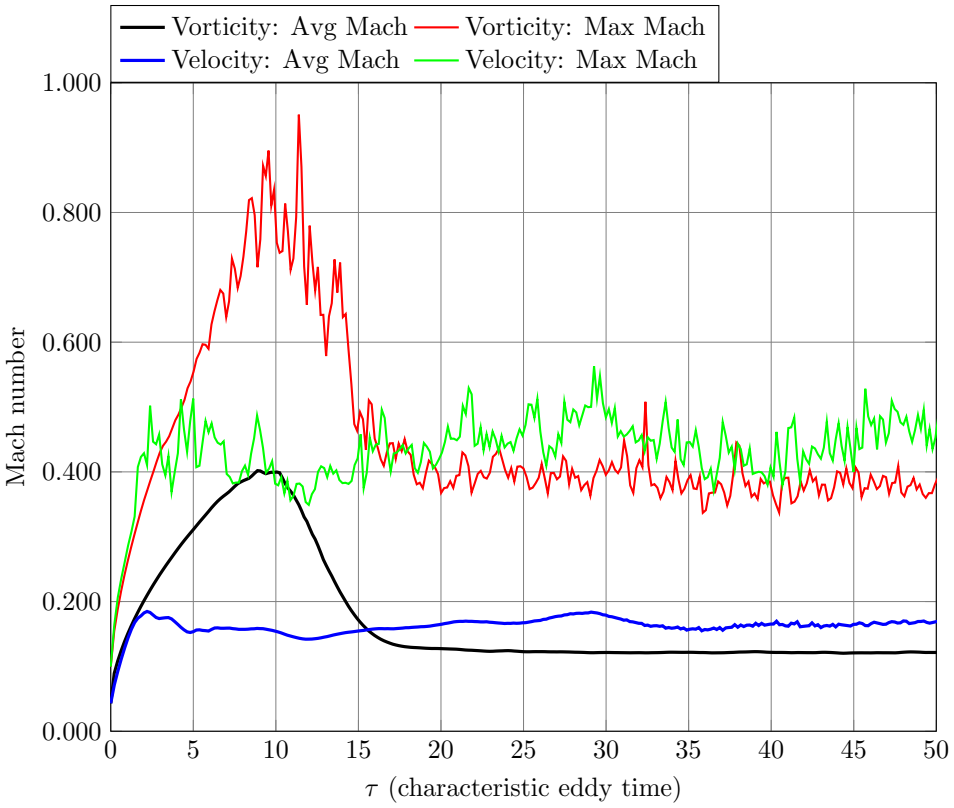

Figure B.3: Mach number over time: Mach 0.1

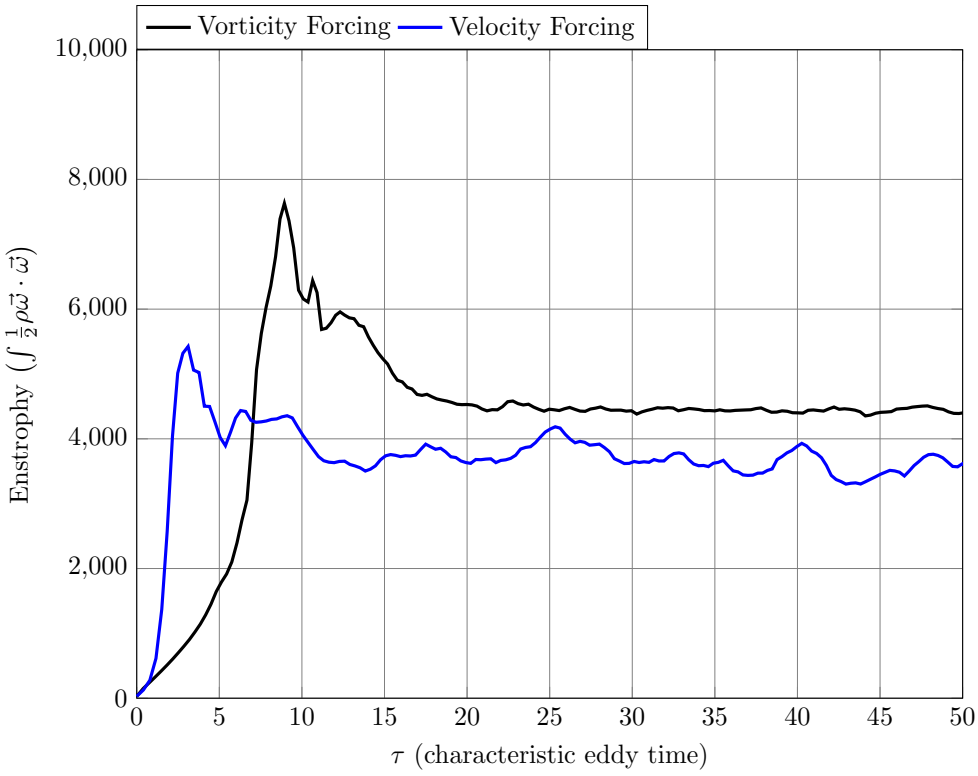

Figure B.4: Enstrophy over time: Mach 0.2

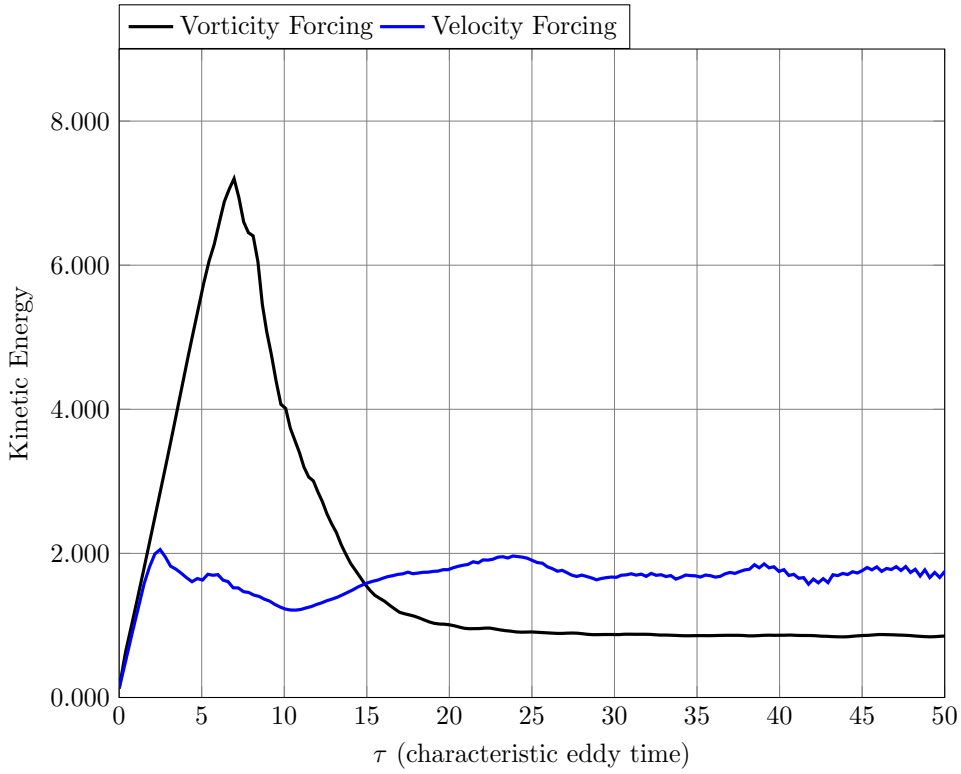

Figure B.5: Kinetic energy over time: Mach 0.2

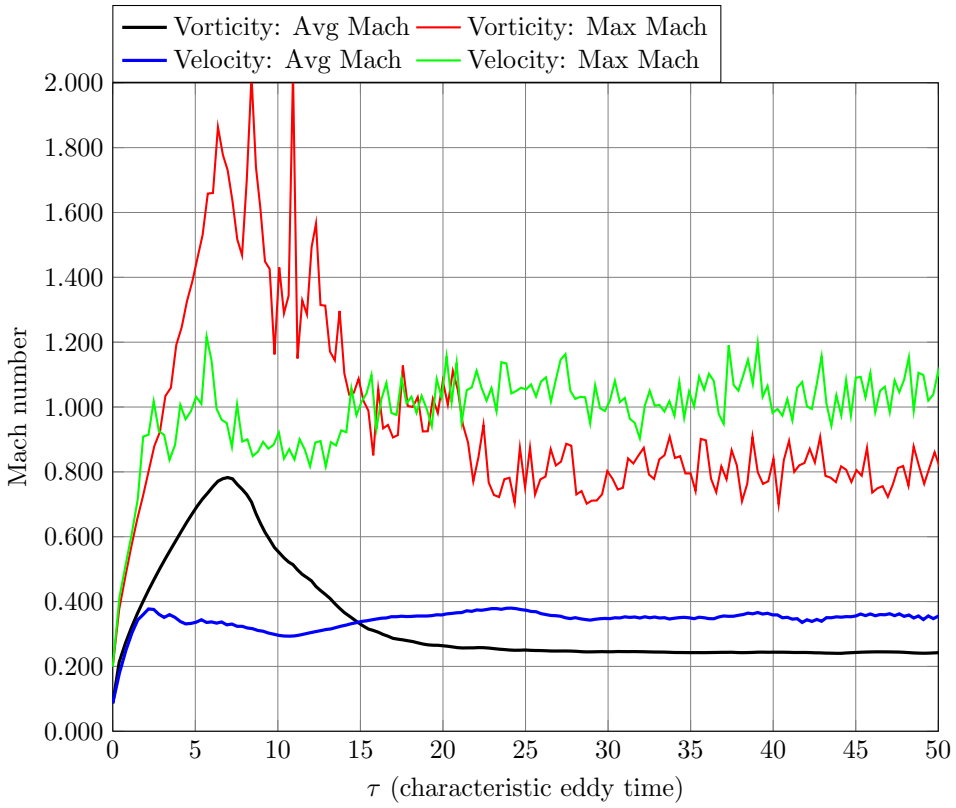

Figure B.6: Mach number over time: Mach 0.2

Appendix C

Additional Orientation Model Development

An additional stretched-vortex orientation model [17], derived during the course of this dissertation by the author and based on an observed similarity between the vortex-orientation model and the viscous stress-tensor, begins with the definition of the eigenvectors of the strain-rate tensor $\tilde{\tilde{\tilde{S}}}$

$$\tilde{S}_{ij}e_j = \lambda e_i \ , \tag{C.1}$$

where λ is an eigenvalue of $\tilde{\tilde{\tilde{S}}}$ and $\vec{e}$ is an eigenvector of $\tilde{\tilde{\tilde{S}}}$. Using Eq. (C.1) and noting $\tilde{\tilde{\tilde{S}}}$ is symmetric, Eq. (4.8) can be rewritten as

$$\delta_{ij} - \frac{1}{\lambda^2}\tilde{S}_{il}e_l e_k \tilde{S}_{kj} = \delta_{ij} - e_i e_j \ . \tag{C.2}$$

Multiplying by λ^2, rearranging slightly, and inserting into Eq. (4.2), a result is obtained that appears similar to the molecular stress tensor given in Eq. 3.5

$$(\widetilde{u_i u_j} - \tilde{u}_i \tilde{u}_j) = -\frac{K}{\lambda^2}\left(\tilde{S}_{il}e_l e_k \tilde{S}_{kj} - \lambda^2 \delta_{ij}\right) \ . \tag{C.3}$$

While this is not entirely surprising, it does give rise to some further observations. The identity matrix in the molecular stress tensor is multiplied by the divergence of velocity which is equivalent to the trace of the strain-rate tensor

$$\tilde{S}_{ii} = \frac{\partial \tilde{u}_i}{\partial x_i} \ . \tag{C.4}$$

It is also known that $\tilde{S}_{ii}$ is equal to the sum of the eigenvalues of the strain-rate tensor and, so, the identity matrix component in the stress tensor can be written as

$$\left(\frac{\partial \tilde{u}_i}{\partial x_i}\right)\delta_{jk} = \tilde{S}_{ii}\delta_{jk} = \left(\sum_i \lambda_i\right)\delta_{jk} \ . \tag{C.5}$$

This would suggest that the $-\lambda^2\delta_{ij}$ term in Eq. C.3 acts similarly to the divergence of velocity (the trace of $\tilde{\vec{\vec{S}}}$). If instead of projecting $\tilde{\vec{\vec{S}}}$ onto $\vec{e}^{\lambda_3}$, it is projected onto itself, a model is obtained which is somewhat akin to other models based on the square of the gradients of velocity [111, 112]

$$(\widetilde{u_i u_j} - \tilde{u}_i\tilde{u}_j) = -\frac{K}{c}\left(\tilde{S}_{ik}\tilde{S}_{kj} - c\delta_{ij}\right) \ , \tag{C.6}$$

where c is a scaling coefficient that is expected to be related to the eigenvalues of $\tilde{\vec{\vec{S}}}\tilde{\vec{\vec{S}}}$ and is expected to normalize $\tilde{\vec{\vec{S}}}\tilde{\vec{\vec{S}}}$. The eigenvectors in $\vec{e}\vec{e}^{\top}$ are unit vectors and so it would be expected that $\tilde{\vec{\vec{S}}}\tilde{\vec{\vec{S}}}$ should function in a similar role of only providing the outer product of the normalized orientation vectors of the SGS vortices. Choosing c to be the trace of $\tilde{\vec{\vec{S}}}\tilde{\vec{\vec{S}}}$ the final form of the model becomes

$$(\widetilde{u_i u_j} - \tilde{u}_i\tilde{u}_j) = -K\left(\frac{\tilde{S}_{ik}\tilde{S}_{kj}}{\tilde{S}_{lm}\tilde{S}_{ml}} - \delta_{ij}\right) = -K\left(\frac{\tilde{S}_{ik}\tilde{S}_{kj}}{\tilde{S}_{lm}\tilde{S}_{lm}} - \delta_{ij}\right) \ . \tag{C.7}$$

Appendix D

Smooth-Ramp Geometry

The smooth-ramp geometry consists of three separate blocks with analytically defined coordinate transformation mappings. The Cartesian physical-space coordinate system is defined as x, y, and z in the streamwise, wall-normal, and spanwise directions respectively. The computational-space coordinate system is defined as ξ, η, and ζ, where ζ corresponds with the spanwise direction and ξ and η roughly correspond to the streamwise and wall-normal directions.

D.1 Computational Space to Physical Space

The streamwise and spanwise mappings are straightforward to construct as they are simply linear scalings. Constraining a linear equation to minimum and maximum values, the streamwise and spanwise mappings are obtained as

$$x = \xi \left(\frac{x_{\text{max}} - x_{\text{min}}}{\xi_{\text{max}} - \xi_{\text{min}}} \right) + \left(\frac{x_{\text{min}}\xi_{\text{max}} - x_{\text{max}}\xi_{\text{min}}}{\xi_{\text{max}} - \xi_{\text{min}}} \right) , \tag{D.1}$$

and

$$z = \zeta \left(\frac{z_{\text{max}} - z_{\text{min}}}{\zeta_{\text{max}} - \zeta_{\text{min}}} \right) + \left(\frac{z_{\text{min}}\zeta_{\text{max}} - z_{\text{max}}\zeta_{\text{min}}}{\zeta_{\text{max}} - \zeta_{\text{min}}} \right) . \tag{D.2}$$

From the AIAA 2022 WMLES workshop [91], the ramp is defined by the following fifth-order polynomial for $0 \leq x \leq 1$,

$$y = f(\xi) = H \left[1 - 10 \left(\frac{x}{L} \right)^3 + 15 \left(\frac{x}{L} \right)^4 - 6 \left(\frac{x}{L} \right)^5 \right] , \tag{D.3}$$

where the ramp length, L, is chosen to be unit length for all of the following derivations and the ramp height, H, is set to 0.22.

In order to fill in the geometry, the y value must additionally be a function of the computational-space coordinate η. More specifically, simple addition of a function of η provides an appropriate

starting point for further development

$$y = h\left(\xi, \eta\right) = f\left(\xi\right) + g\left(\eta\right) \ . \tag{D.4}$$

A quadratic polynomial provides a relatively simple choice of $g\left(\eta\right)$ that allows for some slight grid-stretching near either wall boundary dependent on the polynomial coefficients

$$g\left(\eta\right) = A\eta^2 + B\eta + C \ . \tag{D.5}$$

The quadratic coefficient, A, is left as a user-defined variable in order to provide the ability to tune the grid-stretching (set to be 0.000065 for this dissertation). Since $g\left(\eta\right)$ provides the second-dimension, the coefficients B and C are determined by constraining the polynomial to minimum and maximum values. These constraints are written as

$$g\left(\eta_{\text{min}}\right) = A\eta_{\text{min}}^2 + B\eta_{\text{min}} + C = y_{\text{min}} \ , \tag{D.6}$$

and

$$g\left(\eta_{\text{max}}\right) = A\eta_{\text{max}}^2 + B\eta_{\text{max}} + C = y_{\text{max}} \ . \tag{D.7}$$

From these constraints, the coefficients B and C are found to be

$$B = A\left(\frac{\eta_{\text{min}}^2 - \eta_{\text{max}}^2}{\eta_{\text{max}} - \eta_{\text{min}}}\right) + \left(\frac{y_{\text{max}} - y_{\text{min}}}{\eta_{\text{max}} - \eta_{\text{min}}}\right) \ , \tag{D.8}$$

and

$$C = A\eta_{\text{max}}\eta_{\text{min}} + \left(\frac{y_{\text{min}}\eta_{\text{max}} - y_{\text{max}}\eta_{\text{min}}}{\eta_{\text{max}} - \eta_{\text{min}}}\right) \ . \tag{D.9}$$

Since the upper wall boundary is flat, H must have a spatially-varying multiplier that is constrained to zero at the upper wall and one at the lower wall. Using another quadratic polynomial, a

multiplier function $s(\eta)$ is formulated as

$$s(\eta) = S = a\eta^2 + b\eta + c = S \,, \tag{D.10}$$

where S is the ramp-height multiplier and "a" is a user-defined stretching parameter (set to be -0.00025 for this dissertation). Setting the constraints as $S_{\text{max}} = 0$ (where "max" denotes the value at the maximum η location, not the maximum value of S) and $S_{\text{min}} = 1$, the coefficients b and c are given as

$$b = a\left(\frac{\eta_{\text{min}}^2 - \eta_{\text{max}}^2}{\eta_{\text{max}} - \eta_{\text{min}}}\right) + \left(\frac{S_{\text{max}} - S_{\text{min}}}{\eta_{\text{max}} - \eta_{\text{min}}}\right) = \left(\frac{a\eta_{\text{min}}^2 - a\eta_{\text{max}}^2 - 1}{\eta_{\text{max}} - \eta_{\text{min}}}\right) \,, \tag{D.11}$$

and

$$c = a\eta_{\text{max}}\eta_{\text{min}} + \left(\frac{\eta_{\text{max}}}{\eta_{\text{max}} - \eta_{\text{min}}}\right) \,. \tag{D.12}$$

The resulting form of $h(\xi, \eta)$ is given as

$$y = h(\xi, \eta) = HD\left[a\eta^2 + b\eta + c\right] + \left[A\eta^2 + B\eta + C\right] \,, \tag{D.13}$$

where $D = \left[1 - 10\left(\frac{x}{L}\right)^3 + 15\left(\frac{x}{L}\right)^4 - 6\left(\frac{x}{L}\right)^5\right]$. A slightly more compact form is written as

$$y = h(\xi, \eta) = E\eta^2 + F\eta + G \,, \tag{D.14}$$

where $E = HDa + A$, $F = HDb + B$, and $G = HDc + C$.

For the region of the domain before the ramp (i.e. $x < 0$), all of the previous mappings are valid with the only change being that $D = 1$. Similarly, for the region of the domain after the ramp ($x > 1$), $D = 0$ and all of the mapping terms are computed as presented above.

D.2 Physical Space to Computational Space

Reversing the transformations provides

$$\xi = \left(\frac{\xi_{\text{max}} - \xi_{\text{min}}}{x_{\text{max}} - x_{\text{min}}}\right)\left[x - \left(\frac{x_{\text{min}}\xi_{\text{max}} - x_{\text{max}}\xi_{\text{min}}}{\xi_{\text{max}} - \xi_{\text{min}}}\right)\right] , \tag{D.15}$$

and

$$\zeta = \left(\frac{\zeta_{\text{max}} - \zeta_{\text{min}}}{z_{\text{max}} - z_{\text{min}}}\right)\left[z - \left(\frac{z_{\text{min}}\zeta_{\text{max}} - z_{\text{max}}\zeta_{\text{min}}}{\zeta_{\text{max}} - \zeta_{\text{min}}}\right)\right] . \tag{D.16}$$

The η component has two cases. If both A and a are zero, the η-to-y transform is linear and the inverse transform is simply

$$\eta = \frac{y - G}{F} . \tag{D.17}$$

However, if either A or a are non-zero, the η-to-y transform is quadratic and the inverse transform is

$$\eta = \frac{-F \pm \sqrt{F^2 - 4EI}}{2E} \quad , \quad I = G - y , \tag{D.18}$$

where the positive value is chosen and the result is

$$\eta = \frac{-F + \sqrt{F^2 - 4EI}}{2E} . \tag{D.19}$$

D.3 Derivatives of Mappings

The derivatives of the physical-space coordinates with respect to the computational-space coordinates are zero except for $\frac{\partial x}{\partial \xi}$, $\frac{\partial y}{\partial \xi}$, $\frac{\partial y}{\partial \eta}$, and $\frac{\partial z}{\partial \zeta}$. Both $\frac{\partial x}{\partial \xi}$ and $\frac{\partial z}{\partial \zeta}$ are simply

$$\frac{\partial x}{\partial \xi} = \left(\frac{x_{\text{max}} - x_{\text{min}}}{\xi_{\text{max}} - \xi_{\text{min}}}\right) \quad , \quad \frac{\partial z}{\partial \zeta} = \left(\frac{z_{\text{max}} - z_{\text{min}}}{\zeta_{\text{max}} - \zeta_{\text{min}}}\right) . \tag{D.20}$$

Differentiating Eq. (D.13) with respect to ξ provides

$$\frac{\partial y}{\partial \xi} = H\left[a\eta^2 + b\eta + c\right]\left[-30\left(\frac{x}{L}\right)^2 + 60\left(\frac{x}{L}\right)^3 - 30\left(\frac{x}{L}\right)^4\right]\frac{\partial x}{\partial \xi} , \tag{D.21}$$

while differentiating Eq. (D.14) with respect to η provides

$$\frac{\partial y}{\partial \eta} = 2E\eta + F \ . \tag{D.22}$$